Kinematics and Optimal Control of a Mobile Parallel Robot for Inspection of Pipe-like Environments

by

Hassan Sarfraz

Thesis submitted to the
Faculty of Graduate and Postdoctoral Studies
In partial fulfillment of the requirements
For the M.A.Sc. degree in
Electrical and Computer Engineering

School of Information Technology and Engineering
Faculty of Engineering
University of Ottawa

Abstract

The objective of this thesis is to analyze the kinematics of a mobile parallel robot with contribution that pertain to the singularity analysis, the optimization of geometric parameters and the optimal control to avoid singularities when navigating across singular geometric configurations. The analysis of the workspace and singularities is performed in a prescribed reference workspace regions using discretization method. Serial and parallel singularities are analytically analyzed and all possible singular configurations are presented. Kinematic conditioning index is used to determine the robot's proximity to a singular configuration. A method for the determination of a continuous and singularity-free workspace is detailed.

The geometric parameters of the system are optimized in various types of pipe-like structures with respect to a suitable singularity index, in order to avoid singularities during the navigation across elbows. The optimization problem is formulated with an objective to maximize the reachable workspace and minimize the singularities. The objective function is also subjected to constraints such as collision avoidance, singularity avoidance, workspace continuity and contact constraints imposed between the boundaries and the wheels of the robot. A parametric variation method is used as a technique to optimize the design parameters. The optimal design parameters found are normalized with respect to the width of the pipe-like structures and therefore the results are generalized to be used in the development phase of the robot.

An optimal control to generate singularity-free trajectories when the robotic device has to cross a geometric singularity in a sharp 90° elbow is proposed. Such geometric singularity inherently leads to singularities in the Jacobian of the system, and therefore a modified device with augmented number of degrees of freedom is introduced to be able to generate nonsingular trajectories.

Acknowledgements

First and above all, I praise God, the almighty for providing me this opportunity and granting me the capability to proceed successfully. This thesis appears in its current form due to the assistance and guidance of several people. I would therefore like to offer my sincere thanks to all of them.

My sincere appreciation and thanks goes to my supervisor, Prof. Wail Gueaieb and my co-supervisor, Prof. Davide Spinello for their guidance and constructive comments which helped me push the limits of my knowledge and abilities. I would also like to thank my supervisors for their financial contribution toward my masters of science program. During my program, I was fortunate enough to work with Dr. Lounis Douadi, a post-doctoral fellow at University of Ottawa. My thanks to him for invaluable advice and supervision during the initial stage of my thesis.

Last but not the least, I would like to thank my family. My parents for their encouragement and generous financial support, without which I could not have pursued my academic interest. My brother, sisters, cousins and Sabrina for being a source of inspiration in my life.

Contents

List of Tables

List of Figures

List of Abbreviations

DOF	Degrees of Freedom
SPI	Small Pipeline Inspector
DIRECT	DIviding RECTangles algorithm
KCI	Kinematic Conditioning Index
GCI	Global Conditioning Index
SQP	Sequential Quadratic Programming
SPEA-2	Strenth Pareto Evolutinary Algorithm - Genetic Algorithm
PKM	Parallel Kinematic Manipulator
ANSI B16.9	American National Standard Institute - Standards of Pipes and Fittings
w.r.t	with respect to

List of Symbols

W_p	Width of the pipe
φ	Radius of Curvature
r	Radius
$H_{1,2}$	position of the arm joint on the body of the robot
$\Pi \in \Re$	region of manoeuvre for the robot
P_1	Contact point of the left wheel with the pipe wall
P_2	Contact point of the right wheel with the pipe wall
s_1	left pipe wall defined as arc length parameter
s_2	right pipe wall defined as arc length parameter
α_1	orientation angle of the left arm w.r.t the body of the robot
α_2	orientation angle of the right arm w.r.t the body of the robot
G	Position of the center of gravity of the robot
$(x_G,\ y_G)$	global coordinates defining the position of center of gravity G of the robot
$\mathbf{x}$	End-effector pose
$\dot{\mathbf{x}}$	End-effector velocity vector
$\mathbf{q}$	generalized joint coordinates
$\dot{\mathbf{q}}$	Joint velocity vector
$\mathbf{r}$	position vector
Γ_{ref}	Reference or Prescribed Workspace region
Γ_{sf}	Singularity-free Workspace region
l	length of the arm of mobile parallel robot
w	width of the body of mobile parallel robot
h	height of the body of mobile parallel robot
a	Position of the arm joint of the mobile parallel robot
θ_σ	Orientation of the robot w.r.t center-line of the pipe
θ	Orientation of the robot w.r.t Global coordinate

$\dot{\theta}$	Angular velocity of the body of the robot
χ	design parameters (vector)
d_l	range of l design parameters
d_w	range of w design parameters
d_h	range of h design parameters
d_a	range of a design parameters
$\mathbf{F}(\chi)$	Objective Function as a function of design parameters
$\Gamma_{sf}(\chi)$	Singularity-Free Workspace w.r.t χ
$\chi_{[q]}$	design parameters χ after q^{th} iteration
ϵ	tolerance between the two design parameters χ

Chapter 1

Introduction

Water and energy are an essential part of every individual's life. Population and economic growth is driving the demand of water and energy. Many industries including agricultural, transportation, manufacturing and construction highly depend on access to a reliable water supply and energy such as natural gas, diesel, petroleum and other products made from crude oil. These resources are delivered safely and efficiently mainly through large networks of transmission pipelines. It is estimated that a total length of $3,500,000\ km$ of high pressure transmission pipeline transporting various types of energy resources exists around the world, and approximately $32,000\ km$ of transmission pipelines are constructed every year [32]. These pipelines are susceptible to corrosion, cracking, damage due to digging or natural disasters. Many pipeline operators are currently facing these issues in aging network of pipelines [14, 39, 75]. A possible disruption due to maintenance or repair may lead to shortage in supplies as well as major economic losses. Automating their inspection process is not only safer for humans but also economically relevant. Therefore, it is becoming a pressing and urgent necessity to use autonomous robotic tools to inspect and maintain hazardous confined environment such as transmission pipelines.

A flexible multi-body mechanism, or more specifically wheeled snake-like robots, exhibit excellent mobility in these confined environments as compared to other wheeled mobile robots such as autonomous cars. This is due to the fact that snake-like robots mimic the mobile properties of a snake, which can easily move through tortuous environments such as narrow passages and rough terrains with high speed and good steering ability. Some of the applications of snake-like robots, other than non-destructive pipeline inspection, include search and rescue operations [56], active hose for fire-fighting [76],

maintenance of hazardous areas in industrial plants [15] and domestic applications [31]. The schematic of a snake-like robot is presented in figure 1.1. The modules are connected using passive revolute joints, and kinematically characterized by three degrees of freedom. Each module is a parallel mechanism on a mobile platform. Kinematically, a parallel robot can be defined as a mechanism whose end effector is supported by more than one kinematic chain attached to the basis. It is propelled by the motion of wheels that are in contact with the walls of a pipe-like environment in which it is deployed. Furthermore, multiple modules are required to manage the mechanical and electronic components of the snake-like robot. These components include actuators, motors, sensors and power source.

The autonomous operation of the robotic device is based on decision making algorithms, that in the simplest case consist of controllers for navigation. Control algorithms are generally strongly affected by kinematic singularities in the robot and by eventual geometric singularities in the environment. A singular configuration is such that one or more joint degrees of freedom are no longer independent. Therefore the characterization, within suitable metrics, of the motion singularities is a necessary step to identify critical scenarios with respect to the autonomous navigation. A control strategy for the path-planning of the robot can be obtained by maximizing a metric that quantifies the distance from these singularities.

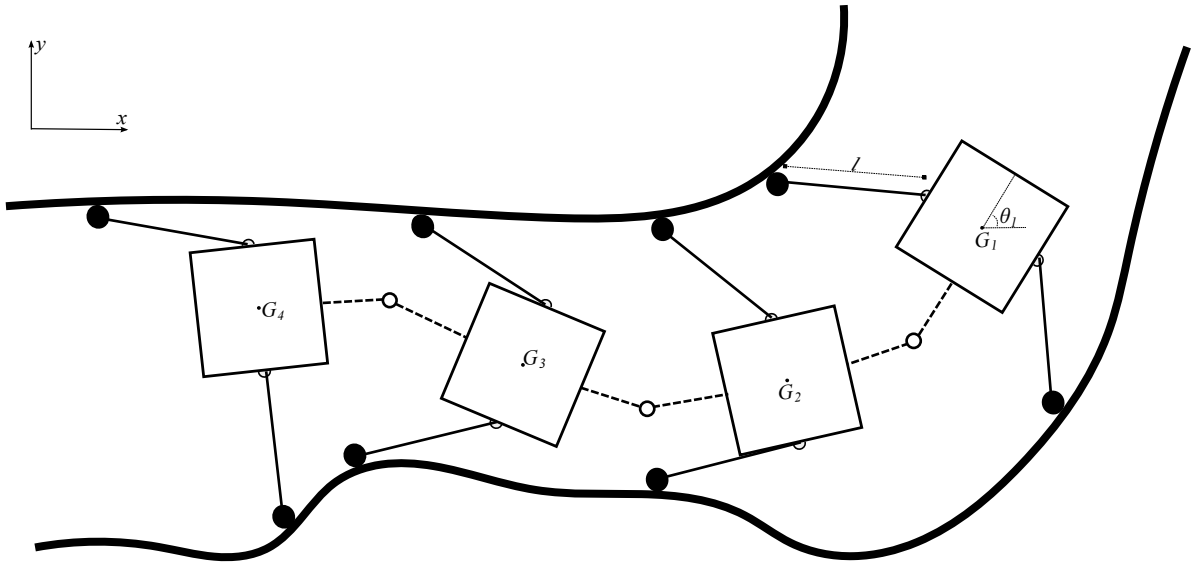

Figure 1.1: Snake-like robot for confined environment exploration

1.1 Thesis Objective and Contribution

The main objective of this thesis is the kinematic analysis of a mobile robot for non-destructive inspection of confined environments. The emphasis is on a single module that is a parallel robot on a mobile platform. Geometric parameters of the system are optimized with respect to a suitable singularity index, in order to avoid singularities during the navigation across elbows. An optimal control to generate singularity free trajectories when the robotic device has to cross a geometric singularity (sharp elbow) is proposed. Such geometric singularity inherently leads to singularities in the Jacobian of the system, and therefore a modified device with augmented number of degrees of freedom is introduced to be able to determine nonsingular trajectories. A detailed list of contributions follows.

Study of Singularities: The determination of singular configurations using determinant based method is performed. The proximity to singularities in various confined environments is determined. The results play a key role in path-following control of the robot in confined environments. For example, during a turn in an elbow of a pipe-like structure, the robot may follow a certain path to avoid singular configurations.

Determination of Optimal Geometry: The design parameters of the robot are optimized based on multiple performance criteria such as singularity avoidance, collision avoidance and continuity in the path. Parametric Variation Method is used to optimize the design parameters.

Optimal Control: A critical scenario consisting of a sharp 90^o elbow, introduces a discontinuity in the workspace. To address this scenario, a motion control is formulated as an optimization problem, with optimization function encoding singularity quantification and collision avoidance.

An in-depth geometric and kinematic analysis of the robot is performed in various scenarios. The results from this thesis are part of the design and development of a snake-like robot for inspection and maintenance in confined environments.

1.2 Organization of this Thesis

The thesis is organized as follows.

Chapter 2: An overview of relevant literature is presented, on the development of mobile robots in confined environments, and on methods for workspace and singularity determination. Briefings on design optimization techniques are also presented.

Chapter 3: The kinematics of the mechanism studied here is presented. The position and velocity kinematic equations are also detailed. Five different types of pipe-like structures are introduced as examples of confined environments, where the robot's manoeuvrability and performance will be analyzed.

Chapter 4: The determination of dexterous workspace and singularities of the robot is presented and analyzed based on a discretization method. The dexterous workspace is all of the possible points the robot can reach with an arbitrary orientation. The singularities are determined by defining the proximity to a singular configuration, by using the Kinematic Conditioning Index of the robot.

Chapter 5: An analysis of design parameters is performed. The optimization problem is formulated by defining design variables, constraints and cost function. The technique used to optimize the cost function is detailed to satisfy multiple performance criteria in pipe-like structures. Simulation results of optimal geometry and design parameters are presented and discussed.

Chapter 6: A critical scenario of the robot crossing a sharp 90^o elbow is presented. A path-following control together with optimal control that maximizes a measure of singularity is proposed as a solution to tackle this scenario.

Chapter 7: Summary and Conclusions are presented.

1.3 Publications

The following publications are produced during the work on this thesis.

Journal Paper

Lounis Douadi, Davide Spinello, Wail Gueaieb and Hassan Sarfraz. "Planar kinematics analysis of a snake-like robot". Robotica.
doi:10.1017/S026357471300091X.

Conference Paper

Davide Spinello, Hassan Sarfraz, Wail Gueaieb, Lounis Douadi, "Critical Maneuvers of an Autonomous Parallel Robot in a Confined Environment", Proceedings of the International Conference on Mechanical Engineering and Mechatronics (ICMEM), 8 pp. Paper no. 196, 2013.

Chapter 2

Literature Review

2.1 Introduction

This chapter provides an overview of the literature on the development of snake-like robots for autonomous operations in confined environments. Various applications and features pertaining to snake-like robots are discussed. The review also covers the methods of determining workspace and singularities of robotic mechanism. Some of the performance indices which effects the workspace and singularities of the robot are discussed. These indices are used to optimize the design parameters. Moreover, techniques used to optimize the design parameters are also detailed.

The literature review is organized as follows. Section 2.2 provides details on the development of snake-like mobile robots for confined environments. In Section 2.3 and 2.4 various methods for determining the workspace and singularities of a robot are discussed, respectively. Two types of design optimization criteria are presented in section 2.5 based on workspace and on performance indices. Section 2.6 provides an overview of various optimization techniques used for optimal design of the robot.

2.2 Development of Snake-like Robots for Confined Environments

Many research efforts have been devoted to the development of fully autonomous mobile robots to be deployed in a confined environment, such as sewer networks, gas pipelines or disaster zones for rescue purposes. These types of environment consist of complex

terrain, often too dangerous for humans to operate. The design of a snake-like robot can be very advantageous in such environments.

In Shin *et al.* [62], a snake-like robot called KAEROT was developed using eleven 2 degrees-of-freedom (DOF) actuator modules. KAEROT has the ability to move in pipe-like structures with a sequence of holding motion known as concertina. During the holding motion, the snake robot keeps one of its end stationary by folding the modules pressing outward in a pipe-like structure. This locomotion is common in snakes that stretch and fold their bodies to move forward. The forward motion of the robot is achieved by keeping the folded part stationary while the rest of the body is either pulled or pushed. Concertina locomotion is useful through narrow passages such as pipes. However, this method of locomotion have limitations since it requires the diameter of the pipe-like structure to be less than the length of one module of the robot in order to perform efficiently.

In Jamoussi [38], a multibody autonomous robot known as Small Pipe Inspector is developed for the inspection of long pipelines with small diameters. A solution is proposed for the inspection of pipe-like structures ranging from 10,000 to 30,000 feet in length using a spiral drive as a form of locomotion. The design and locomotion of SPI have the flexibility to navigate inside the pipelines with varying width.

In Wakimoto *et al.* [79], a micro snake-like robot is developed and tested for small pipe inspection. This robot has the capability to move inside pipes with various diameters using lateral undulation type of locomotion. Lateral undulation is a serpentine crawling which is the fastest and most common form of manoeuvrability in snakes. During this motion, the robot's joints are driven by continuous sine wave signals which are propagated from its head to tail end. The forward motion of the robot is achieved consistently with the sine wave motion, using the friction between the robot and the inner wall of the pipe. The friction forces play an important role for this robot to propel forward especially if it needs to move upward in a vertical pipe against the gravity.

In Sigurd *et al.* [18], a snake-like robot called PIKo is proposed to inspect complex pipe structures. PIKo is a multi module robot which propels itself by the assistance of active wheels attached on each module. The benefit of this design is that it is able to perform horizontal and vertical locomotion. The vertical climb is achieved by using an opposing-push scheme based on friction between pipe and wheels to move upward. The serially connected modules of PIKo robot expand within the pipe in order to be in contact with the inner walls. This enables the robot to adapt and move in pipes with various diameters.

In Ono *et al.* [57], an earthworm-like mobile robot is designed for inspection while navigating inside a pipe. The development of this robot was inspired by an incident in atomic power plant, where the cooling water pipe had leakage due to a crack from vibrations. It was necessary to inspect the cracked region while avoiding radiation from flowed water. Moreover, a heat insulation material had to be removed from the cracked pipe. Therefore, an artificial earthworm type inspection robot was constructed. This robot uses three rubber bellows and pneumatic actuators to manoeuvre. The locomotion is highly dependent on the friction between the rubber rings and the inner pipe walls which restricts its adaptability to pipes with varying diameters.

In Yoon *et al.* [82], an inpipe inspection robot is proposed which uses inchworm locomotion to climb vertically. The mechanism consists of three modules. The front and end modules use pneumatic actuators to press against the walls. The module in the middle is a prismatic actuator. The forward motion is achieved by keeping the end module at a fixed position and by extending the front module with the help of the prismatic actuator in the middle. Kwon and Yi [47] also presented a robot with inchworm locomotion for inspection in pipe-like environment. The robotic mechanism consists of two modules connected by a spring shaft. The modules consists of a differential drive for steering and a spring loaded four-bar mechanism to grip the inside walls.

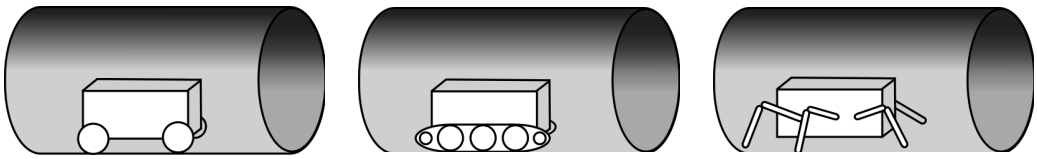

(a) (b) (c)

Figure 2.1: Schematics of other types of mobile robots for in-pipe inspection

Other type of robots used for the inspection of confined environment are wheeled, tracked and crawling robots. Schematic drawings for these types of robot are shown in figure 2.1. Wheeled mobile robots consist of a rigid body with a system of wheels to support its payload to provide motion with respect to the ground as shown in figure 2.1(a). For the purpose of confined environment inspection some of the robots based on wheeled platforms can be found in the literature; see for instance , the works by Hirose *et al.* [30], Kolesnik *et al.* [44] and Zhu [88]. Tracked mobile robot as shown in figure 2.1(b) are very effective on uneven terrains, soft and cracked ground. These types of robot exhibit excellent traction due to increased contact points between the

belt and the ground. Some of the disadvantages are higher energy consumption and mechanical complexity. Moghaddam *et al.* [55] and Masayuki *et al.* [51] proposed to use track driven robots for the inspection of confined environment. Crawling or legged mobile robots are mostly inspired by insects to replicate their efficient manoeuvrability and overcome obstacles which are difficult for a wheeled mobile robot. Examples of crawling robots for in-pipe inspection can be found in literature by Shapiro *et al.* [61] and Stefanini *et al.* [74]

2.3 Workspace Determination

Workspace is the region in space that can be reached by the end effector of a robotic mechanism. The availability of workspace is crucial in path-planning applications where a continuous workspace is required during a task execution. The workspace region can be restricted by many factors such as mechanical joints, limitation of actuators, proximity to a singular configuration or collisions. Different types of workspace can be obtained by imposing constraints on the design parameters such as "constant orientation workspace" or "dexterous workspace". A constant orientation workspace is the region that can be reached by the end-effector of the robot with a fixed orientation. Dexterous workspace is the region that can be reached by all possible orientation of the end-effector of robot. Here we present three methods for the determination of workspaces. These methods are known as geometrical method, discretization method and numerical method. To concisely describe certain manipulators by the sequence of joints composing them, we will adopt the following notation: P for prismatic joint; R for revolute joint; S for spherical joint; and U for universal joint. Actuated joints will be indicated by underlying the corresponding letter.

2.3.1 Geometrical Methods

This method is useful in generating the boundaries of the workspace of a robot. Considering a two-link planar arm as an example to demonstrate the geometric method as shown in figure 2.2. In this case, a boundary formed using the link-1 is found by keeping the one side of the arm fixed and rotating the other side about the fixed point, creating a geometrical shape denoted by B_1. Next, the boundaries formed using link-2 is found by rotating it about the revolute joint connecting it with link-1. Once all the shapes from each link of the arm are obtained, a workspace region is formed by combining all B_i's.

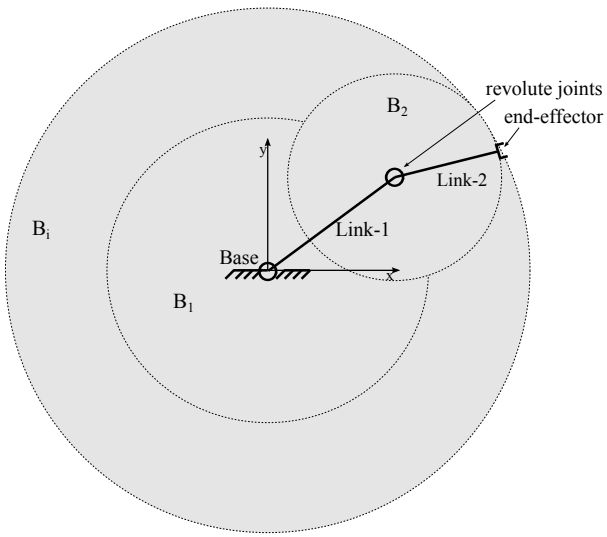

Figure 2.2: Two-link planar arm workspace region

The calculation of a workspace using geometric approach can be performed by using CAD tools. Bonev and Ryu [7] implemented this method using a CAD tool to represent the constant orientation workspace of a 6 degree-of-freedom (DOF) PRRS parallel manipulator. Gallant *et al.* [19] used a geometric method to determine the dexterous workspace of a redundant planar parallel robot. The architectures studied by Gallant *et al.* are the RRRR and RRPR manipulators, where the boundaries of the dexterous workspace is determined by finding the intersection of the dexterous workspace of each kinematic chain. One of the advantages of this method is that it can be implemented efficiently in providing the minimal representation of a workspace, which is beneficial to evaluate the boundaries and volume. However, as mentioned by Merlet [53] and Gallant [19], it is difficult to take into account all the kinematic constraints such as the limits of the orientation of links and the fact that the base may be mobile.

2.3.2 Discretization Methods

In the discretization approach, a reference grid in the form of Cartesian or Polar coordinates is used. The reference grid may cover the total length of the robot. The discretely defined reference workspace is tested at each grid point by using the kinematics of the robot to find if the solution exists. When the solution to the end-effector position exists the actual workspace is well defined. One of the advantages of this approach over the geometric approach is that one can take into account all the constraints of the robot while

calculating the workspace [53], and a disadvantage is that the accuracy of the boundaries of the workspace depends on the sampling step used to create the reference grid. Moreover, if the reference workspace is large, testing all points may be time consuming. Huang [35, 34] used the discretization method to find the optimal design parameters that maximize its workspace. Badescu and Mavroidis [54] used a discretization method to characterize the workspace of a reconfigurable hyper-redundant robotic arm. Similarly, Soheil *et al.* [86] used this method to find the workspace of a 4DOF planar parallel manipulator.

2.3.3 Numerical Methods

Adkins and Haugh [1] used a numerical approach to obtain the constant orientation workspace of a planar Stewart platform by finding a point on the boundary of the workspace and then using numerical continuation method to calculate the rest of the workspace boundaries. A method for acquiring the boundary of the workspace in terms of a constrained optimization problem is demonstrated by Snyman *et al.* [65]. This numerical method starts by finding a point inside the coordinate space of a manipulator. This point is used as an origin for multiple vectors pointing outward in all directions. The end point of each vector is calculated by solving for the inverse kinematics of the robot. Thereafter, the boundaries of the workspace are formed by combining all the end points of the vectors with a line. This method is most suitable for manipulators with a stationary base and workspace boundaries forming a convex shape as shown in figure 2.3. Moreover, this method poses limitations if the actual workspace of the robot is non-convex as shown in figure 2.4. To overcome this limitation, more than one radiating point must be used. However, this increases the complexity as well as the computational effort of the algorithm.

Another type of numerical approach to determine the workspace of a robotic manipulator uses the Interval Analysis [9, 10, 53]. Chablat *et al.* [9] conducted a workspace analysis of the orthoglide which is a 3DOF parallel mechanism featuring three fixed linear joints mounted orthogonally and a mobile platform connected to the linear joints by three articulated parallelograms. A dexterous workspace is found using the Interval Analysis on the bases of prescribed bounded velocity and force transmission factor defined by the eigenvalues of the Jacobian matrix. The method starts by initializing the algorithm with a prescribed workspace region as a set of three-dimensional Cartesian box whose width is greater than a given threshold. The value of this threshold defines the quality of the

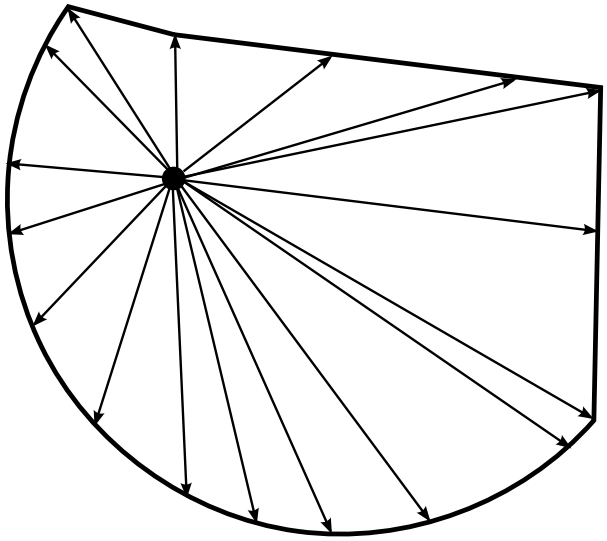

Figure 2.3: Convex shape of a workspace boundary

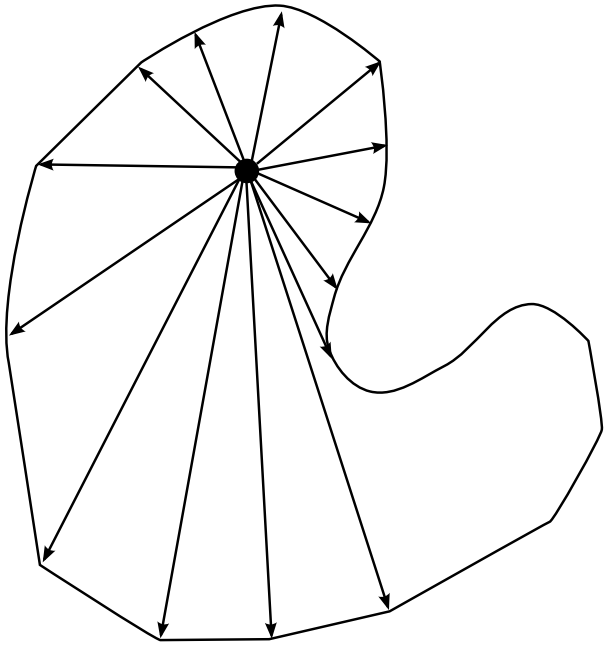

Figure 2.4: Non-Convex shape of a workspace boundary

workspace boundaries. The algorithm then takes this box as an input and analyzes it for one of three possible outcomes. This includes that for an arbitrary point in the box the eigenvalues lies in the specified range or that for any point in the box one of the eigenvalue is either lower or greater than the prescribed range or that both above men-

tioned conditions does not hold for all points in the box. Based on the above conditions respectively, the box is stored as part of the dexterous workspace or discarded or in the third case a bisection method is used to divide the box in to two new sub-boxes making sure that the width are greater than the defined threshold. The algorithm re-evaluates the new sub-boxes until the width of the sub-box reaches the threshold. The advantage of this method is that it can easily handle high degrees-of-freedom with more constraints, however it is very computer-intensive.

Stamper [72] used the Monte Carlo method to determine the workspace volume of a 3DOF manipulator as a function of its links lengths and orientation. This method starts off by initializing the volume of the workspace based on the total link lengths of the manipulator. Then a large number of points are randomly selected within the volume and tested for the existence of the inverse kinematic solution. The points which fall within the selected volume are used to estimate the workspace. The accuracy of this method depends on a careful selection of an initial volume and on the number of points used to determine the existence of a manipulator's workspace. A similar numerical method has been used by Rastergar *et al.* [59] and Alciatore *et al.* [2] to determine the workpace.

2.4 Singularities Determination

In the design of a robotic mechanism and the study of its kinematics, a designer should take into consideration the occurrence of singularities within the workspace region. Singular configurations can be determined through the study of the Jacobian, which defines the linear mapping between joint velocities and the end-effector velocities. When the Jacobian becomes rank deficient, singularities occur at that configuration. Therefore, when a singularity exists the mobility of a mechanism is reduced as a subset of degrees of freedom of the end effector becomes unavailable. Moreover, an unbounded solution to the inverse kinematic may exist. Also, in the neighbourhood of a singular configuration, a small velocity in the operational space may lead to large velocities in the joint space. One of the ways singularities can be avoided during the motion planning of the robotic mechanism is to study the workspace to find each singular pose, and introduce repulsive artificial potentials in correspondence of the singular points.

A parallel manipulator is a closed-loop kinematic chain, whose end-effector is linked to the base by several independent kinematic chains. Parallel manipulators are able to withstand higher load since the total load can be shared among the parallel links of the

manipulator. An example of a Stewart parallel manipulator is shown in figure 2.5. This mechanism consists of a fixed base and a moving platform which are connected by six linear actuators also known as prismatic joints. The mechanism is able to change the position and orientation of the moving platform by varying the lengths of the prismatic joints. Merlet [53] showed three types of kinematic singularities which may exist in a

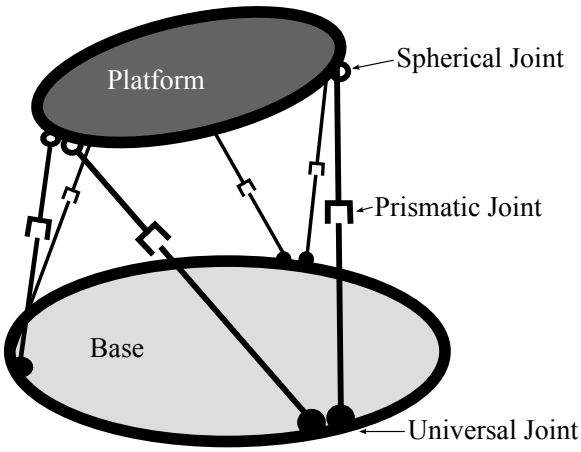

Figure 2.5: Gough-Stewart parallel manipulator

parallel manipulator. The first type is known as serial singularity which occurs when a non-zero velocity in actuated joints leads to zero end-effector velocity. This type of singularity exists in both open and closed kinematic chains. The second type is known as a parallel singularity. This type of singularity only exists in manipulators with closed kinematic chains such as parallel manipulators. A parallel singularity occurs when a motion of the end-effector exists even when the joints are in a motionless state. In this configuration, an infinitesimal motion in robot's end-effector may occur even if the actuators are all locked, leading to uncontrolled degrees of freedom on the end-effector. The third type is a combination of the serial and parallel singularities, where the end-effector may experience motion while the actuated joints are locked and vice versa.

2.4.1 Analytical Methods

When the Jacobian matrix of a manipulator is square, the singular configuration of the robot can be determined by finding the determinant roots of their inverse Jacobian. Gossilin *et al.* [21] uses analytical expressions of the determinant of the inverse Jacobian to analyse different types of singularities found in various closed-loop kinematic chains. A thorough analysis is performed on 1DOF planar RRRP mechanism, 2DOF Watt's linkage,

3DOF parallel manipulator with revolute joints, spherical 3DOF parallel manipulator and spatial 6DOF parallel manipulator. Daniali *et al.* [12] analysed singularities of 24 different types of 3DOF planar parallel manipulators using the determinant of Jacobian matrices. The manipulators in study were classified in two classes and for each three types of singularities were identified. Sefrioui *et al.* [60] studied singularities of a general 3DOF planar parallel manipulator using the analytical method based on the determinant. Moreover, a graphical representation of the singularity locus is illustrated with the help of a CAD tool. The singularity loci of 3DOF spherical parallel manipulator have been analytically expressed in the joint and cartesian space by using the direct and inverse kinematic solutions [22].

Another method to determine singularities is based on an index that measures the proximity to a singular configuration. By calculating the condition number κ at a given configuration for the manipulator, one can determine its proximity to a singular configuration. This index is described in section 2.5.2. Huang Z. Ming [35], Kun-ku Oh *et al.* [45], Guowu *et al.* [25] have used kinematic conditioning index (KCI), which is the reciprocal of the condition number of the Jacobian matrix, to characterize the degree of singularity. The KCI is bounded between 0 and 1, where a value of 0 depicts a singular configuration and a value of 1 depicts the farthest configuration from singularity. Fattah *et al.* [16] studied the condition number of the Jacobian matrix of a 3DOF parallel manipulator and Stewart-Gough platform. Using KCI they identified how far the manipulator is from being singularity-free as the configuration changes. Zanganeh *et al.* [85] used KCI as a general framework to determine the optimal kinematic design of parallel manipulators.

It is noted in Gosselin *et al.* [21] that the analytical method of finding the determinant of the inverse Jacobian matrix is in general mostly suitable for manipulators with 3DOF or less. Otherwise, the analytical expression becomes too complicated to analyse. In this case, Grassmann geometry is highly desirable to use, as discussed in the following section.

2.4.2 Geometric Methods

The singular configurations of a manipulator can be determined using a method known as Grassmann-line geometry. This method is based on determining the linear dependencies of lines which in case of a parallel mechanism represents the linkage joining the base and a moving platform. Plucker vectors are used to define these lines in a three dimensional

space. Consider a line in three-dimensional space passing through two points, p and q. Figure 2.6 illustrates this line and an origin point o. The Plucker vector of this line can be defined by first calculating the vectors $\mathbf{U} = p-q$ and $\mathbf{V} = (p-o)\times(q-o)$, which is normal to the plane spanned by $p-o$ and $q-o$. Hence $\{\mathbf{U};\mathbf{V}\}$ is the plucker vector of a line. The semicolon ';' distinguishes it from a Cartesian vector. The plucker coordinates of a line are therefore represented by a pair of three-dimensional vectors. One is parallel to the line and the other is the moment of that vector about the origin. Merlet [53] showed that

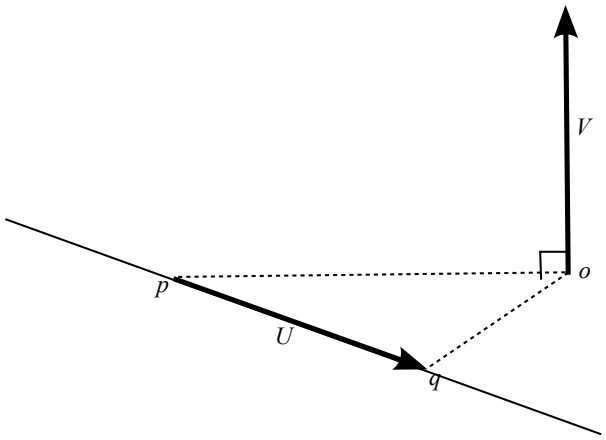

Figure 2.6: Defining a Plucker vector

the Jacobian of a fully parallel Stewart-Gough consists of plucker vectors of the lines associated with the prismatic actuators of the manipulator. The singularity analysis of the Stewart-Gough mechanism was based on finding geometrical conditions for linear dependencies between these lines. Figure 2.7 illustrates the geometrical conditions of one, two and three lines, respectively. As shown in figure 2.7 a line in a three-dimensional space itself represents a geometric characteristic. When two lines exists in three-dimensional space they can either be a pair of skew lines or intersect each other forming a plane. When 3 lines exist in a three-dimensional space they can be characterized in four different ways. Three lines may form a plane as shown in figure 2.7(d), or all lines may pass through a point as shown in figure 2.7(c), or form two intersecting planes as shown in figure 2.7(b) or three skew lines with a common point where a line may connect know as a regulus as shown in figure 2.7(a). A basic example of a planar parallel manipulator presented by Merlet [53] is considered to determine its singular configuration using Grassmann-line geometry as shown in figure 2.8. The two rigid bodies in this case, a moving platform and a stationary base are attached using three linkages. By reference to figure 2.7 it can be seen that the only possibility for a three line system to have a geometric characteristics

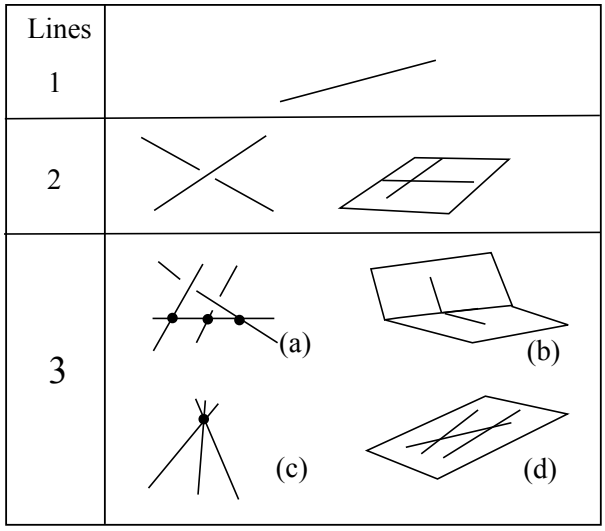

Figure 2.7: Geometrical conditions of one, two and three lines

of a two line system is when the lines representing each linkage cross at the same point c, as illustrated in figure 2.8. This scenario results in rank deficiency of a Jacobian and a singular configuration. To avoid this singular configuration the three linkage structure must be reconfigured as shown in figure 2.9. It can be seen that in this case the lines representing the three linkages can never cross at the same point and therefore can never be represented as a system with two linkage.

Fichter [17] used line geometry to perform singularity analysis on Gough-Stewart platform. Similarly, Simaan *et al.* [64] obtained singular configurations of 14 composite 6DOF robots using line geometry. It was also shown that the rows of the inverse Jacobian matrix represented Plucker vectors of the lines controlling the manipulator's motion. Wolf *et al.* [80] also used line geometry to analyze the singularities of 3DOF CaPaMan parallel manipulator by using the linear dependency of lines derived from external wrenches acting on the moving platform to forces at the joints. Singularity analysis of a parallel robot based on Stewart platform have been performed by Hao and McCarthy [27] using Grassmann-line Geometry. Classification of singularities based on line geometry have also been done on a fully parallel 5DOF manipulator by Mbarek *et al.* [52].

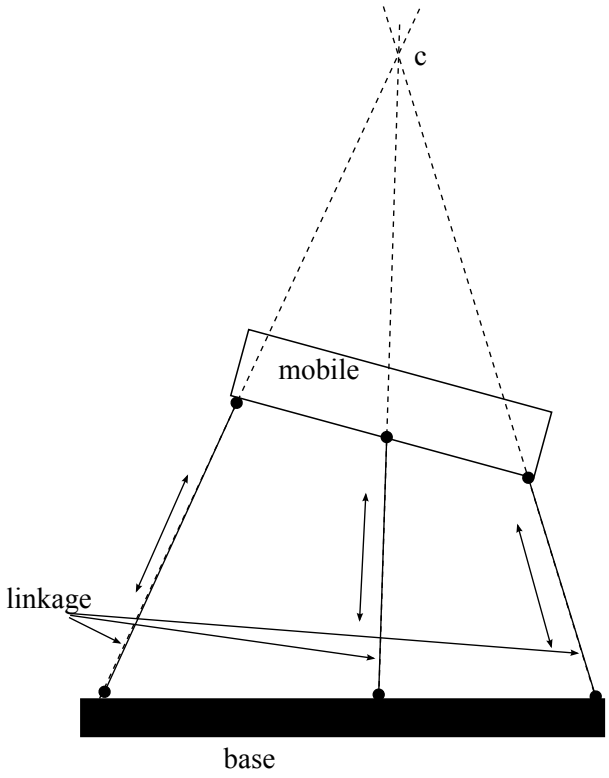

Figure 2.8: Singular configuration of a planar parallel manipulator

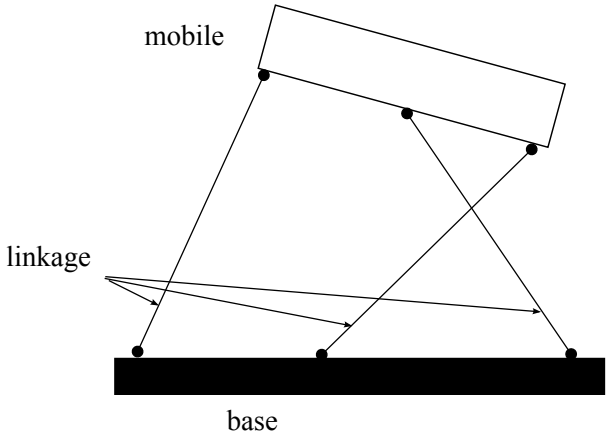

Figure 2.9: Planar parallel manipulator without singular configuration

2.5 Design Optimization Criteria

Depending on the application of a robotic manipulator, the design parameters can be optimized to meet specific performance criteria, for example the maximization of its

reachable workspace or to obtain optimal torque/force transmission ratio between actuators and end-effector. Furthermore, manipulability, conditioning index and global conditioning index are some of the performance criteria used in the design process to overcome singular configurations of the robot. Two types of design optimization criteria are discussed in this section. One is based on the workspace, and the other is based on the extremization of some index that encodes the performance of the system.

2.5.1 Workspace Optimization

Workspace optimization is also known as workspace synthesis of a manipulator. It involves the optimization of design parameters of the robot to achieve the desired workspace area. It further involves solving the inverse kinematics, which may not have a unique solution. Therefore, a unique solution is selected by adding a suitable set of constraints that encode additional performance criteria.

Optimization with respect to the workspace has been conducted by Gosselin and Guillot [23], that optimized a planar 2DOF parallel manipulator to obtain the workspace equivalent to a prescribed working area. Boudreau and Gosselin [8] further developed this methodology by using genetic algorithms on planar and spatial manipulators. Merlet [53] illustrates the method of determining workspace using constraints on the design dimensions and the ranges of motion of the manipulator. A common region where all constraints of the system are satisfied is found as manipulator's workspace area.

Lee *et al.* [48] described the design optimization of a mobile welding robot which requires workspace specific orientations for welding. The optimization is based on a cost function given by the ratio between the robot's design parameters and its workspace volume.

A multi-objective optimization method for workspace known as the DEMOCRAT is proposed by Merlet [53]. This method takes into account a set of performance criteria and analyzes the performance of the manipulator. These criteria are used to compute a discretized closed region. Then each discrete position is analysed to make sure it best fits the performance criteria. The problem with this method occurs as the design variables increase. Gallant and Boudreau [20] used a method which is based on genetic algorithms for optimizing a planar parallel 3DOF P$\underline{\text{R}}$P manipulators. This method produces an optimal singularity-free workspace and uses criteria of global conditioning index which is described in the following section.

2.5.2 Performance Optimization Criteria

Performance optimization is defined with respect to a specific performance measure. Some of the most common types of performance measures are manipulability, conditioning index of the Jacobian matrix, and dexterity.

Manipulability Measure

Manipulability is a configuration dependent measure which quantitatively characterize the effects of joint velocities on the end-effector velocities of a manipulator. This index was first introduced by Yoshikawa [83] and further details can be found in Yoshikawa [84] and Bayle *et al.* [3]. A similar type of characterization, known as impulse response, is performed on a Linear Time-invariant systems to calculate the output of the system for a given input. For a multi-input system, the output is characterized in terms of an input that has a unit norm. Let $\dot{q}$ be a set of joint velocities such that

$$\|\dot{q}\| = \dot{q}^T \dot{q} \leq 1 \tag{2.1}$$

For a given joint velocity $\dot{q}$, the end-effector velocity is obtained by $\xi = J\dot{q}$ with the Jacobian J acting as a scaling factor. For a nonsingular Jacobian a minimum least square solution for $\dot{q}$ is given by $\dot{q} = J^{\dagger}\xi$, where $J^{\dagger} = J^T(JJ^T)^{-1}$ is the left Moore-Penrose pseudo-inverse of J. Substitution into equation 2.1 gives

$$\begin{aligned} \|\dot{q}\| &= \dot{q}^T \dot{q} \\ &= \xi^T J^{\dagger^T} J^{\dagger} \xi \\ &= \xi^T (JJ^T)^{-1} \xi \leq 1 \end{aligned} \tag{2.2}$$

In the joint velocity space equation 2.1 represents a unit sphere,which is mapped into the manipulability ellipsoid $\xi^T(JJ^T)^{-1}\xi \leq 1$. The direction and magnitude of the principal axes of the ellipsoid are calculated as the eigenvectors and eigenvalues of JJ^T, respectively. The principal axes span the end effector velocity space, and an eigenvalue which is smaller indicates a corresponding restricted end-effector velocity. In general, it is desirable to have an ellipsoid which is closer to a sphere so that the end-effect may easily move along any direction of the operational space [63]. This can be achieved by maximizing the manipulability measure denoted by,

$$\sqrt{det(JJ^T)}$$

Bayle *et al.* [4] performed manipulability analysis on a wheeled mobile robot with a robotic arm attached on top. Mendes and Gomes [50] presented the optimization of 6DOF a Controlled Impedance Device using manipulability as a performance index. The purpose of using this performance index is to be able to operate in a small workspace area where the error between the joint velocity and operational velocity is minimized. Phem and Chen [37] investigated manipulability of a parallel flexure mechanism using a pseudo rigid body model. Dimensional synthesis is performed using manipulability as a performance criterion to take into account the dexterity and sensitivity of the parallel flexure mechanism.

Conditioning Index

The condition number of a manipulator is a measure of the kinematic accuracy and the proximity to a singularity. It is used to show how a relative error in the joint velocities with respect to the input may lead to a relative error in the end-effector velocities [53]. The condition number κ is the ratio of the maximum over the minimum singular value of the Jacobian matrix. The value of κ lies between $1 \leq \kappa < \infty$. When κ is close to unity, the manipulator approaches isotropy, meaning that the robot is kinematically more accurate and singularity-free [53]. Planar and spherical 3DOF $\underline{\text{R}}$RR manipulators were studied by Gosselin and Angeles [21] so that they were isotropic at a specific configuration. Gosselin and Lavoie [24] studied a spherical 3DOF manipulator to determine its isotropic configuration which minimizes the condition number. Fattah and Ghasemi [16] studied the isotropic conditions of two spatial parallel manipulators and the kinematic conditioning index with respect to the motion of the moving platform. Zanganeh and Angeles [85] defined a set of conditions where parallel manipulators can be isotropic.

Global Conditioning Index

A global conditioning index (GCI) was proposed by Gosselin and Angeles [21] in order to evaluate the complete workspace of the manipulator. This index was proposed since the determination of the isotropic condition of a manipulator is configuration dependent property. Therefore, the GCI was proposed to obtain isotropy of the manipulator over the entire workspace. Global conditioning index have been used to optimize several types of manipulators by Stamper et al. [71], Tsai and Joshi [77], Kurtz and Hayward [46] and Leguay-Durand and Reboulet [49].

2.6 Design Optimization Techniques

In this section we present some of the techniques used to optimize the design parameters of a robot. Van Henten et al. [78] used Dividing Rectangles (DIRECT) algorithm to optimize the dexterity of a four link PPRP manipulator. The optimal design of the manipulator is used for autonomous cucumber harvesting in greenhouses. DIRECT algorithm uses a deterministic approach to obtain a global minimum of an objective function defined with respect to a constrained variable. For example, if $f(x)$ represents an objective function then the variable x may only attain values between $a < x < b$. During the first iteration, the algorithm starts by evaluating the objective function using the mid-value $c = \frac{a+b}{2}$ of the range of possible variables as illustrated in figure 2.10. The algorithm stores the values of the function $f(c)$ and consider it as the current best minimum value of the objective function (f_{min}). The next step involves trisecting the interval to find two new mid-values of the sub-intervals as shown in figure 2.10. By doing this, point c remains the center point of one of the sub-intervals. The value of $f(x)$ is evaluated for each mid-values of the sub-intervals and f_{min} is updated. For the next iteration, the sub-intervals which minimizes the objective function are selected and the DIRECT algorithm repeats until the threshold for the next sub-interval length is reached. Further details regarding this method can be found in Jones et al. [40].

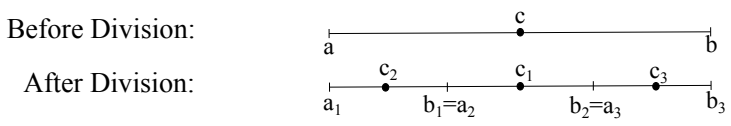

Figure 2.10: Subdividing an interval with center-point sampling

Kircanski [43] optimized the link length of 2DOF, 3DOF and 4DOF planar manipulators using a sequential quadratic programming (SQP) method. A condition number was used as the criterion for optimization which was obtained as an explicit analytic function of joint coordinates and link length ratios. SQP is a non-linear programming method for smooth constrained optimization problems. The main feature of SQP algorithm is that at a given iteration it contains a Quadratic Programming sub-problem which is used to compute the search direction. This method finds the search direction by linearizing the objective and constraint function and by using a bounded symmetric positive-definite Hessian [11]. A more thorough study on SQP algorithm and its history can be found in Han [26] and powell [58]. Zhao [87] also performed dimensional synthesis on 3DOF parallel delta robot taking into account kinematic isotropy as a performance criteria. SQP

algorithm is used to solve this non-linear constrained optimization problem. Manipulability index can also be used as an objective function, which leads to maximum velocity transmission between the joint and the operational space of the robot. Moreover, robot's dimensions relative to the size of the desired workspace is considered as a constraint.

Kelaiaia *et al.* [42] performed multi-objective optimization on a 3DOF linear Delta parallel robot using a genetic algorithm and the Strenght Pareto evolutionary algorithm (SPEA-2). Multiple performance criterion were taken into consideration such as workspace, stiffness, condition number and manipulability index. A general background and procedure on how to implement genetic algorithms and SPEA-2 are given in [81, 89], respectively. Stan *et al.* [73] also used genetic algorithms to optimize the workspace of a bipod mini robot by considering transmission quality index, design space and workspace as performance index.

Miller [41] used exhaustive search algorithms and weighted factors in the multi-objective function to optimize NUWAR robot and linear delta robot. The multi-objective function uses manipulability measure and workspace as performance criteria for optimization. Huang [36] used constrained non-linear optimization on a Trivariant robot, where dimensional synthesis was performed by minimizing the condition index subjected to a set of mechanical constraints. Chablat *et al.* [10] used an interval based method and both workspace and kinetostatic performance indexes to optimize Orthoglide and UranSX 3DOF parallel kinematic manipulators. The optimization resulted in the largest dexterous workspace within the Cartesian workspace of the manipulators.

Hao and Merlet [28] proposed a new method for optimal design of parallel manipulators which satisfies multi-criteria requirements. This methodology is known as Interval Analysis which gives a solution to the best design for compulsory and relaxable requirements. For a given range of design parameters, Interval Analysis computes a range of solutions for each design parameter. The process is detailed by Merlet [53] and implemented by Hao and Merlet [28].

Huang [35] performed dimensional synthesis on a 5DOF planar parallel robot using parametric variation as an optimization technique. Optimal design was presented using workspace and kinematic conditioning index as optimization criteria. Parametric variation method is used to solve for a multi-variable non-linear optimization problem. During parametric variation one variable is varied to maximize an index, while keeping other variables constant. This procedure is repeated for other variables, and the variables which maximize the index are used in the next iteration to obtain another optimal set. The process stops when convergence is attained. This method is similar to successive

substitution method for root finding applications.

Gradient descent method can also be used as a technique for optimization [69]. This method locates a local minimum of an objective function which must be differentiable, by iterating along the gradient, which represent the direction of maximum variation. The function used may represent multiple performance criteria of the robot such as kinematic conditioning index and manipulability. The iterative search process stops when the gradient approaches zero, which corresponds to a local minimum of the cost function. Further details on the topic of gradient descent can be found in [5, 6].

2.7 Chapter Summary

In this chapter, the development of snake-like robots for confined environments has been discussed. The determination of workspace and singularities based on geometric method, discretization method and numerical method have been discussed. The discretization approach in determining the workspace is specifically relevant for this thesis, where a Cartesian grid is used to verify the existence of the inverse kinematic solution at each gridded point. The analytical method of finding the determinant roots of the inverse Jacobian is also relevant in the determination of singularities. Moreover, the kinematic conditioning index will assist in obtaining the robot's proximity to a singular configuration. Furthermore, the criteria used for the dimensional synthesis of a robot are classified into two groups. One is based on workspace optimization index and the other is based on performance optimization index. Finally, among the techniques used to optimize different types of robots, the parametric variation method will be used for design optimization of the robot presented in this thesis.

Chapter 3

Description of the Mobile Planar Parallel Robot and its Environment

3.1 Introduction

In this chapter the kinematics of the mobile parallel robot studied in this thesis is described in detail. The kinematical model was proposed by Douadi *et al.* [13]. The optimization of geometric and configuration parameters presented in subsequent Chapters are based on the kinematics illustrated here. Section 3.2 provides a detailed description of the robot. The position and velocity kinematics of the planar parallel robot are given in Sections 3.3 and 3.4, respectively. Five different type of confined environments are presented in section 3.5 for the purpose of optimization of design parameters of the mechanism.

3.2 Mechanism Description

Figure 3.1 shows a parallel mechanism with a mobile base. This mobile parallel robot is able to manoeuvre in a planar region defined as $\Pi \in \Re^2$. The main body of the robot with height h and width w is connected to two arms of length l pinned to it at points H_1 and H_2. The distance to the position of H_1 and H_2 is defined by ah from the bottom of the body, where $a \in [0, 1]$ is a non-dimensional design parameter. The parameters l, w, h and a define the geometry of the robot. These design parameters are normalized with respect to the width of the confined environment denoted by W_p. To ensure successful manoeuvrability of the robot the two wheels at the end of the arms are assumed to be

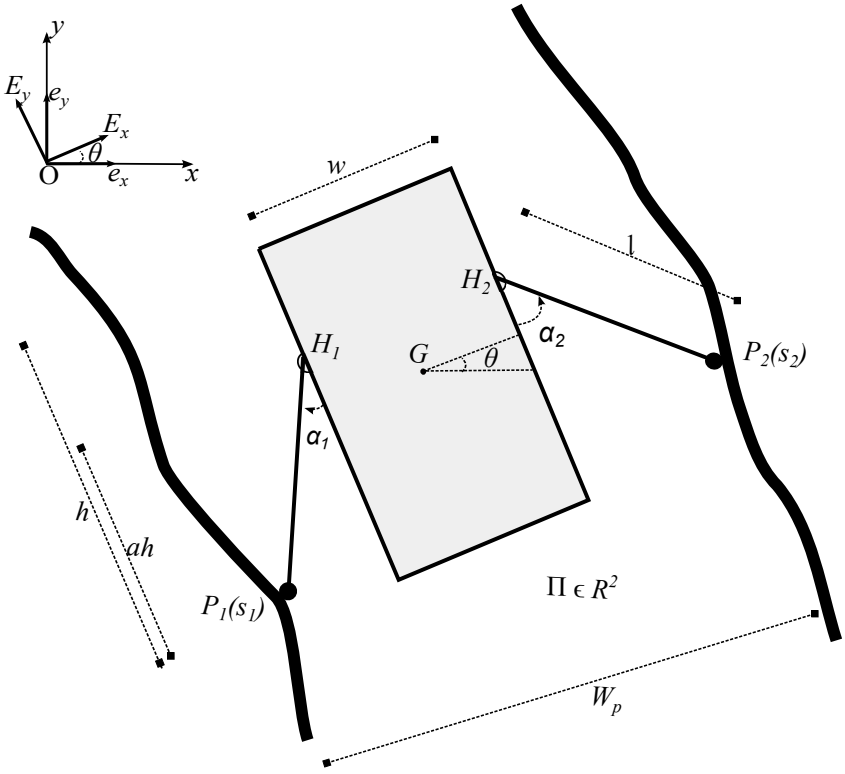

Figure 3.1: Planar Robot's Model

always in contact with the boundaries of the region Π at point P_1 and P_2. The boundaries of the region Π are parametrized by arc lengths s_1 and s_2. It is assumed that both wheels of the module are subjected to rolling without slipping constraints. At the contact points P_1 and P_2, the normal component of velocity with respect to the boundary of the curve is constrained to be zero, in order to enforce the contact with the wall (provided that the contact exists at the initial configuration). Therefore, a simplified model of a wheel is taken into consideration by assuming the wheel radius to be very small. This assumption leads to approximating the center of mass of the wheels with the contact points, P_1 and P_2. The joints H_1, H_2, P_1, and P_2 are active. A global reference frame with orthogonal basis vectors ($\mathbf{e}_x$, $\mathbf{e}_y$) are shown in figure 3.1. The center of mass of the main body is symbolized as G with global coordinates (x_G, y_G). The global orientation angle of the rigid body is defined by $\theta \in [0, 2\pi)$. The angle $\alpha_1 \in [0, \frac{\pi}{2})$ and $\alpha_2 \in [0, \frac{\pi}{2})$ are the relative orientation of the arms with respect to the rigid body.

In order to determine the mechanism's degrees of freedom (DOF) the number of rigid bodies and constraints are analysed. The mechanism is composed of 5 rigid parts: 1

main body, 2 arms and 2 wheels. Each of these rigid bodies has 3 DOF giving a total of 15 DOF. This mechanism has four revolute joints, two at points H_1 and H_2 and two at points P_1 and P_2. Each revolute joint corresponds to 2 constraints leading to a total of 8 constraints. The two wheels of the robot in contact with the walls subjected to rolling without slipping correspond to 4 more constraints. By subtracting these constraints from the total DOF of the rigid bodies, the mechanism's DOF is found to be $15 - 8 - 4 = 3$.

3.3 Position Kinematics

Since the mechanism has 3DOF the end-effector is represented by two positional coordinates and an orientation angle denoted by $\mathbf{x} = (x_G, y_G, \theta)$. x_G and y_G give the position of point G which is the center of gravity of the robot. The generalized joint coordinates $\mathbf{q}$ contains two joint angles α_1 and α_2 along with the positions of the wheels defined on boundaries of the region by arc length parameters s_1 and s_2. Therefore $\mathbf{q} = (\alpha_1, \alpha_2, s_1, s_2)$. Let $(\mathbf{E}_x\ \mathbf{E}_y)$ be an orthonormal basis attached to the robot's moving body, as shown in figure 3.1. Then

$$(\mathbf{E}_x\ \mathbf{E}_y) = (\mathbf{e}_x\ \mathbf{e}_y)\ \mathbf{R}(\theta)$$

where $\mathbf{R}$ is the rotation matrix

$$\mathbf{R}(\theta) = \begin{pmatrix} \cos(\theta) & -\sin(\theta) \\ \sin(\theta) & \cos(\theta) \end{pmatrix}$$

We denote with $\mathbf{r}_{GH_2}$ the displacement vector from point G to point H_2. By referring to figure 3.1 we have.

$$\begin{aligned}
\mathbf{r}_{GH_2} &= \frac{w}{2}\mathbf{E}_x + h\left(a - \frac{1}{2}\right)\mathbf{E}_y \\
&= \left(\tfrac{w}{2}\cos(\theta) - h(a - \tfrac{1}{2})\sin(\theta)\right)\mathbf{e}_x + \left(\tfrac{w}{2}\sin(\theta) + h(a - \tfrac{1}{2})\cos(\theta)\right)\mathbf{e}_y \\
\mathbf{r}_{H_2P_2} &= -l\mathbf{R}(\alpha_2)\mathbf{E}_y \\
&= l\mathbf{R}(\alpha_2)\sin(\theta)\mathbf{e}_x - l\mathbf{R}(\alpha_2)\cos(\theta)\mathbf{e}_y \\
&= l(\sin(\alpha_2 + \theta)\mathbf{e}_x - \cos(\alpha_2 + \theta)\mathbf{e}_y) \\
\mathbf{r}_{GH_1} &= -\frac{w}{2}\mathbf{E}_x + h\left(a - \frac{1}{2}\right)\mathbf{E}_y \\
&= -\left(\tfrac{w}{2}\cos(\theta) + h(a - \tfrac{1}{2})\sin(\theta)\right)\mathbf{e}_x + \left(-\tfrac{w}{2}\sin(\theta) + h(a - \tfrac{1}{2})\cos(\theta)\right)\mathbf{e}_y
\end{aligned}$$

$$\begin{aligned}
\mathbf{r}_{H_1P_1} &= -l\mathbf{R}(-\alpha_1)\mathbf{E}_y \\
&= l\mathbf{R}^T(\alpha_1)\sin(\theta)\mathbf{e}_x - l\mathbf{R}^T(\alpha_1)\cos(\theta)\mathbf{e}_y \\
&= l(\sin(\alpha_1-\theta)\mathbf{e}_x - \cos(\alpha_1-\theta)\mathbf{e}_y) \\
\mathbf{r}_{P_1P_2} &= \Big(x_{P_2}(s_2) - x_{P_1}(s_1)\Big)\,\mathbf{e}_x + \Big(y_{P_2}(s_2) - y_{P_1}(s_1)\Big)\,\mathbf{e}_y
\end{aligned}$$

The wheels of the robot are assumed to be always in contact with the inner boundaries of the region Π at points P_1 and P_2. These points are defined by the parametrization of the boundaries. By referring to figure 3.1 the vector $\mathbf{r}_{OG}$, which expresses the position of the center of mass G in the world coordinate frame, is given by.

$$\begin{aligned}
\mathbf{r}_{OG} &= \mathbf{r}_{OP_1} - \mathbf{r}_{H_1P_1} - \mathbf{r}_{GH_1} \\
\mathbf{r}_{OG} &= \mathbf{r}_{OP_2} - \mathbf{r}_{H_2P_2} - \mathbf{r}_{GH_2}
\end{aligned} \tag{3.1}$$

By combining equations (3.1) a closure equation is obtained for the parallel robot

$$\mathbf{r}_{P_1P_2} + \mathbf{r}_{H_1P_1} + \mathbf{r}_{GH_1} - \mathbf{r}_{H_2P_2} - \mathbf{r}_{GH_2} = 0 \tag{3.2}$$

By projecting (3.2) and the first (3.1), and by considering the parameters $s_1, s_2, \alpha_1, \alpha_2, \theta, x_G$ and y_G, the explicit set of four relations can be determined

$$\begin{aligned}
x_G &= x_{P_1}(s_1) + \frac{w}{2}\cos(\theta) + h(a-\frac{1}{2})\sin(\theta) + l\sin(\alpha_1-\theta) \\
y_G &= y_{P_1}(s_1) + \frac{w}{2}\sin(\theta) - h(a-\frac{1}{2})\cos(\theta) + l\cos(\alpha_1-\theta) \\
\sin(\alpha_1-\theta) &+ \sin(\alpha_2-\theta) + \frac{w}{l}\cos(\theta) - \frac{1}{l}(x_{P_2}(s_2) - x_{P_1}(s_1)) = 0 \\
\cos(\alpha_1-\theta) &- \cos(\alpha_2-\theta) + \frac{w}{l}\sin(\theta) - \frac{1}{l}(y_{P_2}(s_2) - y_{P_1}(s_1)) = 0
\end{aligned} \tag{3.3}$$

It can be noted that the direct kinematics solution of the robot can be obtained by solving (3.3) for $\mathbf{x} = (x_G, y_G, \theta)$. Similarly, solving for $\mathbf{q} = (\alpha_1, \alpha_2, s_1, s_2)$ gives the inverse kinematic solutions.

3.4 Velocity Kinematics

The velocity kinematics is obtained by time deriving the position kinematics equations (3.3)

$$-\dot{x}_G + \dot{\theta}\left(h\left(a-\frac{1}{2}\right)\cos(\theta) - \frac{w}{2}\sin(\theta) - l\cos(\alpha_1-\theta)\right) + l\dot{\alpha_1}\cos(\alpha_1-\theta) + \dot{s_1}\frac{dx_{p_1}(s_1)}{ds_1} = 0$$

$$-\dot{y}_G + \dot{\theta}\left(h\left(a-\frac{1}{2}\right)\sin(\theta) + \frac{w}{2}\sin(\theta) + l\cos(\alpha_1-\theta)\right) - l\dot{\alpha_1}\sin(\alpha_1-\theta) + \dot{s_1}\frac{dy_{p_1}(s_1)}{ds_1} = 0$$

$$\dot{\theta}\left(l\cos(\alpha_1-\theta) - l\cos(\alpha_2+\theta) + w\sin(\theta)\right) - l\dot{\alpha_1}\cos(\alpha_1-\theta) - l\dot{\alpha_2}\cos(\alpha_2-\theta) + \dot{s_1}\frac{dx_{p_1}(s_1)}{ds_1} + \dot{s_2}\frac{dx_{p_2}(s_2)}{ds_2} = 0$$

$$\dot{\theta}\left(-l\sin(\alpha_1-\theta) - l\sin(\alpha_2+\theta) - w\cos(\theta)\right) + l\dot{\alpha_1}\sin(\alpha_1-\theta) - l\dot{\alpha_2}\sin(\alpha_2+\theta) - \dot{s_1}\frac{dy_{p_1}(s_1)}{ds_1} + \dot{s_2}\frac{dy_{p_2}(s_2)}{ds_2} = 0$$

The end-effector velocity is defined by $\dot{\mathbf{x}} = (\dot{x}_G, \dot{y}_G, \dot{\theta})$, and the joint velocity is defined by $\dot{\mathbf{q}} = (\dot{\alpha_1}, \dot{\alpha_2}, \dot{s_1}, \dot{s_2})$. Therefore, the velocity kinematics of the robot can be written in the form

$$J_x\ \dot{\mathbf{x}} = J_q\ \dot{\mathbf{q}}$$

where $J_x \in \Re^{4\times3}$ and $J_q \in \Re^{4\times4}$ are the parallel and serial Jacobians, respectively

$$J_x = \begin{bmatrix} -1 & 0 & h(a-\frac{1}{2})\cos(\theta) - \frac{w}{2}\sin(\theta) - l\cos(\alpha_1-\theta) \\ 0 & -1 & h(a-\frac{1}{2})\sin(\theta) + \frac{w}{2}\cos(\theta) + l\sin(\alpha_1-\theta) \\ 0 & 0 & l\cos(\alpha_1-\theta) - l\cos(\alpha_2+\theta) + w\sin(\theta) \\ 0 & 0 & -l\sin(\alpha_1-\theta) - l\sin(\alpha_2+\theta) - w\cos(\theta) \end{bmatrix} \tag{3.4}$$

$$J_q = \begin{bmatrix} l\cos(\alpha_1-\theta) & 0 & \frac{dx_{p_1}(s_1)}{ds_1} & 0 \\ -l\sin(\alpha_1-\theta) & 0 & \frac{dy_{p_1}(s_1)}{ds_1} & 0 \\ -l\cos(\alpha_1-\theta) & -l\cos(\alpha_2+\theta) & -\frac{dx_{p_1}(s_1)}{ds_1} & \frac{dx_{p_2}(s_2)}{ds_2} \\ l\sin(\alpha_1-\theta) & -l\sin(\alpha_2+\theta) & -\frac{dy_{p_1}(s_1)}{ds_1} & \frac{dy_{p_2}(s_2)}{ds_2} \end{bmatrix} \tag{3.5}$$

3.5 Simulation Scenarios

Straight Pipe (Varying Diameter): One of the challenges a mobile parallel robot may face is a pipe-like structure with different diameters as shown in figure 3.2. The robot introduced in previous section has the capability to manoeuvre in such environment. Therefore dimensional synthesis on the robot's parameter is performed based on this type of structure for maximum workspace. The diameter of the pipe is set to W_p, and the pipe diameter decreases to $0.75 \times W_p$ half way in to the pipe.

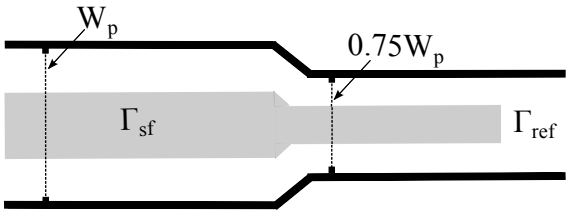

Figure 3.2: Varying diameter Pipe-like Structure

90^o **Elbow Pipe:** This structure is shown in figure 3.3, which is also one of the most common elbow joints found in the pipeline inspection industry. This type of elbow joint combines two mutually perpendicular pipes together. The width or diameter of the pipe is denoted by W_p and is kept constant throughout the pipe. The radius of curvature is set to $\varphi = \frac{1}{r}$ from the center-line of the pipe, where r represents the radius which is equal to W_p. The radius of curvature in all elbow pipe-like structures are set according to the American National Standard Institution, ANSI B16.9. According to this standard, an elbow joint which has r equal to one times the outer diameter of the pipe is called Short Radius elbow pipe. Another standard dimension of an elbow joint is the Long Radius elbow pipe, which is equal to $1.5 \times W_p$. The most difficult elbow to manoeuvre for the robot is Short Radius elbow, therefore the robot's parameters are optimized according to this standard dimension.

135^o **Elbow Pipe:** This structure is shown in figure 3.4. This type of pipe structure combines two straight pipes with 135^o elbow joint. The outer diameter W_p, of the pipe is constant throughout its length.

180^o **Elbow Pipe:** This structure is shown in figure 3.5. This type of pipe structures

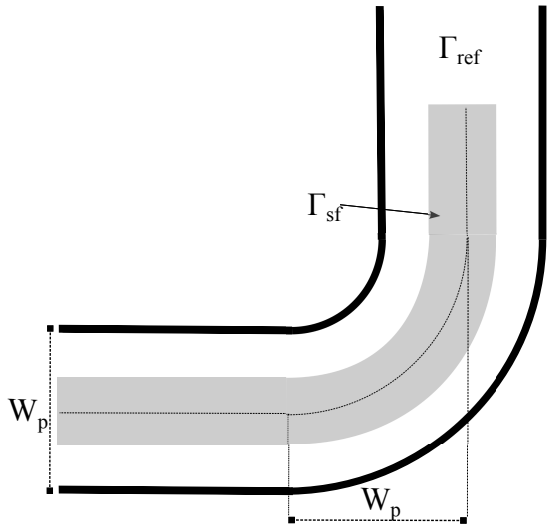

Figure 3.3: 90^o Pipe-like Structure

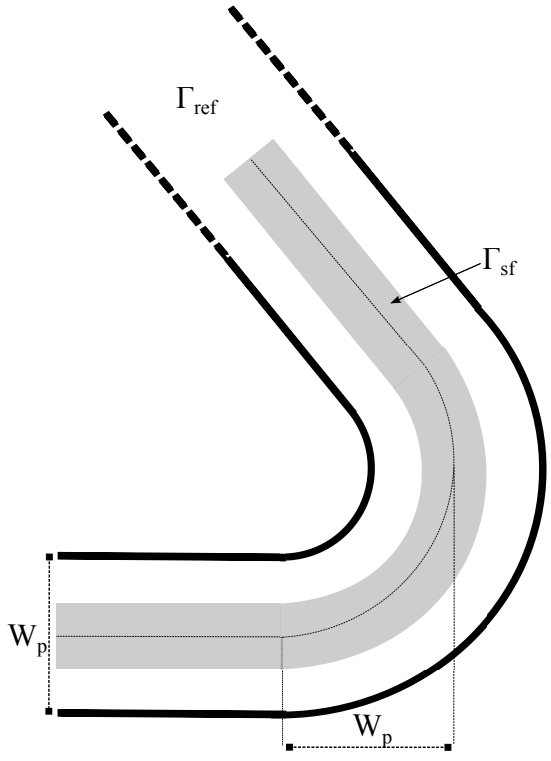

Figure 3.4: 135^o Pipe-like Structure

combines two parallel pipes with a 180^o elbow joint. The outer diameter of the pipe is constant throughout the length of the pipe and is denoted by W_p.

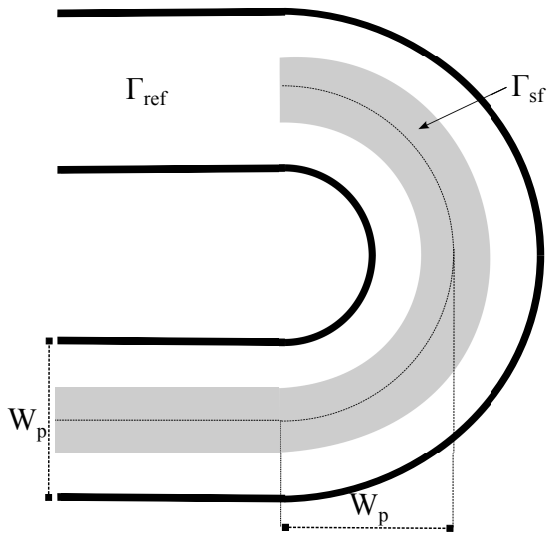

Figure 3.5: 180^o Elbow Pipe-like Structure

Sharp 90^o Elbow Pipe: This structure is shown in figure 3.6. This type of pipe structure combines two straight pipes perpendicular to each other. The outer diameter is constant throughout the length of the pipe and is denoted by W_p. This pipe-like structure introduces a critical manoeuvrability scenario due to singular geometry.

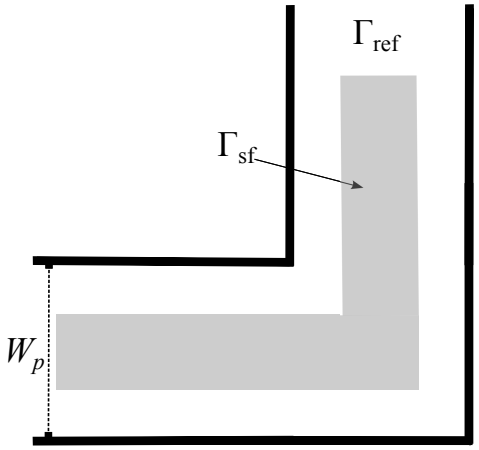

Figure 3.6: Sharp 90^o Elbow Pipe-like Structure

3.6 Chapter Summary

This chapter details the 3 DOF mobile planar parallel robot proposed by Douadi *et al.* [13]. The mechanism's rigid components such as the body and the arms are especially highlighted as they are the design parameters which will be optimized in the following chapters. The position and velocity kinematics of the mechanism are also detailed, followed by the illustration to five different types of confined environments that reproduce typical manoeuvrability scenario. Four types of elbow pipe and a straight pipe with varying diameters are introduced as a confined environment in which the robot's manoeuvrability and performance will be analyzed and optimized in the following chapters.

Chapter 4

Workspace and Singularity Analysis

4.1 Introduction

This chapter focuses on the analysis of the workspace and singularities. For the workspace analysis, discretization method will be used which transforms the prescribed workspace region into a Cartesian grid and verifies the existence of the inverse kinematic solution at each gridded cell. The analytical method of determinant roots of the inverse Jacobian will be used to obtain all singular configurations of the robot. Furthermore, kinematic conditioning index will also be used in order to determine the robot's proximity to a singular configuration. The purpose is to obtain a continuous and singularity-free workspace. Since the workspace and singularities highly depend on the geometry of the robot, it is important to find optimal design dimensions to successfully overcome critical scenarios. This analysis will play a key role in the optimization of the design parameters as detailed in chapter 5.

Section 4.2 details the method used to define the workspace. Section 4.3, illustrates different types of singular configurations admissible for the robot. Sections 4.4 and 4.5 discuss simulation results of the workspace and singularity analysis using different types of pipe structures described earlier.

4.2 Workspace Analysis

The workspace analysis is performed using a disretization method described in section 2.3 by first initializing the reference workspace, Γ_{ref}, in which the singularity-free workspace Γ_{sf} needs to be determined. By considering different types of pipe-like structures, Γ_{ref} is

initialized by forming a grid on the surface area inside the pipe with a cell size of $0.03W_p$ as shown in figure 4.7. A similar method of workspace determination using discretization method was adopted by Huang M.Z. [35]. The method to compute, Γ_{sf} is structured numerically in three steps. In the first step, each cell of the reference workspace is checked for collision avoidance by placing the center of mass G of the robot's body at the centroid of the cell and by considering possible collision of the four corners with the walls. When a collision occurs, the respective cell is discarded from Γ_{sf}. A possible configuration of the robot is shown in figure 4.1 depicting a collision occurrence. The arrow pointing to the left wall and the corner of the robot's module depicts a collision due to reaching the maximum orientation, while the arrow on the right shows a collision between the pipe wall and the robot's arm.

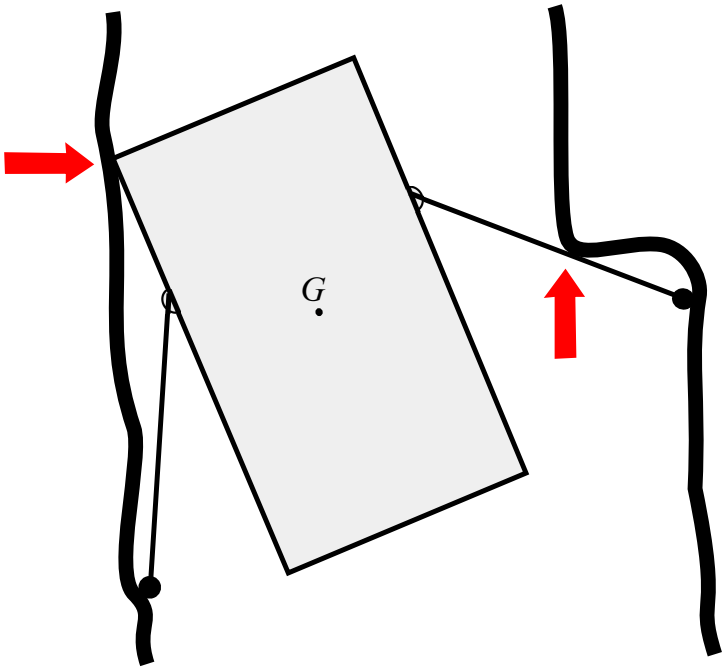

Figure 4.1: Possible Collision Scenario

During the second step a direct search algorithm is used to move G to each gridded cell position and verify the existence of the inverse kinematic solution using equations (3.3). During the third step, the robot's proximity to a singular configuration at a given cell is analyzed using kinematic conditioning index. The details about this index and the singularity analysis of this robot is discussed in the following section. When all the discrete points of Γ_{ref} are analyzed, the final step is to check for the continuity of Γ_{sf} using the connected component labelling method [29]. Figure 4.2 illustrates a continuous

singularity-free workspace determination algorithm using the discretization method.

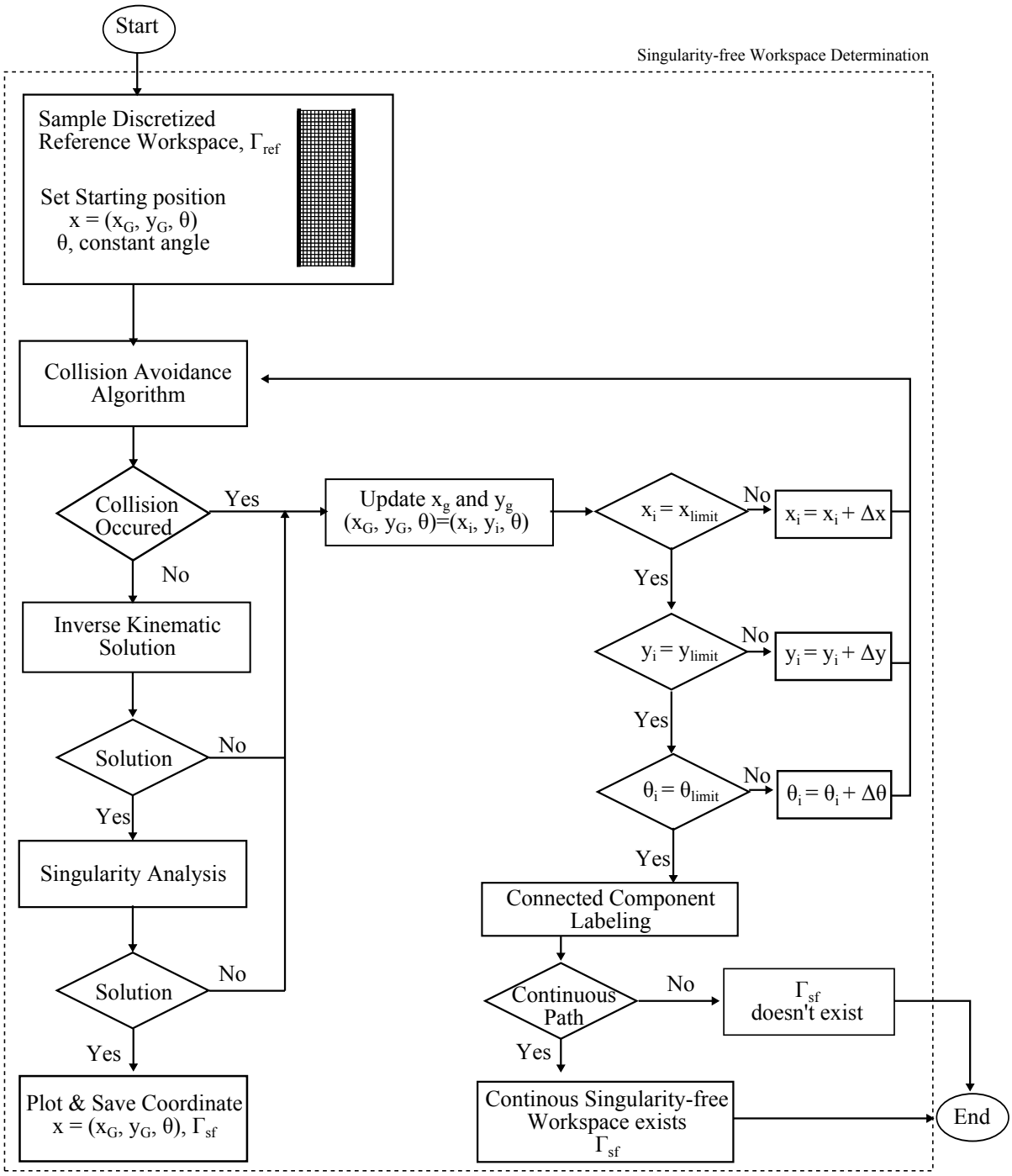

Figure 4.2: Algorithm for Singularity-free Workspace determination

4.3 Singularity Analysis

When the configuration of the robot results in a singularity, the robot is uncontrollable since a subset of the degrees of freedom becomes momentarily inaccessible. Therefore, it is important to avoid such configurations during the path planning stage. Furthermore, the design of the robot can be optimized to avoid such singular configurations, especially when operating in critical (geometrical) conditions such as an elbow. The following expression restates the velocity kinematics of the mobile planar parallel robot. As established in chapter 3 the velocity kinematics can be written as

$$J_x \ \dot{\mathbf{x}} = J_q \ \dot{\mathbf{q}}$$

where the Jacobians are given in equations 3.4 and 3.5, and the velocities are collected into the vectors

$$\dot{\mathbf{x}} = [\dot{x}_G \ \dot{y}_G \ \dot{\theta}] \ , \ \dot{\mathbf{q}} = [\dot{\alpha}_1 \ \dot{\alpha}_1 \ \dot{s_1} \ \dot{s_2}]$$

The dimension of x equals the number of degrees of freedom of the system.

4.3.1 Serial Singularity Configurations

In a parallel robot two types of singularity exist, known as serial and parallel singularities [21]. A Serial Singularity is also known as the inverse kinematic singularity. The singularity of this type occurs when the rank of J_q is lower than the end-effector's degrees of freedom [86]. In other words, a zero twist of the end-effector velocity is obtained for a non-zero actuated joint velocities. The serial singular configurations are studied by considering the minimum least square inverse relation

$$\dot{\mathbf{q}} = J_q^{\dagger} \ J_x \ \dot{\mathbf{x}} \tag{4.1}$$

where $J_q^{\dagger} = J_q^T (J_q^T \ J_q)^{-1}$ is the right pseudo-inverse of J_q. Therefore, serial singularities exist corresponding to singularities of the matrix $J_q J_q^T$, that can be identified as the roots of the equation

$$det(J_q {J_q}^T) = 0 \tag{4.2}$$

For the Jacobian in equation (3.4) the expression in 4.2 is explicitly written as

$$-l^2 \left(\frac{dy_{p_1}(s_1)}{ds_1} cos(\alpha_1 - \theta) + \frac{dx_{p_1}(s_1)}{ds_1} sin(\alpha_1 - \theta) \right) \left(\frac{dx_{p_2}(s_2)}{ds_2} sin(\alpha_2 + \theta) - \frac{dy_{p_2}(s_2)}{ds_2} cos(\alpha_2 + \theta) \right) = 0 \tag{4.3}$$

which implies

$$\begin{aligned} \frac{dy_{p_1}(s_1)}{ds_1} cos(\alpha_1 - \theta) &= -\frac{dx_{p_1}(s_1)}{ds_1} sin(\alpha_1 - \theta) \\ \frac{dy_{p_2}(s_2)}{ds_2} cos(\alpha_2 + \theta) &= \frac{dx_{p_2}(s_2)}{ds_2} sin(\alpha_2 + \theta) \end{aligned} \tag{4.4}$$

The variables and symbols in equation 4.3 and 4.4 are defined in chapter 3. The first expression in equation 4.4 is a condition of singular configuration that corresponds to the left arm of the robot being normal to the pipe wall. This is true when $(\alpha_1 - \theta) = k\pi$, where $k = 0, 1$ and the velocity of the wheel in x direction is zero as illustrated in figure 4.3. Similarly, the second expression in equation 4.4 is a condition of a singular

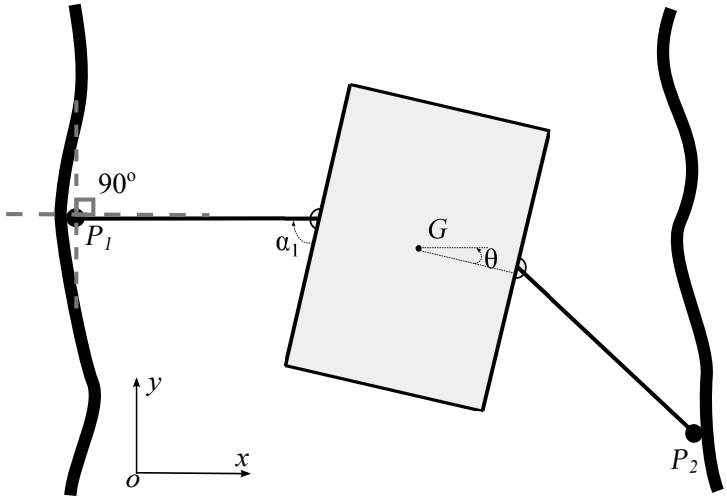

Figure 4.3: Serial singularity exist when the left arm is normal to the respective wall

configuration corresponding to the right arm being normal to the pipe wall as illustrated in figure 4.4. Another possible serial singular configuration is when both arms are normal to the boundaries of the pipe at the same time as shown in figure 4.5.

4.3.2 Parallel Singularity Configurations

A parallel singularity is also known as a direct kinematic singularity [86]. A singularity of this type occurs when a nonzero velocity of the end effector is admitted for a zero joint velocity. This type of singularity can occur only in parallel manipulators. The parallel singular configurations are studied by considering the minimum least square inverse relation

$$\dot{\mathbf{x}} = J_x^{\dagger} \; J_q \; \dot{\mathbf{q}} \tag{4.5}$$

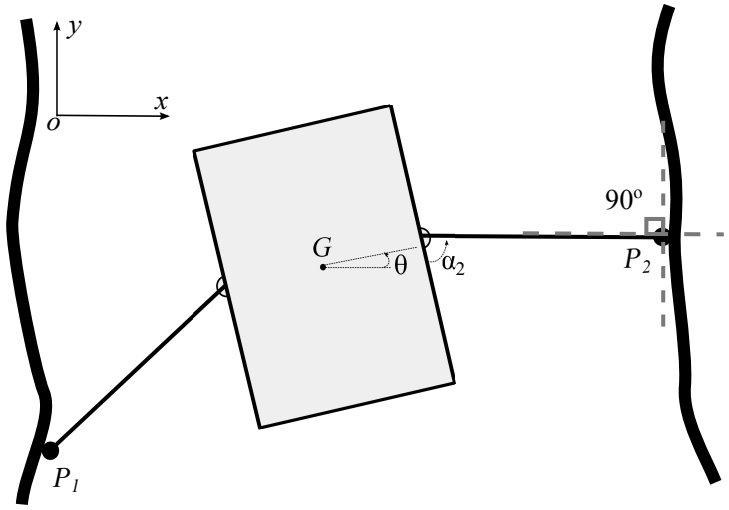

Figure 4.4: Serial singularity exist when the right arm is normal to the respective wall

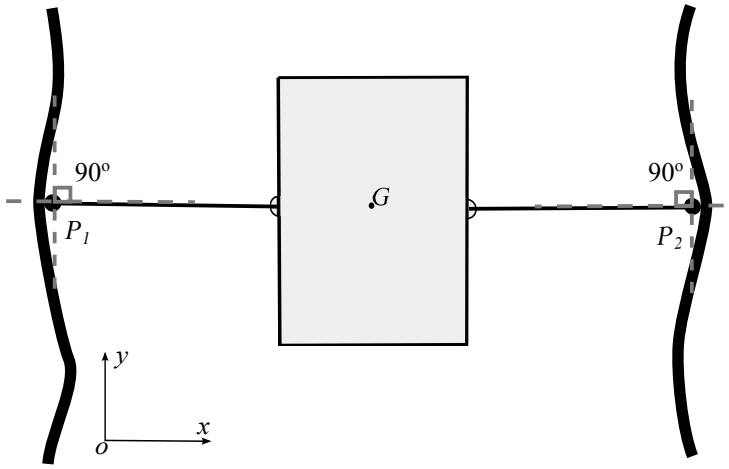

Figure 4.5: Both arms perpendicular to the respective walls

where $J_x^{\dagger} = {J_x}^T \left(J_x {J_x}^T\right)^{-1}$ is the right pseudo-inverse of the matrix J_x. From the same argument used above, parallel singularities can be identified as the roots of the nonlinear equation

$$det(J_x J_x^T) = 0 \tag{4.6}$$

The explicit form of equation (4.6) gives

$$w^2 + 2l^2(1 - cos(\alpha_1 + \alpha_2)) + 2wl(sin(\alpha_1) + sin(\alpha_2)) = 0 \tag{4.7}$$

Therefore, a parallel singularity exists if the following conditions are both satisfied.

$$\begin{cases} w & = 0 \\ (\alpha_1 + \alpha_2) & = \pm i\pi,\ i = 0, 2, 4... \end{cases}$$

The above case of singularity is physically not realizable since $w = 0$ and $\alpha_1 + \alpha_2 = 2\pi$ means that the width of the body is zero and the arms are overlapped. By setting the following physical constraints on the arms relative rotations, $0^o \leq \alpha_1 \leq 90^o$ and $0^o \leq \alpha_2 \leq 90^o$, parallel singularities cannot occur. Figure 4.6 show one of the configuration leading to parallel singularity.

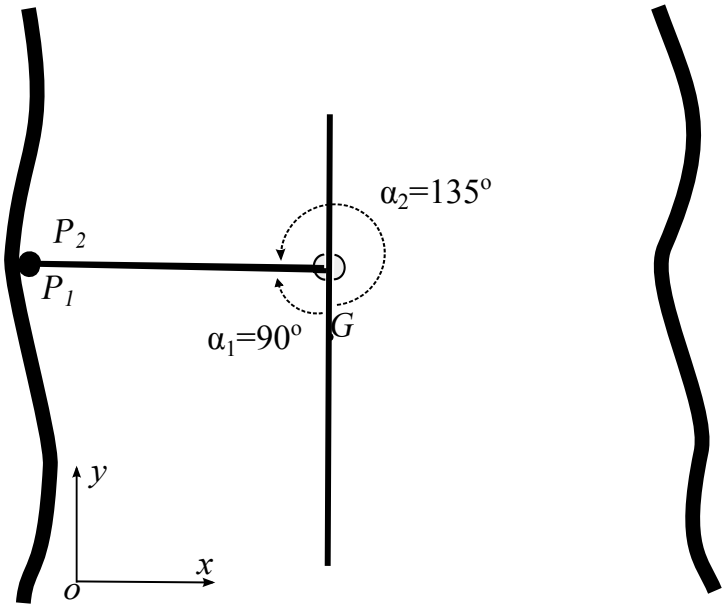

Figure 4.6: Illustration of a parallel singular configuration

4.3.3 Proximity to a Singular Configuration

The condition number is a measure of the kinematic accuracy and the proximity to a singular configuration. Consider a linear system

$$\Theta = J^{-1}X$$

where J^{-1} is an $n \times n$ inverse kinematic Jacobian, X represents the end-effector velocity and Θ are the joint velocities. Using a norm $\|.\|$ such that,

$$\|\Delta\Theta\| = \|J^{-1}\Delta X\| \leq \|J^{-1}\|\|\Delta X\|$$

from which we get

$$\frac{\|\Delta\Theta\|}{\|\Theta\|} \leq \|J^{-1}\| \frac{\|\Delta X\|}{\|\Theta\|}$$

$$\frac{\|\Delta\Theta\|}{\|\Theta\|} \leq \|J^{-1}\|\|J\| \frac{\|\Delta X\|}{\|X\|} \tag{4.8}$$

Equation 4.8 represents the error amplification factor and shows how a relative error in Θ gets multiplied and leads to a relative error in X. The error amplification factor is also called the condition number [53], defined by

$$\kappa = \|J^{-1}\|\|J\| = \frac{\sigma_{max}}{\sigma_{min}}$$

κ is defined as the ratio of the maximum over the minimum singular value of Jacobian where σ_{max} and σ_{min} are the singular values of the Jacobian matrix. The value of κ lies between $1 \leq \kappa < \infty$. when κ is close to unity, the manipulator is more isotropic, meaning that the robot is kinematically more accurate and singularity-free since a relative error in the actuated joint velocities results in a minimal effect on the end-effector velocities of a robotic manipulator [53]. The kinematic conditioning index is defined as the reciprocal of the condition number.

$$KCI = \frac{1}{\kappa}$$

KCI is bounded between $0 \leq KCI \leq 1$. Ideally, a resulting value close to 1 means that the manipulator is singularity-free with minimum positioning error of the robot's center of gravity G with respect to the actuated joints, whereas a value close to 0 depicts a robot being close to a singular configuration.

4.4 Determination of Γ_{sf} in various pipe-like structures

This section is devoted to the singularity-free workspace (Γ_{sf}) analysis of the mobile planar parallel robot in four different types of pipe-like structures, with constant width denoted by W_p. The analysis is performed using the discretization method is formalized by the algorithm in figure 4.2. Γ_{ref} is initialized by dividing the area between the boundaries of the pipe-like structures in a grid as shown in figure 4.7. The values of the geometric parameters for finding the inverse kinematic solution are normalized with respect to W_p and defined as $l = 0.7W_p$, $w = 0.5W_p$, $h = W_p$ and $a = 1$. These geometric parameters are selected to ensure that the robot fits inside the pipe-like structures.

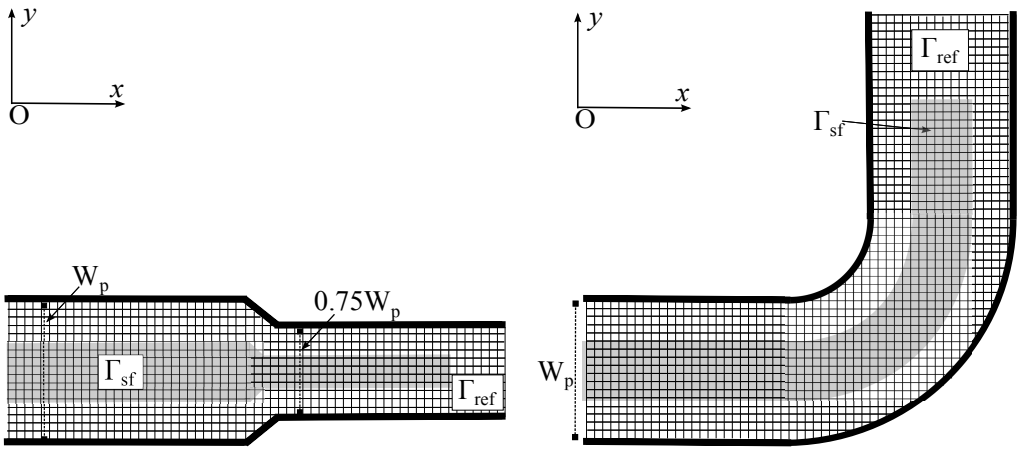

(a) Initialization of Straight Pipe

(b) Initialization of 90^o Elbow Pipe

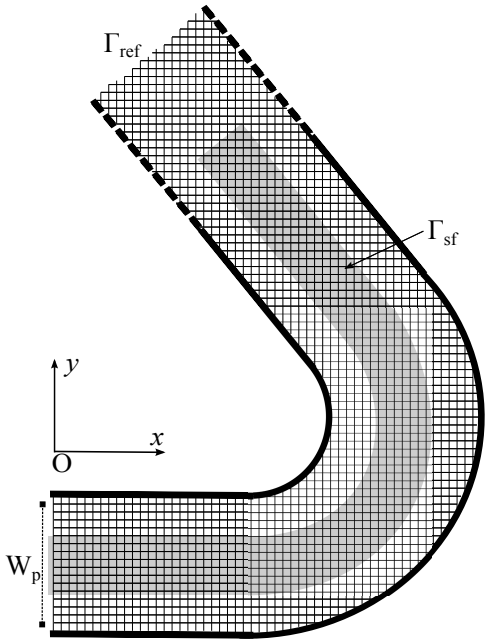

(c) Initialization of 135^o Elbow Pipe

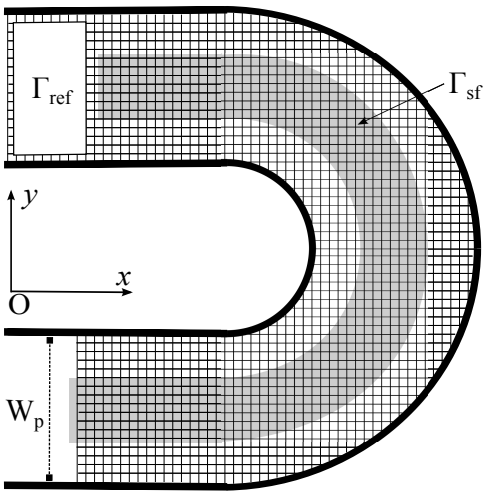

(d) Initialization of 180^o Elbow Pipe

Figure 4.7: Initialization of Γ_{ref} in four types of pipe-like structures

4.4.1 Straight Pipe-like Structure (varied W_p)

Figure 4.9(a) shows the singularity-free workspace of the robot within a horizontal straight pipe-like structure. The orientation angle θ of the robot is equal to 90^o with respect to the global reference frame. For simplicity during the discussion of workspace analysis the orientation angle can be redefined with respect to the center-line of the pipe.

Therefore, to this end θ_σ will be used to address the orientation of the robot tangent to the center-line of the pipe as shown in figure 4.8. It can be seen that the workspace region

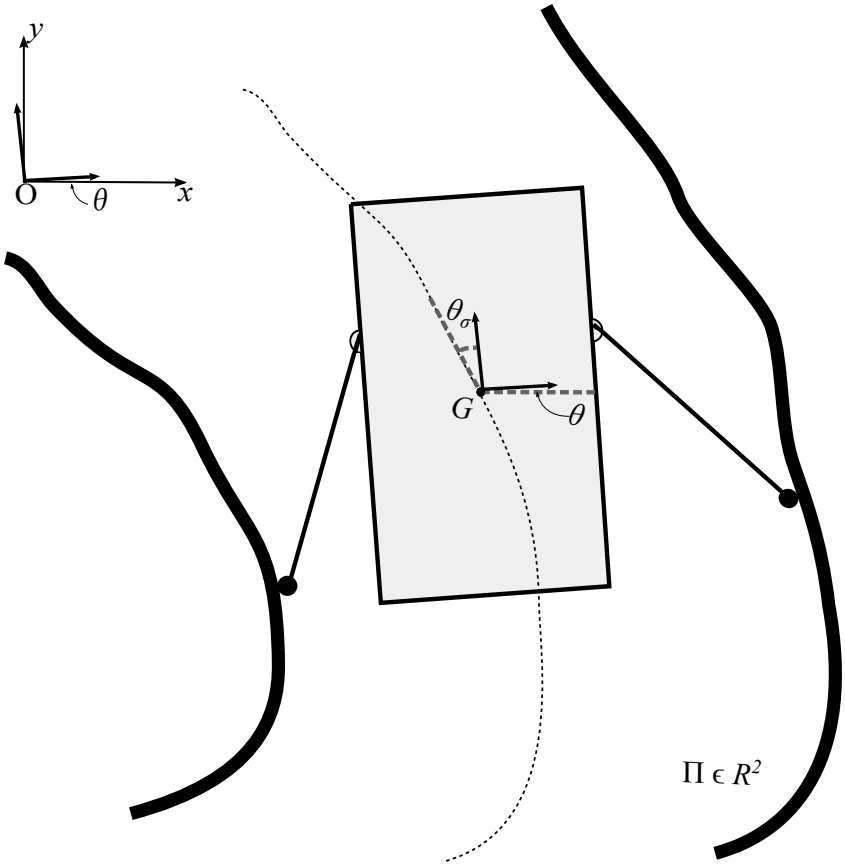

Figure 4.8: Defining the orientation angle (θ_σ) tangent to the center-line of the pipe

in blue is symmetric and resembles the boundary line of the straight pipe. This is one of the advantages of the mobile parallel robot under study, that it is structurally designed to meet the requirements of navigating in confined spaces while tracking the center-line of the pipe. Figures 4.9(b)-4.9(e) show the workspace with the orientation angle of -5^o, 5^o, -15^o, and 15^o about the center line of the pipe, respectively. It can be seen that the singularity-free workspace region (Γ_{sf}) is continuous and it decreases in width along the center line as $\mid \theta_\sigma \mid$ increases. This is due to the fact that the corners of the robot's body tend to collide with the boundaries of the pipe when the angle increases. With the current choice of geometric parameters, the robot's orientation (θ_σ) have a limit of $-17^o < \theta_\sigma < 17^o$, thereafter Γ_{sf} cease to exist due to collisions.

4.4.2 Pipe-like structures: 90^o, 135^o and 180^o elbow

Figures 4.10, 4.11 and 4.12 show the workspace of the robot in 90^o elbow, 135^o elbow and 180^o elbow pipe, respectively. The workspace is evaluated by varying the orientation angle, θ_σ along the center-line of each elbow structure. Therefore, θ_σ is set to 0^o, -10^o, 10^o, -20^o, and 20^o with respect to the center-line of the pipe. It can be seen in figures 4.10, 4.11 and 4.12 that the singularity-free workspace region Γ_{sf} is continuous and it decreases in width along the center line as $\mid \theta_\sigma \mid$ increases. With the current choice of geometric parameters, the robot's orientation have a limit of $-30^o < \theta_\sigma < 30^o$, thereafter the Γ_{sf} region disappears due to the collisions between the robot and the pipe walls. The limit of the orientation angle θ_σ in elbow pipe is twice as large compare to the straight pipe. This is due to the fact that the width W_p of the straight pipe in figure 4.7(a) varies from W_p to $0.75W_p$, which caused the robot to limit its orientation angle to $-17^o < \theta_\sigma < 17^o$ in order to avoid collision.

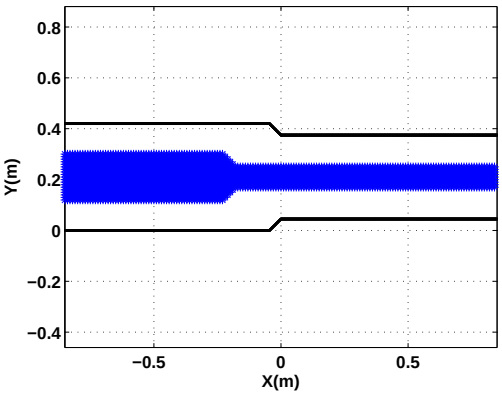

(a) Workspace of mobile parallel robot, $\theta_\sigma = 0^o$

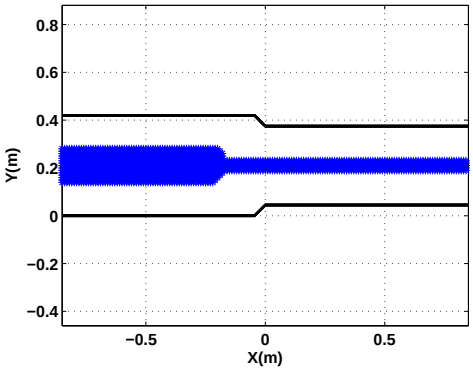

(b) Workspace of mobile parallel robot, $\theta_\sigma = -5^o$

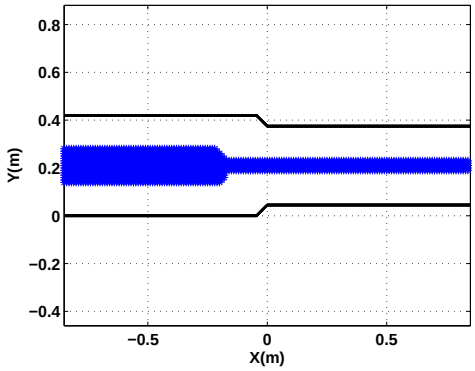

(c) Workspace of mobile parallel robot, $\theta_\sigma = 5^o$

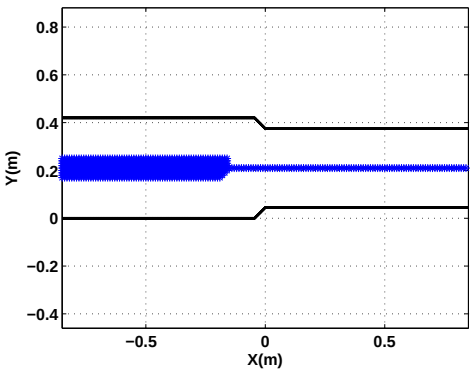

(d) Workspace of mobile parallel robot, $\theta_\sigma = -15^o$

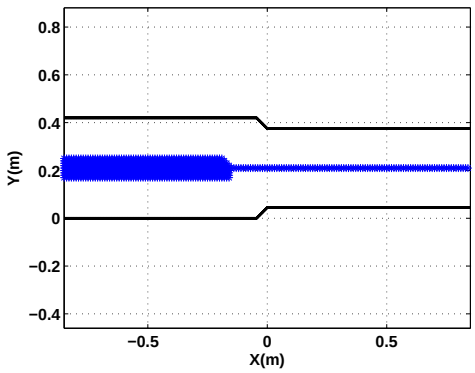

(e) Workspace of mobile parallel robot, $\theta_\sigma = 15^o$

Figure 4.9: Workspace of mobile parallel robot in a Straight pipe-like structure

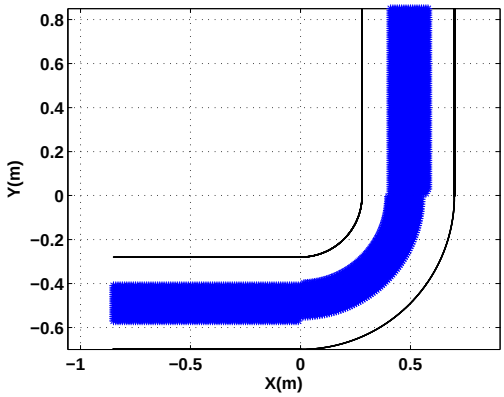

(a) Workspace of mobile parallel robot, $\theta = 0^o$

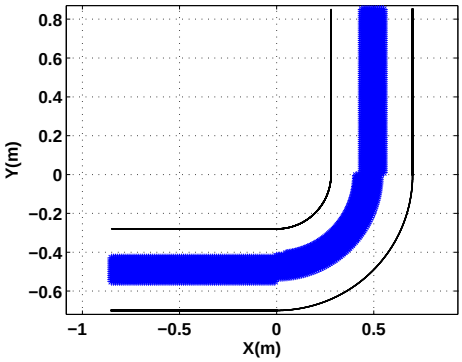

(b) Workspace of mobile parallel robot, $\theta = -10^o$

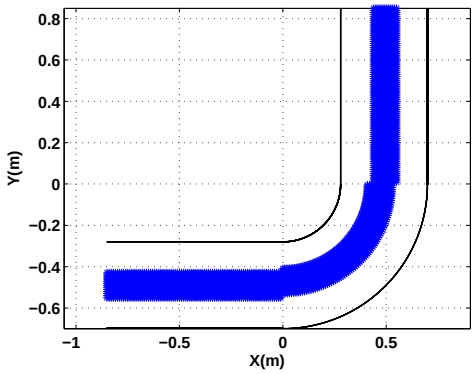

(c) Workspace of mobile parallel robot, $\theta = 10^o$

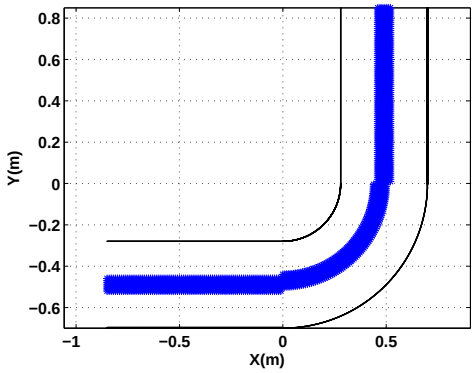

(d) Workspace of mobile parallel robot, $\theta = -20^o$

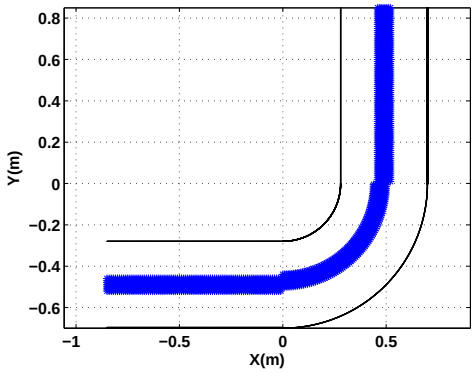

(e) Workspace of mobile parallel robot, $\theta = 20^o$

Figure 4.10: Workspace of mobile parallel robot in 90^o Elbow pipe

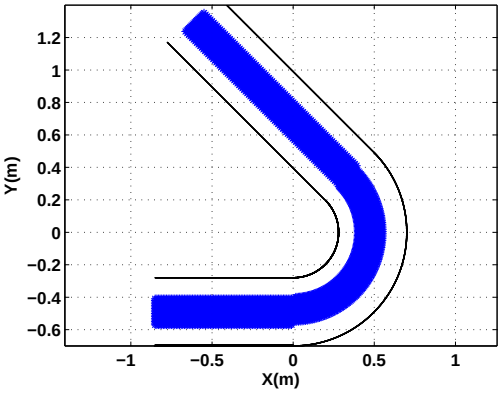

(a) Workspace of mobile parallel robot, $\theta = 0^o$

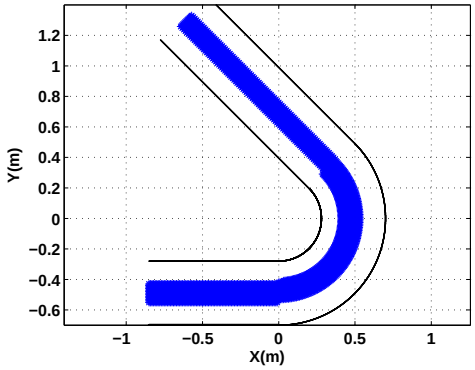

(b) Workspace of mobile parallel robot, $\theta = -10^o$

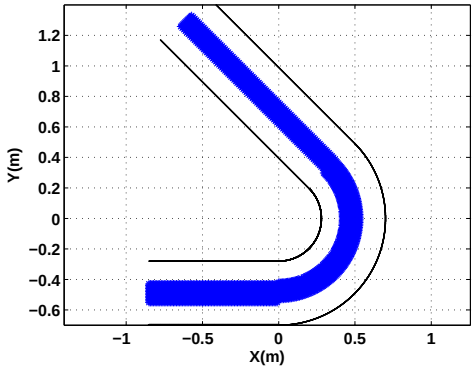

(c) Workspace of mobile parallel robot, $\theta = 10^o$

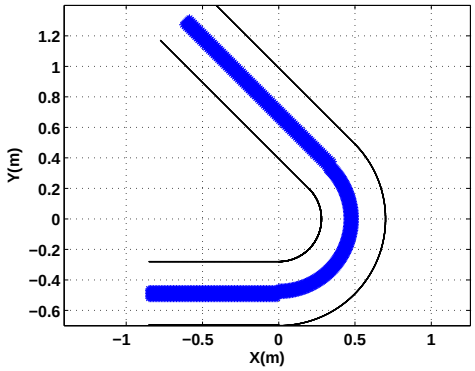

(d) Workspace of mobile parallel robot, $\theta = -20^o$

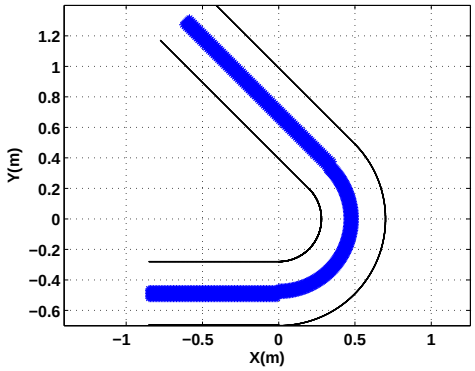

(e) Workspace of mobile parallel robot, $\theta = 20^o$

Figure 4.11: Workspace of mobile parallel robot in 135^o Elbow pipe

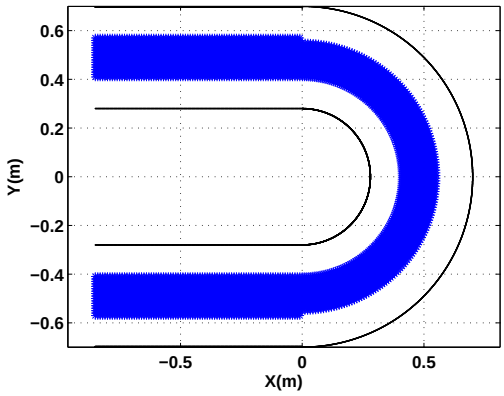

(a) Workspace of mobile parallel robot, $\theta = 0^o$

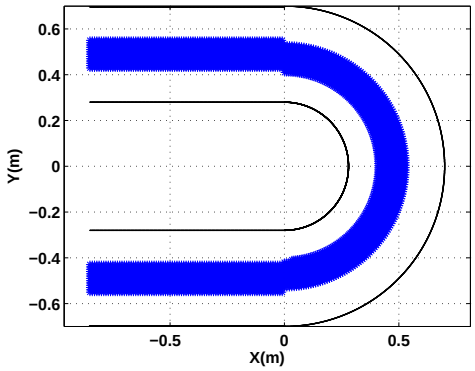

(b) Workspace of mobile parallel robot, $\theta = -10^o$

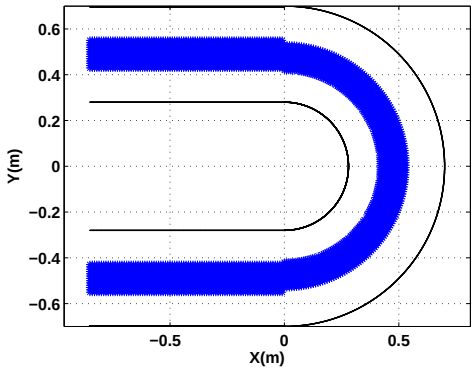

(c) Workspace of mobile parallel robot, $\theta = 10^o$

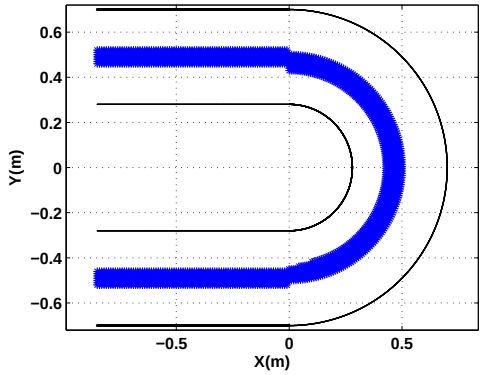

(d) Workspace of mobile parallel robot, $\theta = -20^o$

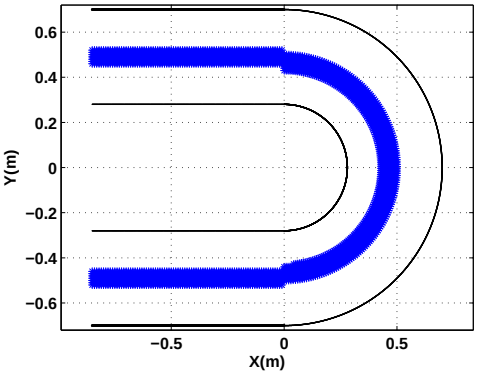

(e) Workspace of mobile parallel robot, $\theta = 20^o$

Figure 4.12: Workspace of mobile parallel robot in 180^o Elbow pipe

4.5 KCI analysis in various pipe-like structures

4.5.1 Straight Pipe-like Structure (varied W_p)

The analysis of proximity to a singular configuration is performed by computing KCI within Γ_{sf} for the orientation angles 0^o, -5^o, 5^o, -15^o, and 15^o. Figure 4.14 shows the variation of KCI on Γ_{sf} region with a color coded map where dark regions are closer to singularity. Figure 4.14(a) shows that the value of KCI is always close to 1 at the center line of the pipe throughout its length. Furthermore, as θ_σ increases, the value of KCI becomes closer to 1 near the center line of the pipe. This is an important observation since it compliments the practical application of a pipeline inspection robot, which often requires its body or robot's center of gravity to be at the center of the pipe width for the optimal functioning of the sensors on board. [67].

4.5.2 Pipe-like structures: 90^o, 135^o and 180^o elbow

Singularity analysis of a mobile parallel robot in 90^o elbow, 135^o elbow and 180^o elbow pipe-like structures are performed within Γ_{sf} for the orientation angles 0^o, -10^o, 10^o, -20^o, and 20^o. The proximity to a singular configuration of the robot is found using kinematic conditioning index, KCI. Figure 4.15 shows the variation of KCI on the Γ_{sf} region in a 90^o elbow pipe with a color-coded map where dark regions are closer to singularity. Similarly figures 4.16 and 4.17, show the results of KCI analysis on 135^o and 180^o elbow pipe structures. Figure 4.15(a) shows the variation of KCI on Γ_{sf} region when the orientation angle is $\theta_\sigma = 0^o$. It is already known from the the analysis of KCI on a straight pipe that the robot is far from a singular configuration when it follows the center-line of the pipe. However, in the curved section of the 90^o elbow pipe, KCI is maximum to the right side of the center-line of the pipe as shown in figure 4.15(a). If the robot navigates into the elbow closely to the left wall, the right arm becomes closer to being normal to the pipe wall leading to a serial singular configuration as depicted in figure 4.4. Similar results are found in 135^o elbow and 180^o elbow when the orientation angle is $\theta_\sigma = 0^o$ as shown in figure 4.16(a) and 4.17(a), respectively.

In an elbow when the robot is orientated with $\theta_\sigma = -10^o, -20^o$ along the center-line, it is far from a singular configuration (or more isotropic) since KCI value of mobile parallel robot reaches 0.7. On the other hand, when the robot is oriented toward the right with $\theta_\sigma = 10^o, 20^o$, the value of KCI is closer to 0.4 along the center-line of the pipe. When the body of the robot is oriented to the right, it is facing opposite to the

path of travel. This causes the angle of the right arm α_2 to increase in order to keep the wheels always in contact with the wall. Moreover the angle of the left arm decreases causing the robot to be far from an isotropic configuration. Figure 4.13 illustrates a configuration of the robot in an elbow while oriented to the right. It can be seen that the right arm increases to $\alpha_2 = 90^o$ as the the robot moves closer to the left wall. This can result in the robot reaching a singular configuration as depicted in figure 4.4.

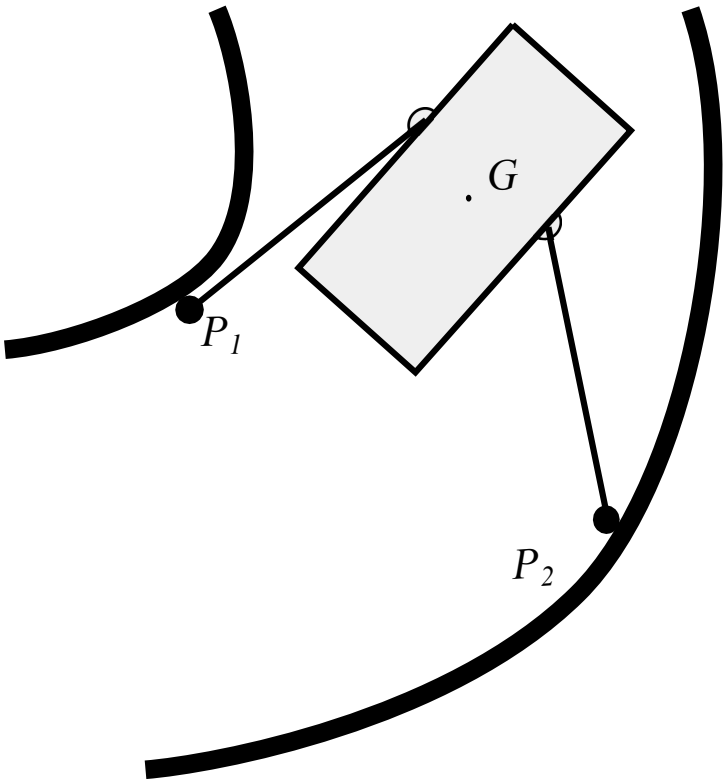

Figure 4.13: Configuration of the robot in an elbow oriented to the right

4.6 Chapter Summary

A discretization method for the workspace analysis is detailed in this chapter. The concept and algorithm of determining singularity-free workspace Γ_{sf} is explained in details. Serial and parallel singularities of the parallel robot are investigated analytically, and all possible singular configurations are identified. Then a method of calculating the proximity to a singular configuration is explained using the Kinematic Conditioning Index, or KCI. For each pipe-like structure introduced in chapter 3, Γ_{sf} and KCI analysis are

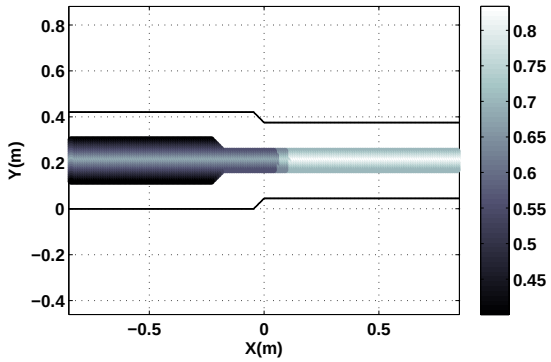

(a) KCI of mobile parallel robot, $\theta_\sigma = 0^o$

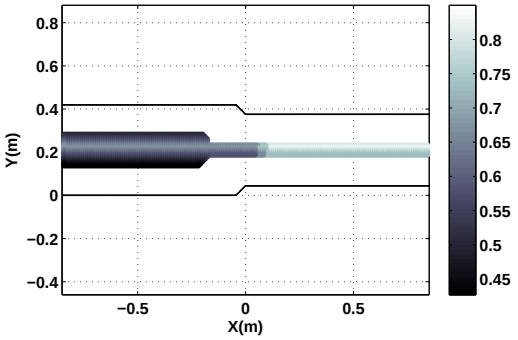

(b) KCI of mobile parallel robot, $\theta_\sigma = -5^o$

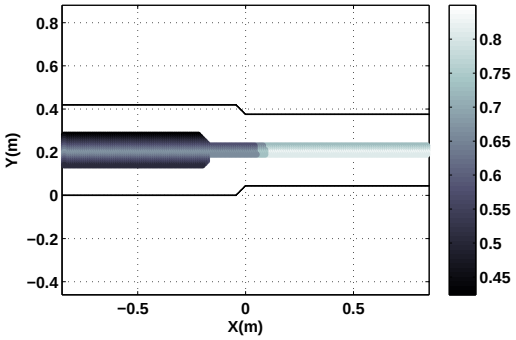

(c) KCI of mobile parallel robot, $\theta_\sigma = 5^o$

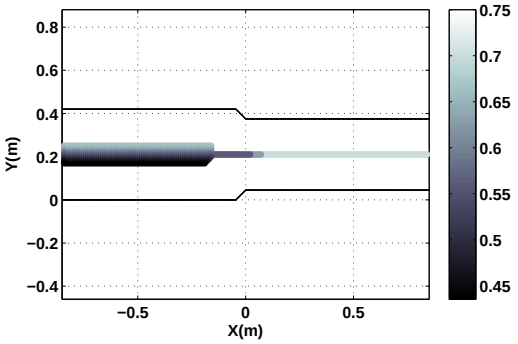

(d) KCI of mobile parallel robot, $\theta_\sigma = -15^o$

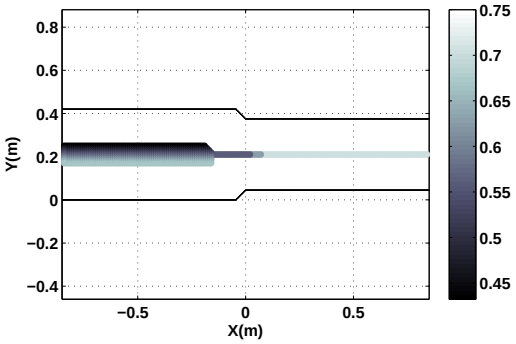

(e) KCI of mobile parallel robot, $\theta_\sigma = 15^o$

Figure 4.14: KCI Analysis of mobile parallel robot in a Straight pipe-like structure

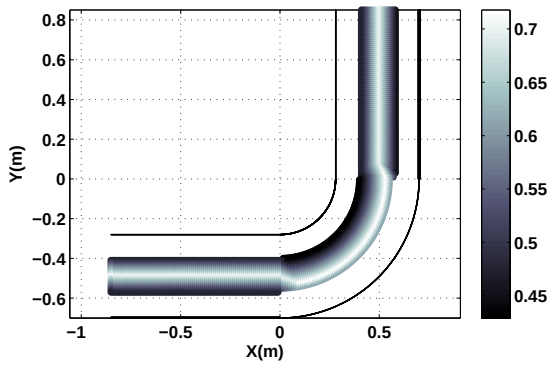

(a) KCI of mobile parallel robot, $\theta = 0^o$

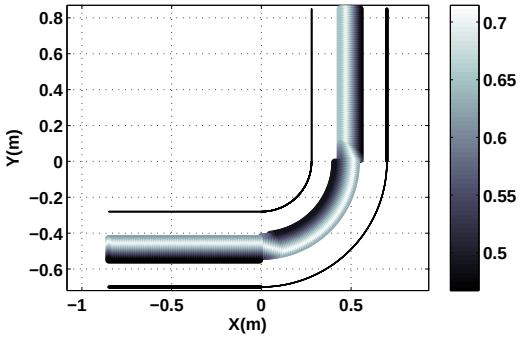

(b) KCI of mobile parallel robot, $\theta = -10^o$

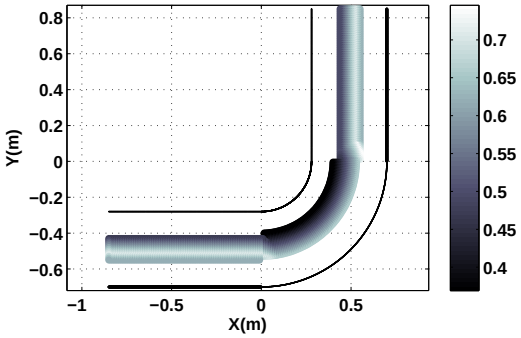

(c) KCI of mobile parallel robot, $\theta = 10^o$

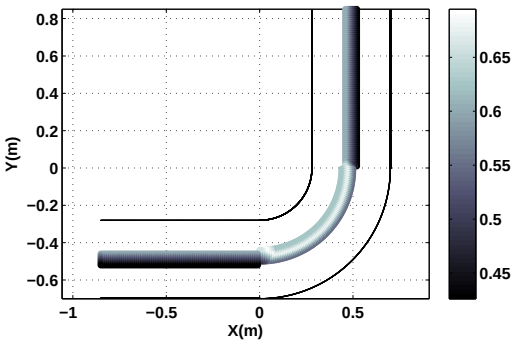

(d) KCI of mobile parallel robot, $\theta = -20^o$

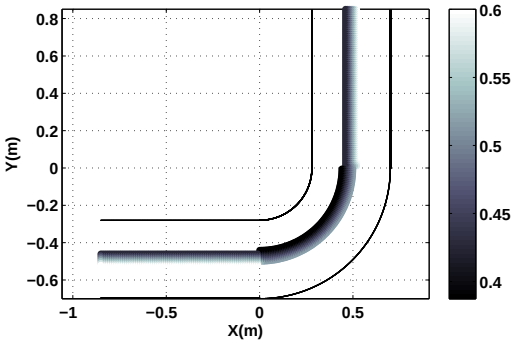

(e) KCI of mobile parallel robot, $\theta = 20^o$

Figure 4.15: KCI Analysis of mobile parallel robot in 90^o Elbow pipe

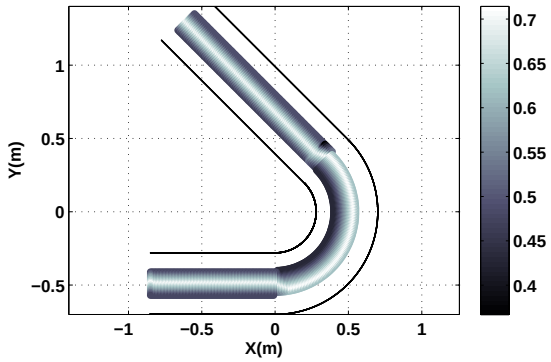

(a) KCI of mobile parallel robot, $\theta = 0^o$

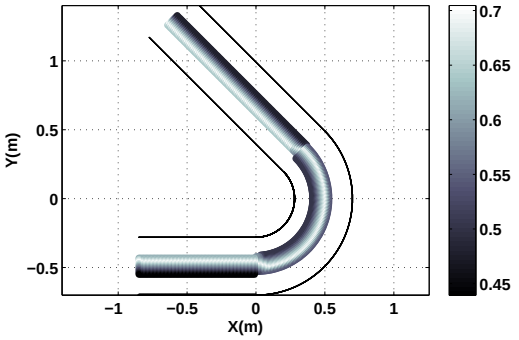

(b) KCI of mobile parallel robot, $\theta = -10^o$

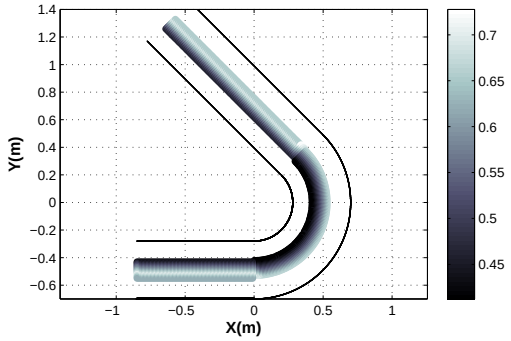

(c) KCI of mobile parallel robot, $\theta = 10^o$

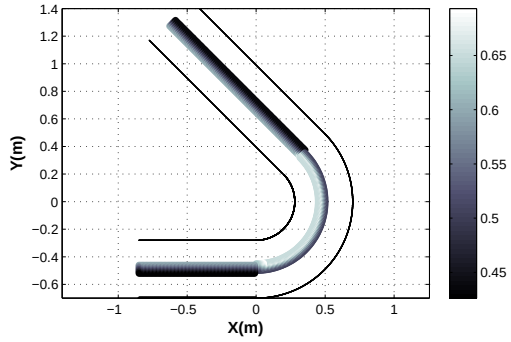

(d) KCI of mobile parallel robot, $\theta = -20^o$

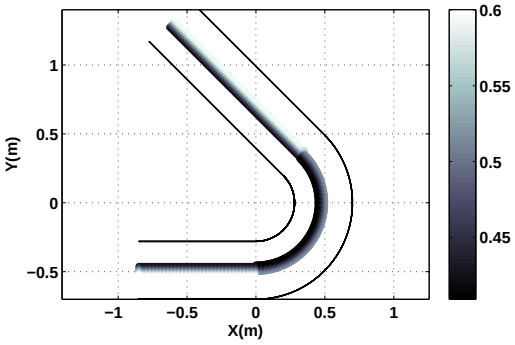

(e) KCI of mobile parallel robot, $\theta = 20^o$

Figure 4.16: KCI Analysis of mobile parallel robot in 135^o Elbow pipe

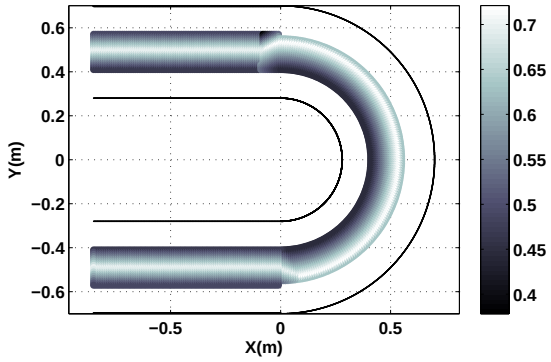

(a) KCI of mobile parallel robot, $\theta = 0^o$

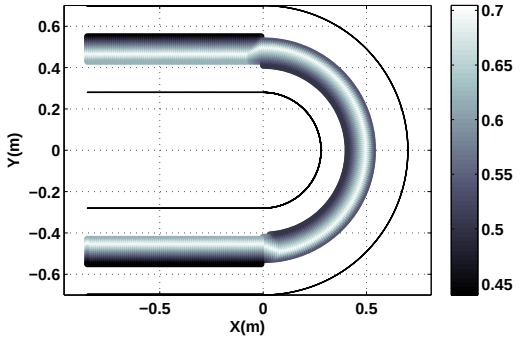

(b) KCI of mobile parallel robot, $\theta = -10^o$

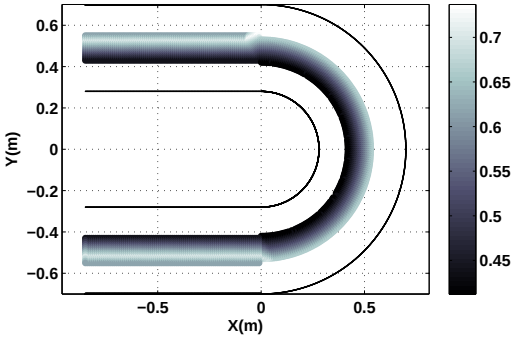

(c) KCI of mobile parallel robot, $\theta = 10^o$

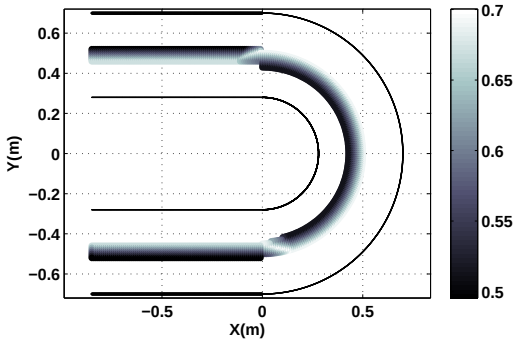

(d) KCI of mobile parallel robot, $\theta = -20^o$

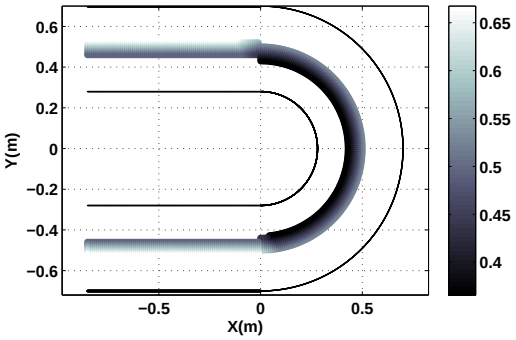

(e) KCI of mobile parallel robot, $\theta = 20^o$

Figure 4.17: KCI Analysis of mobile parallel robot in 180^o Elbow pipe

performed. After obtaining Γ_{sf} in all four types of pipe-like structures, it was evident that the structure of the robot allowed it to have continuity in its singularity-free path. It was also noted that as the θ_σ diverts from zero, the width of Γ_{sf} decreases. The results from this chapter help better understand the kinematic design of the robot as well as its behaviour in various pipe-like structures. The singularity-free workspace obtained in various pipe-structures can assist the mobile parallel robot in its path-planning strategy. The method of determining Γ_{sf} and the results from the analysis will aid in the design optimization of the mobile parallel robot.

Chapter 5

Optimization of Geometric Parameters

5.1 Introduction

The determination of the dimensions of a given structure to achieve a desired kinematic performance is known as Dimensional Synthesis or Design Optimization. It is mentioned by J.P. Merlet, that "a parallel robot with well-designed dimensions will exhibit overall better performance compared to another parallel robot whose structure seems to be more appropriate but whose dimensions have been poorly chosen"[53]. This chapter examines the geometrical characteristics of the planar mobile parallel robot in a confined environment. The confined environment is chosen to be the pipe-like structures introduced in chapter 3. Therefore, the dimensional synthesis on the mobile parallel robot is performed to satisfy multiple performance criteria in these pipe-like structures.

Section 5.2 defines the purpose of optimization and the performance criteria used. Section 5.3 formulates the optimization problem by defining the design variable, constraints and objective function. The technique used to optimize the formulated objective function is described in section 5.4. Section 5.5 to 5.8 provide the results and detailed discussion on the design optimization in four types of pipe-like structures.

5.2 Purpose of Optimization

The mobile parallel robot studied here is the model of a pipeline inspection robot. A pipeline inspection robot is used in energy industry to perform various maintenance operations on pipeline. It is very important to regularly inspect these pipelines as they are used to transport large quantities of natural gas and petroleum products. These robots gather various forms of data while navigating into these pipeline. The data is then used by pipeline operators to make sure that the pipeline is defect-free. The pipeline inspection robot navigates inside pipes with different diameters and elbow joints. Since the diameter of a pipeline vary according to the product being delivered, results presented here are parametrized with respect to the pipe diameter W_p. The purpose of design optimization is to find optimal design parameters that maximize the reachable workspace and minimize the kinematic singularities in a pipe-like structure. Reachable workspace here is defined as the set of all possible locations of the operating points of the robot that may be reached with at least one configuration. The kinematic singularities can be minimized by using the KCI.

5.3 Optimization Problem Formulation

The optimization problem is formulated as a constrained optimization problem in terms of the parameters and constraints imposed on the design. These parameters are also known as design variables, which describe the physical structure of the mobile parallel robot. In the following sections the design parameters, cost function, constraints, and optimization problem are defined.

5.3.1 Design Variables

A total of four design parameters representing the geometry of the mobile parallel robot will be optimized. These design parameters described in chapter 3 are the width w and height h of the body, the length of the arms l, and the position of the arms on the body a. Each of these parameters may only be selected from a specific range of possible values. For example the width of the body may not exceed the diameter of the pipe, otherwise the robot will not fit into the pipe. Similarly, the length of the arms should be large enough to successfully position the body into the pipe. Since this is formulated as a discrete optimization problem each parameter is assigned its own range of values which

are discretely defined. The four design parameters are collected into the vector.

$$\chi = (l,\ w,\ h,\ a\ )$$

where

$$l \in d_l,\ w \in d_w,\ h \in d_h,\ a \in d_a$$

where d_l, d_w, d_h, and d_a are the ranges that define the constraints.

5.3.2 Cost Function

A multi-objective function is considered with additive contributions from workspace and singularity analysis performed in chapter 4. A ratio of Γ_{sf} over Γ_{ref} is used as an index to maximize the reachable workspace and eliminate the singularities within this workspace. As detailed in chapter 4, Γ_{sf} denotes a singularity-free workspace of a mobile parallel robot with respect to a prescribed reference workspace denoted by Γ_{ref}. The optimization problem is formulated as

$$\max_{\chi} \mathbf{F}(\chi) = \max_{\chi} \frac{\Gamma_{sf}}{\Gamma_{ref}}$$

The cost function depends on the design parameters χ. The determination of Γ_{sf} is evaluated using a discretization method for a given χ. The discretization method grids the region into nodes. Each node represents a square with its length equal to the sampling step $0.03W_p$. The cost function, being a ratio of areas, can therefore be expressed equivalently as the ratio of the number of nodes used to discretize the two regions, since each node is surrounded by a square of constant area. Therefore, it may attain any value between 0 and 1, representing the area of the singularity-free workspace relative to the prescribed reference workspace. The goal of the optimization is to find χ which maximizes the cost function $\mathbf{F}$, therefore making Γ_{sf} approximately equal to Γ_{ref}.

5.3.3 Constraints

For the optimization problem three types of constraints are considered. The first type is a singularity-free constraint expressed as a lower bound on KCI.

$$KCI(\chi) > 0.01$$

where $KCI(\chi)$ represents the value of Kinematic Conditioning Index for a given set of design parameters, see 4.3.3.

The second type is a collision avoidance constraint between the arms or body of the robot and the inner boundaries of the pipe structure. The collision avoidance constraint is also part of the Singularity-free workspace determination algorithm, as introduced in chapter 4. The collision avoidance constraint evaluates the position of the robot, which is a function of the set of design parameters χ, the configuration and the orientation. This constraint is set in terms of the boundaries of a confined environment which is defined by two curves parametrized by arc lengths s_1 and s_2 as illustrated in figure 3.1. The robot is required to be between these curves and the configuration of the robot must be collision-free.

The third type is a contact constraint which is required for consistent locomotion of the robot. Specifically, the position of the left and right wheels of the robot defined by point P_1 and P_2 on the walls, respectively, should always lie on the boundaries of the confined environment as illustrated in figure 3.1. Moreover, for an arbitrary value of the design parameter a and h, the relationship between design parameters l and w plays an important role to satisfy the closure equation (3.2) of the robot. Figure 5.1, illustrates the relationship between parameter l and w. It can be seen that as w decreases, the range of values which l may acquire increases accordingly. This phenomenon is taken into consideration in the optimization algorithm, where the range d_l and d_w is adjusted to satisfy this constraint.

The continuity of the workspace is an essential part of the multi objective discrete optimization problem. In this case, a method known as Connected Component Labelling is used to determine if a single geometrical shape exists, representing a continuous workspace throughout the pipe length. Connected Component Labelling is mainly used in computer vision on a binary digital image to detect connected nodes or pixels [29]. The continuity of the workspace is added as an additional constraint in the optimization algorithm to determine the Γ_{sf} region. Figure 5.2 illustrates an example of a discontinuous Γ_{sf} region in grey. A simple iterative process is used to assign the value 1 to nodes representing Γ_{sf}, hence forming a binary digital image. The shaded area representing Γ_{sf} is composed of two disjoint regions. The nodes are connected by either their edges and/or vertices making an 8 way connection.

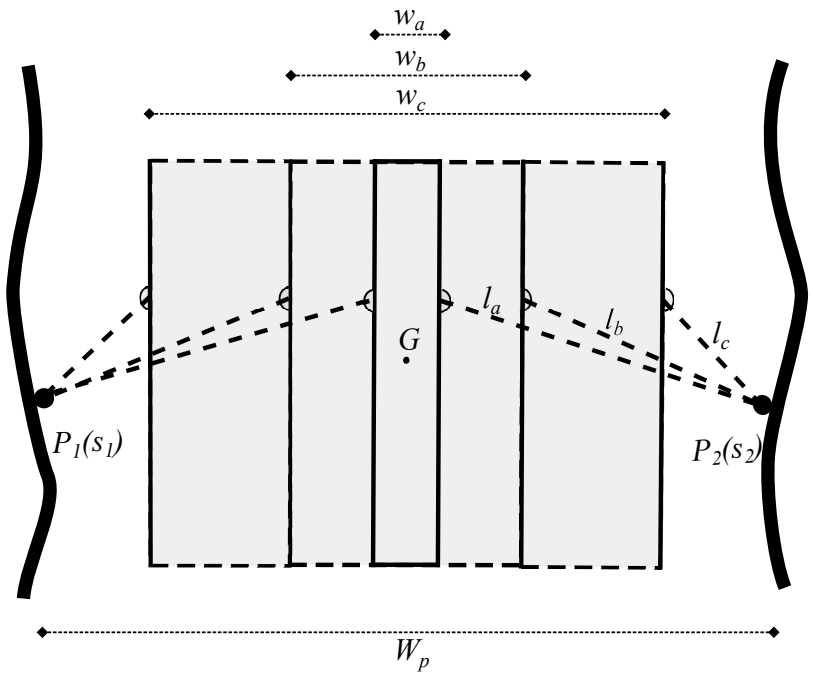

Figure 5.1: Relation between l and w

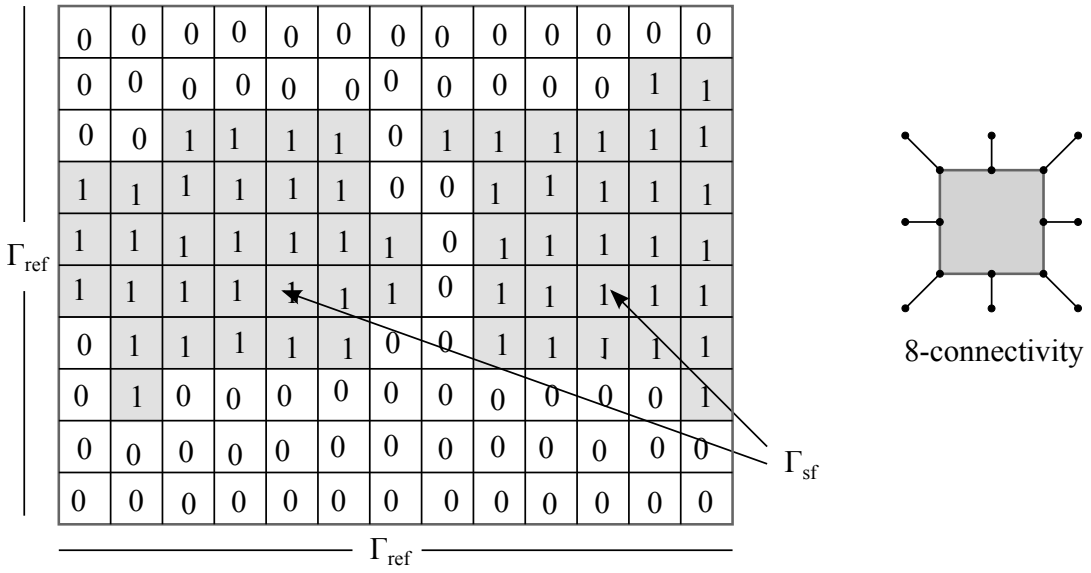

Figure 5.2: Representing a geometric shape using Connected Component Labelling

5.3.4 Constrained Optimization Problem

Based on the discussion above, the constrained optimization problem to find the optimal set of design parameters χ is formulated as

$$\begin{aligned} &\text{Maximize} && \mathbf{F}(\chi) = \frac{\Gamma_{sf}}{\Gamma_{ref}},\ \chi = (l,\ w,\ h,\ a\ ) \\ &\text{subjected to:} && KCI > 0.01 \\ & && \text{Collision Avoidance Constraint} \\ & && 2l + w > W_p \\ & && \text{Continuity of } \Gamma_{sf} \end{aligned}$$

The design parameters are normalized with respect to the width of the pipe, W_p. Moreover, each design parameter attains discrete values between 0 and 1, which can be selected during the execution of the optimization algorithm.

$$\begin{aligned} l \in &\{d_l = (0, 0.01, 0.02, \cdots, 1)\} \\ w \in &\{d_w = (0, 0.01, 0.02, \cdots, 1)\} \\ h \in &\{d_h = (0, 0.01, 0.02, \cdots, 1)\} \\ a \in &\{d_a = (0, 0.01, 0.02, \cdots, 1)\} \end{aligned}$$

The objective function may attain any value between 0 and 1. A value of 0 means Γ_{sf} region does not exist and as the value approaches 1, Γ_{sf} region is maximum.

5.4 Optimization Technique

The optimization technique used to maximize the cost function is known as Parametric Variation method. As discussed in the literature review, this method was used by Huang [35] to optimize the design parameters of a 5DOF planar parallel manipulator. Parametric Variation is composed of a numerical method, used for searching the roots of a non-linear equation, known as Successive Substitution method [33]. Figure 5.3 is a flowchart illustrating the design optimization using Parametric Variation method. The algorithm starts with an initial guess for χ. The initial values are set to $l = 0.5W_p$, $w = 0.5W_p$, $h = W_p$ and $a = 0.5W_p$, so that constraints are not violated. Therefore

$$\begin{aligned} \chi_{[0]} &= \left(l_{[0]}, w_{[0]}, h_{[0]}, a_{[0]}\right) \\ &= (0.5, 0.5, 1, 0.5) \end{aligned}$$

The algorithm discretizes the pipe-like structure forming a grid of nodes to obtain a discrete Γ_{ref} region in which the robot's design parameters are optimized. The sampling step used to discretize the pipe is $0.03W_p$. A step by step procedure of the optimization algorithm is listed below.

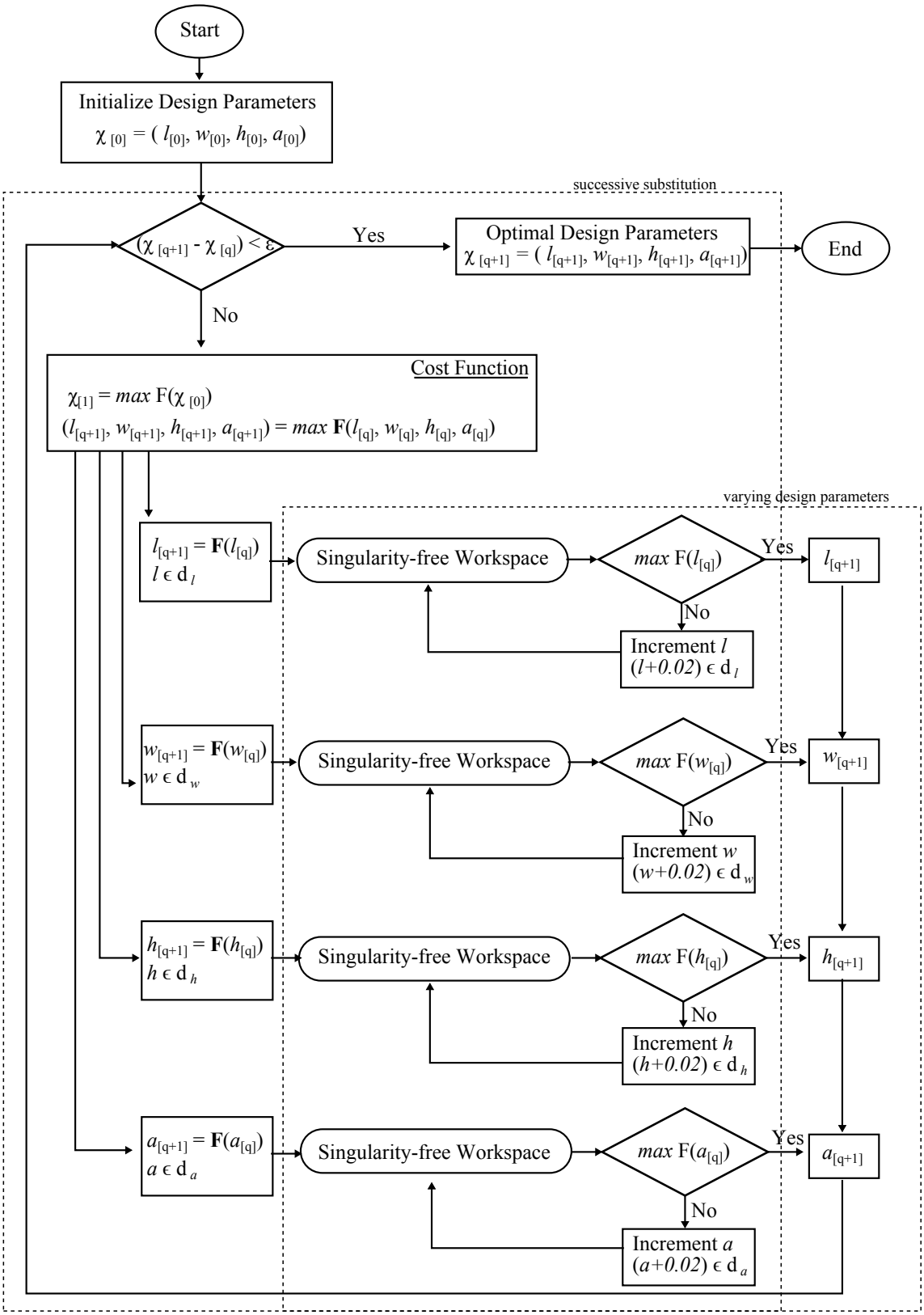

Figure 5.3: Flowchart of a Parametric Variation design optimization

1. The design parameters are initialized

2. The cost function $\mathbf{F}$ is evaluated at $\chi_{[0]}$, and the maximum of $\mathbf{F}$ is found by varying each design parameter while keeping the other parameters fixed:

$$l_{[1]} = \max_{l \in d_l} \mathbf{F}(l, w_{[0]}, h_{[0]}, a_{[0]})$$

$$w_{[1]} = \max_{w \in d_w} \mathbf{F}(l_{[0]}, w, h_{[0]}, a_{[0]})$$

$$h_{[1]} = \max_{h \in d_h} \mathbf{F}(l_{[0]}, w_{[0]}, h, a_{[0]})$$

$$a_{[1]} = \max_{a \in d_a} \mathbf{F}(l_{[0]}, w_{[0]}, h_{[0]}, a)$$

   Hence the first set of optimized parameters denoted by $\chi_{[1]}$ is obtained.

3. $\mathbf{F}$ is evaluated at $\chi_{[1]}$. As before the maximum of $\mathbf{F}$ is found by varying each design parameter while keeping the other parameters fixed:

$$l_{[2]} = \max_{l \in d_l} \mathbf{F}(l, w_{[1]}, h_{[1]}, a_{[1]})$$

$$w_{[2]} = \max_{w \in d_w} \mathbf{F}(l_{[1]}, w, h_{[1]}, a_{[1]})$$

$$h_{[2]} = \max_{h \in d_h} \mathbf{F}(l_{[1]}, w_{[1]}, h, a_{[1]})$$

$$a_{[2]} = \max_{a \in d_a} \mathbf{F}(l_{[1]}, w_{[1]}, h_{[1]}, a)$$

4. The above process is repeated for q iterations until the set of parameters convergences. This means that the change between $\chi_{[q+1]}$ and $\chi_{[q]}$ is within a specified tolerance, denoted here by $\epsilon = 0.01$:

$$|| \chi_{[q+1]} - \chi_{[q]} || \leq \epsilon$$

5. $\chi_{[q]} = (l_{[q]}, w_{[q]}, h_{[q]}, a_{[q]})$ is considered the optimal solution.

During the optimization, a sampling step of 0.02 is used to vary each design parameter. The sampling step governs the convergence and accuracy of the solution. Therefore three different sampling steps are used to test the accuracy of the results. Figure 5.4 shows the plot of average cost function versus l used to find the converged value of l during the constraint optimization in a straight pipe. In figure 5.5, three different sampling steps are used for the same procedure. The dashed black line represents the variation of l with step size of 0.1. The dotted black line is obtained with step size 0.04, and the blue line is

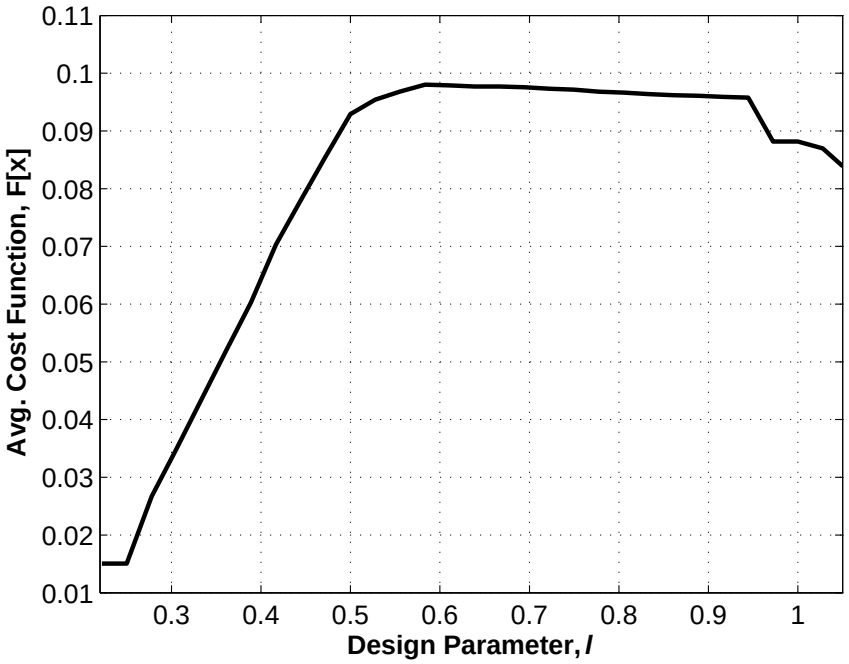

Figure 5.4: Average Cost Function versus l, for $w = 0.5W_p$, $h = W_p$ and $a = 0.96$

obtained with step size 0.02. It can be seen that as the step size decreases from 0.1 to 0.02, the plot tend to overlap. Further reducing the step size increases the computational time with no significant gain. Therefore, a step size of 0.02 is used to vary the design parameters during the design optimization.

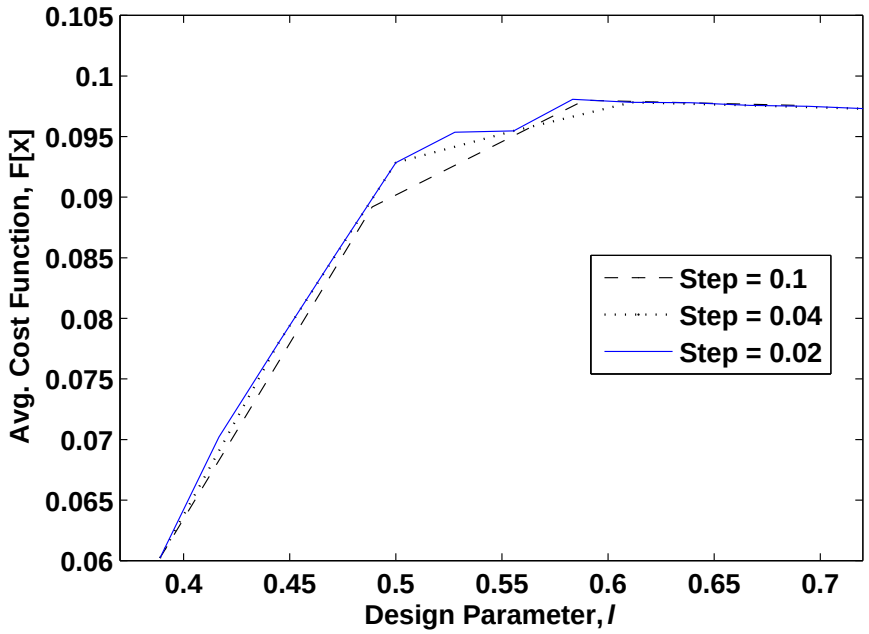

Figure 5.5: Average Cost Function versus l using three different sampling steps

5.5 Optimization in a Straight Pipe

The initial configuration of the robot placed in a straight pipe with varying diameter is shown in Figure 5.6. The design parameters l and a are set equal to half of W_p. The length and width of the body is kept in a rectangular shape with $w = 0.5W_p$ and $h = W_p$. The rectangular shape of the body reflects a possible size of the payload during the design phase of the robot. The four corners and the arms of the robot are highlighted in red to show the possible collision points. Before starting the optimization process, it

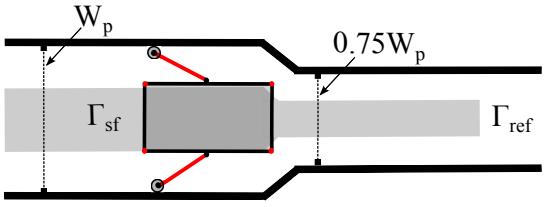

Figure 5.6: Initial configuration of the robot in a horizontal straight pipe with varying width

is worth visualizing Γ_{sf} for the given initial design parameters. The straight pipe-like structure is divided into 6205 nodes to obtain a discrete Γ_{ref} region from which Γ_{sf}

nodes are highlighted for a constant orientation angle $\theta_\sigma = 0°$ with respect to the center line of the pipe. The resultant Γ_{sf} region is shown in Figure 5.7. The total number of nodes composing Γ_{sf} is 2054. Each node represents a square with a length of $0.03W_p$. Therefore, the resulting value of the objective function $\mathbf{F}(\chi)$ when $\theta_\sigma = 0°$ is

$$\mathbf{F}(\ 0.5,\ 0.5,\ 1,\ 0.5\ ) = \frac{\Gamma_{sf}}{\Gamma_{ref}} = \frac{2054}{6205} = 0.331$$

This means that, using the initial parameters the robot is able to reach 33.1% of Γ_{ref} region.

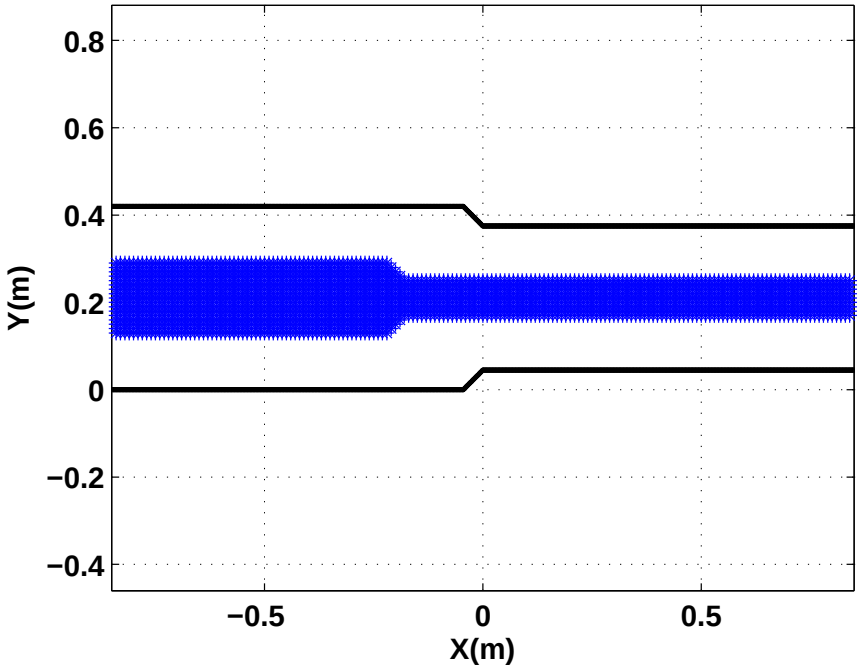

Figure 5.7: Γ_{sf} using initial parameters , $\theta_\sigma = 0°$ in a straight pipe

5.5.1 Constrained Optimization

Certain parameters are required to be constrained due to the fact that the minimum size of the body, described by w and h, is determined by its payload. For example the body of the robot is required to fit various electronics and mechanical components. Therefore, the design parameters w and h are kept constant to obtain a desired dimension and only

l and a are optimized. The constant value of h and w are set as

$$w = 0.5W_p$$

$$h = W_p$$

Table 5.1 shows the values of parameters l and a at various iterations during the optimization process. The converged design parameters are obtained at the 10^{th} iteration, where $l = 0.58W_p$ and $a = 0.96$. The position of the pinning points of the arms (a) which maximize the Γ_{sf} is at the top corners of the body.

Table 5.1: Optimization of constrained design parameters

Design Parameters	l	a
Initial parameter	0.50	0.50
$1^{st} Iteration$	0.47	0.82
$2^{nd} Iteration$	0.45	0.80
$3^{rd} Iteration$	0.50	0.76
$4^{th} Iteration$	0.47	0.85
$5^{th} Iteration$	0.53	0.95
$6^{th} Iteration$	0.58	0.77
$7^{th} Iteration$	0.47	0.96
$8^{th} Iteration$	0.58	0.95
$9^{th} Iteration$	0.58	0.96
Optimal Parameters		
$10^{rd} Iteration$	0.58	0.96

The optimization process is also repeated here and the results of the optimal design parameters are verified by using different initial parameters to show convergence to the same values for different initial conditions. Figure 5.8 shows the configuration of the robot in a straight pipe with a different set of initial parameters. Parameters l and a are set equal to $0.25W_p$. Parameters w and h are set to $w = 0.5W_p$, $h = W_p$. The pipe-like structure is divided into 6205 nodes to obtain a discrete Γ_{ref} region from which Γ_{sf} nodes are highlighted for a constant orientation angle $\theta_\sigma = 0^\circ$ with respect to the center line of the pipe. The resultant Γ_{sf} region is shown in Figure 5.9. Due to short arm lengths, the robot is more likely to violate the contact constraints between the wheels and the pipe walls. Therefore, a narrower Γ_{sf} region exist in pipe width equal to W_p. However,

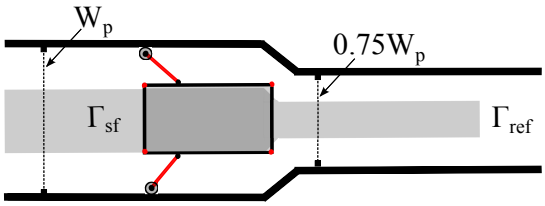

Figure 5.8: Configuration of the robot in a straight pipe with different initial parameters

as the robot moves in to a pipe with $0.75W_p$, the Γ_{sf} region becomes wider. The total number of nodes composing Γ_{sf} is 748. Each node represents a square of length $0.03W_p$. Therefore, the resulting value of the objective function $\mathbf{F}(\chi)$ when $\theta_\sigma = 0°$ is

$$\mathbf{F}(\ 0.25,\ 0.5,\ 1,\ 0.25\ ) = \frac{\Gamma_{sf}}{\Gamma_{ref}} = \frac{748}{6205} = 0.120$$

This means that, using the initial parameters the robot is able to reach only 12.0% of Γ_{ref} region. Table 5.2 shows the values of parameters l and a at various iterations during the

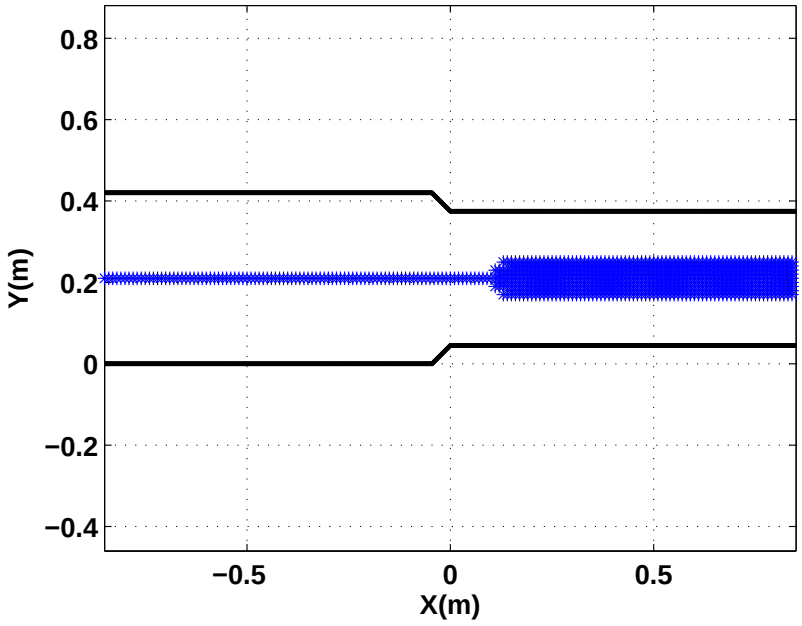

Figure 5.9: Γ_{sf} using different initial parameters, $\theta_\sigma = 0°$ in a straight pipe

optimization process. The converged design parameters are obtained after 9 iterations, where $l = 0.58W_p$ and $a = 0.96$. These optimal values are virtually the same as those obtained with the other set of initial conditions.

Table 5.2: Optimization with different initial parameters

Design Parameters	l	a
Initial parameter	0.25	0.25
$1^{st} Iteration$	0.44	0.82
$2^{nd} Iteration$	0.50	0.75
$3^{th} Iteration$	0.47	0.85
$4^{th} Iteration$	0.53	0.95
$5^{th} Iteration$	0.58	0.77
$6^{th} Iteration$	0.47	0.96
$7^{th} Iteration$	0.58	0.95
$8^{th} Iteration$	0.58	0.96
Optimal Parameters		
$9^{rd} Iteration$	0.58	0.96

Figure 5.10(a) shows values of the cost function versus θ_σ for various values of the parameter l, when $w = 0.5W_p$, $h = W_p$ and $a = 0.96$. It can be seen that when the orientation of the module is close to zero, more than one value of parameter l exist that maximize the cost function. Moreover, the plots represented by $l = 0.58W_p$, $0.72W_p$ and $0.86W_p$ are overlapped around the maximum of $\mathbf{F}$. To solve for this ambiguity, Figure 5.10(b) is used which plots the average of the cost function value with respect to θ_σ versus the design parameter l. Therefore with respect to this measure, it can be seen that the value of l where the cost function is maximum is $l = 0.58W_p$.

Figure 5.11(a) shows values of the cost function versus θ_σ for various values of a, when $l = 0.58W_p$, $w = 0.5W_p$ and $h = W_p$. It can be noted that when the configuration of the robot is symmetric at $\theta_\sigma = 0^\circ$, the plots for different values of a all overlap around the maximum of $\mathbf{F}$. However, as the robot moves away from a symmetric configuration the best value of a is close to 1. Figure 5.11(b) complements the above finding by averaging the cost function value over the range of θ_σ versus the design parameter a. Therefore, it can be confirmed that the best value to choose in order to maximize the singularity-free workspace is approximately $a = 1$.

Figure 5.12 shows a configuration of the robot with the constant parameters $h = W_p$ and $w = 0.5W_p$, and the optimal values for l and a. Figure 5.13 shows the robot with optimal design parameters in a straight pipe. The resultant Γ_{sf} region of these new

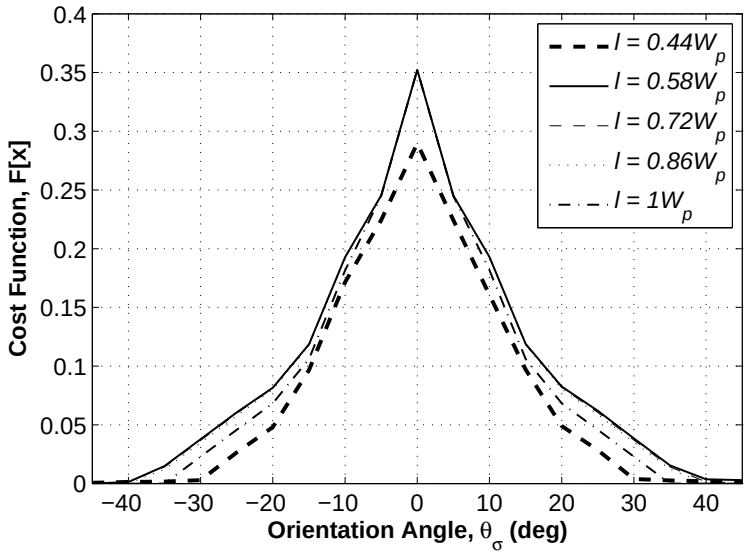

(a)

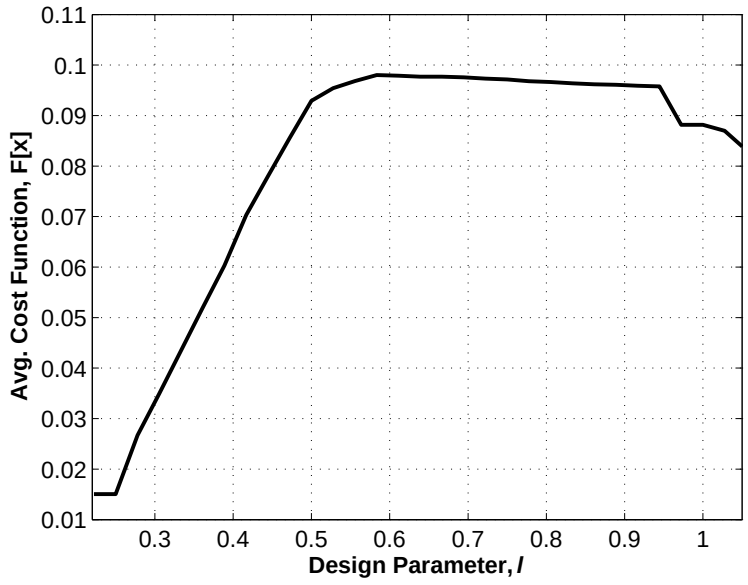

(b)

Figure 5.10: (a)Cost Function versus θ_σ for various values of l (b)Average Cost Function versus l, for $w = 0.5W_p$, $h = W_p$ and $a = 0.96$

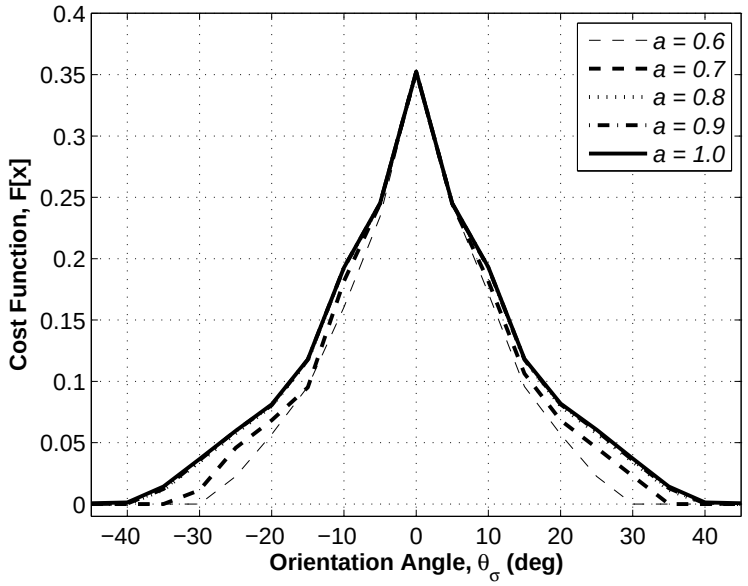

(a)

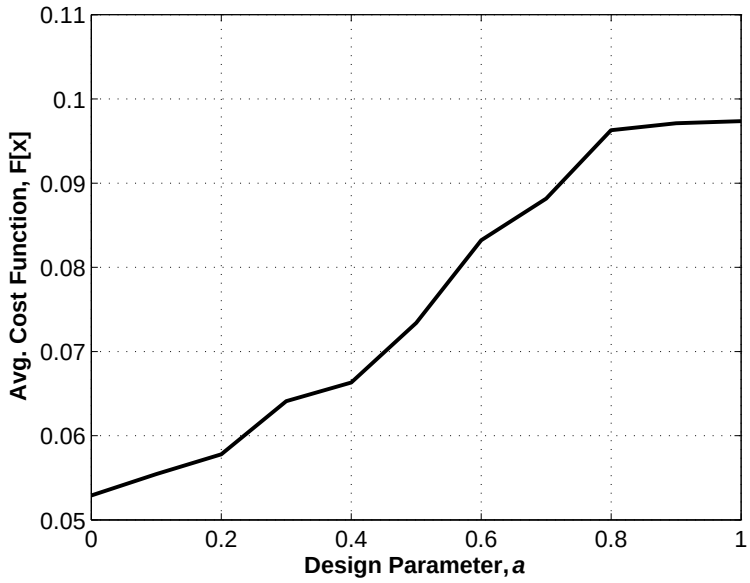

(b)

Figure 5.11: (a)Cost Function versus θ_σ for various values of a (b)Average Cost Function versus a, for $l = 0.58W_p$, $w = 0.5W_p$ and $h = W_p$.

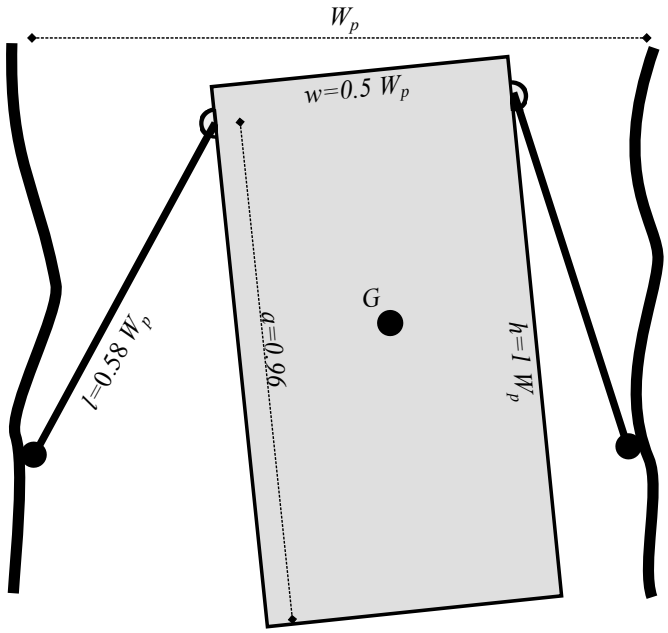

Figure 5.12: Configuration of the robot with optimal values for l and a (with constant h and w values)

parameters is shown in figure 5.14. The total number of discrete points depicting a Γ_{sf} region is 2117 out of 6205 points of Γ_{ref}, when $\theta_\sigma = 0°$.

$$\mathbf{F}(\chi) = \mathbf{F}(\ 0.58,\ 0.50,\ 1.0,\ 0.96\ ) = \frac{\Gamma_{sf}}{\Gamma_{ref}} = \frac{2117}{6205} = 0.341$$

This means that using these optimal design parameters, the robot is able to reach 34.1% of Γ_{ref} region.

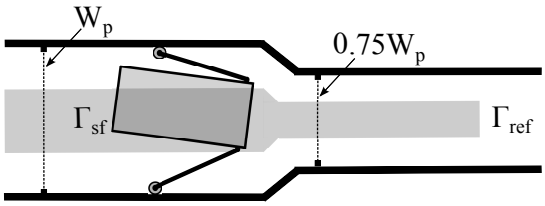

Figure 5.13: Configuration of the robot in a straight pipe using optimal constrained design parameters

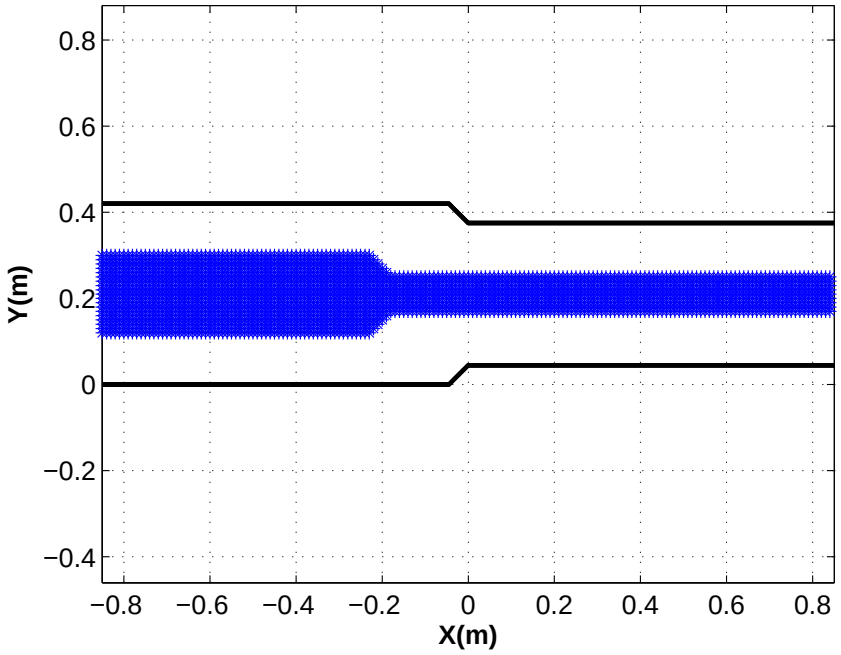

Figure 5.14: Γ_{sf} region using constrained design parameters in a straight pipe, $\theta_\sigma = 0^o$

5.5.2 Optimization with unconstrained design parameters

In this section the optimization is performed without setting any upper or lower bounds on the design parameters with the purpose to investigate the limit cases arising without constraints. Table 5.3 shows the values of each design parameters at various iterations during the optimization process. Converged values of l, w, h and a are found at 8^{th} iteration. Using the converged optimal design parameters, the robot crosses the pipe and satisfy all of its constraints. A representation of these parameters normalized with respect to W_p is presented in figure 5.15, where the mobile parallel robot is shown in an arbitrary confined environment. It can be seen that when the design parameters are unconstrained, the payload area denoted by h and w reaches zero. This causes the two pinning point of the arms to be connected together as a revolute joint.

Figure 5.16(a) shows values of the cost function versus θ_σ for various values of l, when $w = 0$, $h = 0$ and $a = 1$. This plot shows that $\mathbf{F}$ is maximum when θ_σ is close to zero. However, as the orientation angle changes this is not the case. Figure 5.16(b) shows the average of the cost function over the range of θ_σ versus l. It can be seen that when $l = W_p$, the average of the cost function is maximum.

Table 5.3: Optimization of Design Parameters in a Straight Pipe

Design Parameters, χ	l	w	h	a
Initial parameter	0.5	0.5	0.5	0.5
$1^{st} Iteration$	0.44	0.36	0.03	1
$2^{nd} Iteration$	0.64	0.44	0.42	1
$3^{rd} Iteration$	0.58	0.14	0.33	1
$4^{th} Iteration$	0.86	0.22	0.39	1
$5^{th} Iteration$	0.78	0.03	0.16	1
$6^{nd} Iteration$	0.97	0.03	0.03	1
$7^{rd} Iteration$	1	0	0	1
Optimal Parameters				
$8^{rd} Iteration$	1	0	0	1

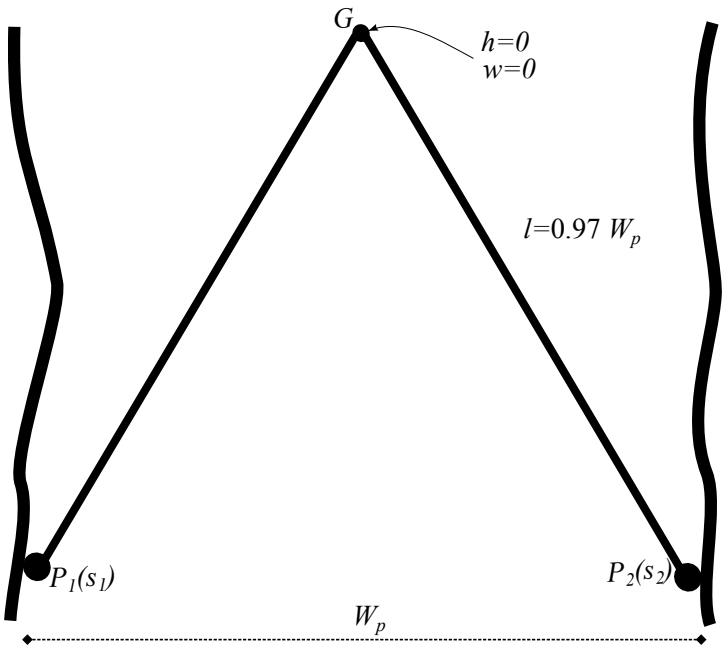

Figure 5.15: Configuration of the robot with converged unconstrained design parameters

Figure 5.17(a) shows values of the cost function versus θ_σ for various values of parameter w, when $l = W_p$, $h = 0$ and $a = 1$. When $w = 0$, Γ_{sf} is maximum with a value of 0.83, which means that 83% of the Γ_{ref} in a straight pipe is reachable by the end-effector G of the robot. Moreover, in general the cost function value is also maximum

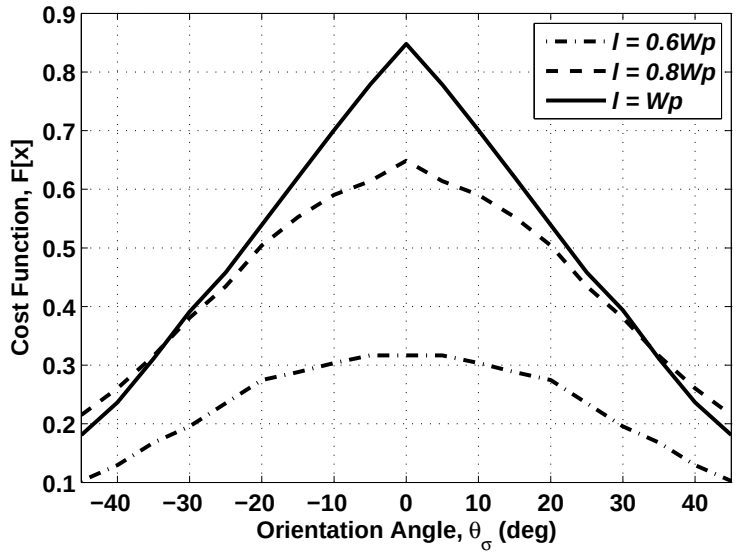

(a)

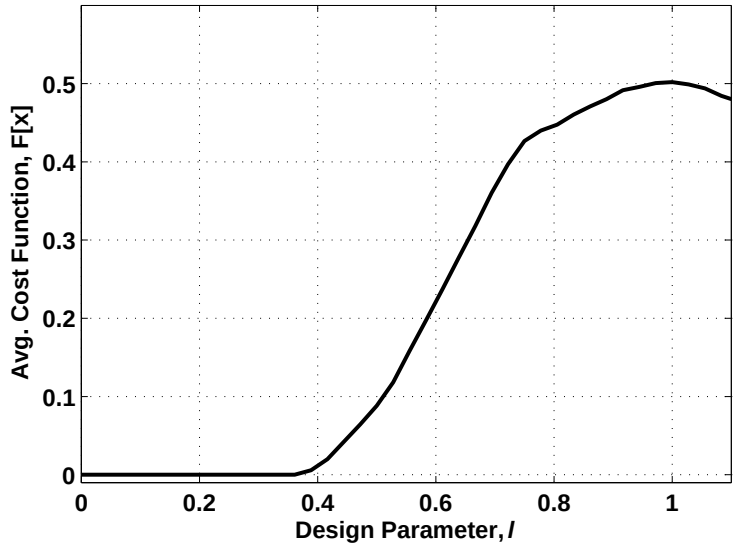

(b)

Figure 5.16: (a) Cost Function versus θ_σ for various values of l (b) Average Cost Function versus l, for $w = 0$, $h = 0$ and $a = 1$

when $-45^\circ \leq \theta_\sigma \leq 45^\circ$. Figure 5.17(b) confirms the above finding by averaging the cost function value over the range of θ_σ versus the design parameter w. Therefore, it can be seen that the value of w which maximizes the cost function is $w = 0$.

Figure 5.18(a) shows values of the cost function versus θ_σ for various values of the parameter h, when $l = W_p$, $w = 0$ and $a = 1$. It can be noted that for different values of h presented in figure 5.18(a) the cost function value versus θ_σ almost stays the same. The reason behind this is because the width of the module is $w = 0$ and as the value of h decrease, the module of the robot is less likely to collide with the inner walls of the straight pipe. Similar to the design parameter w, the value $h = 0$ is found since the cost function value is always maximum when θ_σ changes from -45° to 45° degrees. Figure 5.18(b) complements the above finding by averaging the cost function value over the range of θ_σ versus the design parameter h. Therefore, it can be confirmed that the value of $h = 0$ maximizes the cost function.

Figure 5.19(a) shows values of the cost function versus θ_σ for various values of the parameter a, when $l = W_p$, $w = 0$ and $h = 0$. It can be noted that for various values of a presented in figure 5.19(a) the cost function value versus θ_σ stays the same and the plots are overlapped. In order to understand this result, it is important to recall that a represents the position of the arm joints on the body of the robot. Since the converged value of w and h are equal to zero, the value of $\mathbf{F}$ stays constant as a is varied. Therefore, in this case a does not effect the cost function. Figure 5.19(b) shows the average of the cost function value over the range of θ_σ versus the design parameter a. It can be seen that the value of the cost function is constant as a is varied. For the purpose of selecting a value of a to continue the optimization process, $a = 1$ is selected.

Figure 5.20 represents the robot with converged unconstrained design parameters in a straight pipe. Figure 5.21 shows Γ_{sf} region of the robot when $\theta_\sigma = 0^\circ$. It can be seen that the width of Γ_{sf} decreases as the width of the pipe reduces to $0.75W_p$. This is due to the fact that the arms of the robot adapts to the pipe to avoid colliding with the inner boundaries. The total number of discrete points representing Γ_{sf} region is 5258 out of 6205 points for Γ_{ref} region when $\theta_\sigma = 0^\circ$.

$$\mathbf{F}(\chi) = \mathbf{F}(\ 1.0,\ 0.0,\ 0.0,\ 1.0\ ) = \frac{\Gamma_{sf}}{\Gamma_{ref}} = \frac{5258}{6205} = 0.847$$

This means that, using the unconstrained optimal parameters the robot is able to reach approximately 85% of Γ_{ref} region.

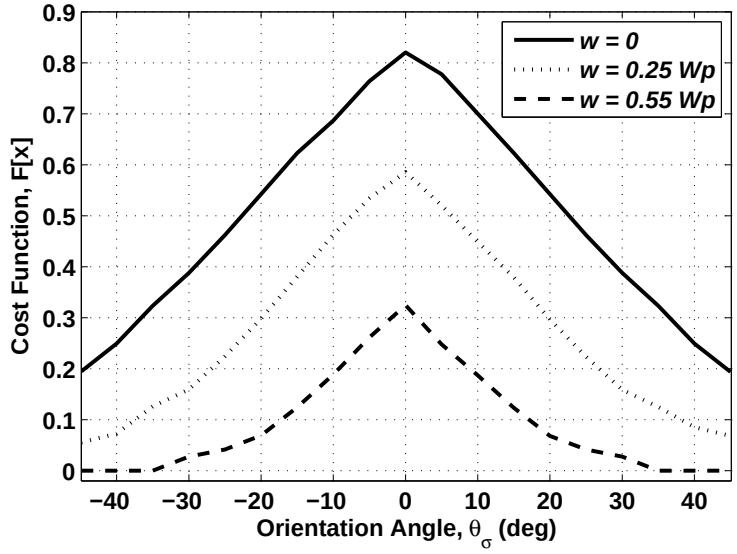

(a)

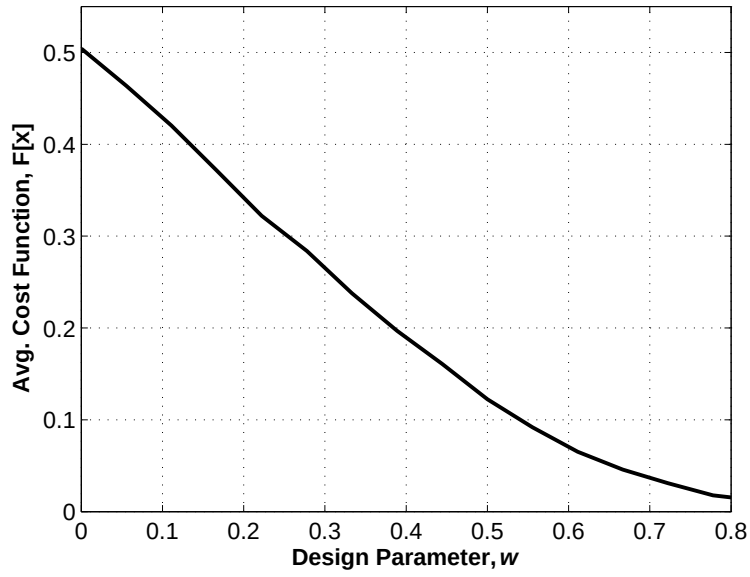

(b)

Figure 5.17: (a)Cost Function versus θ_σ for various values of w (b) Average Cost Function versus w, for $l = W_p$, $h = 0$ and $a = 1$.

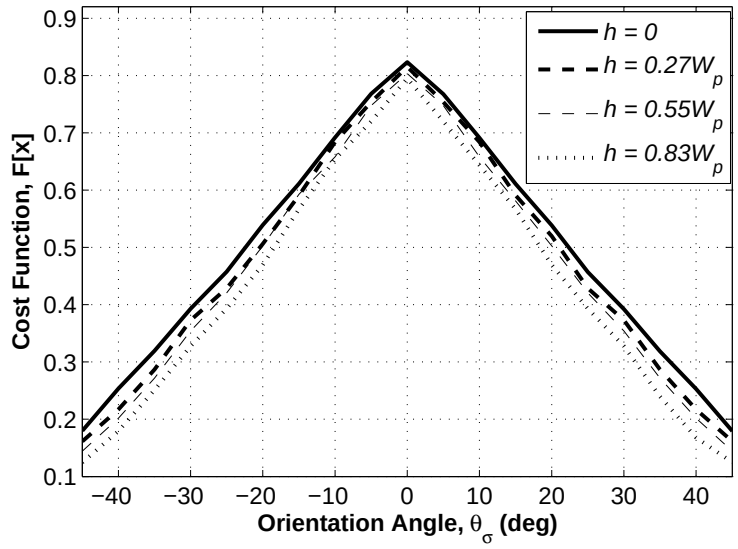

(a)

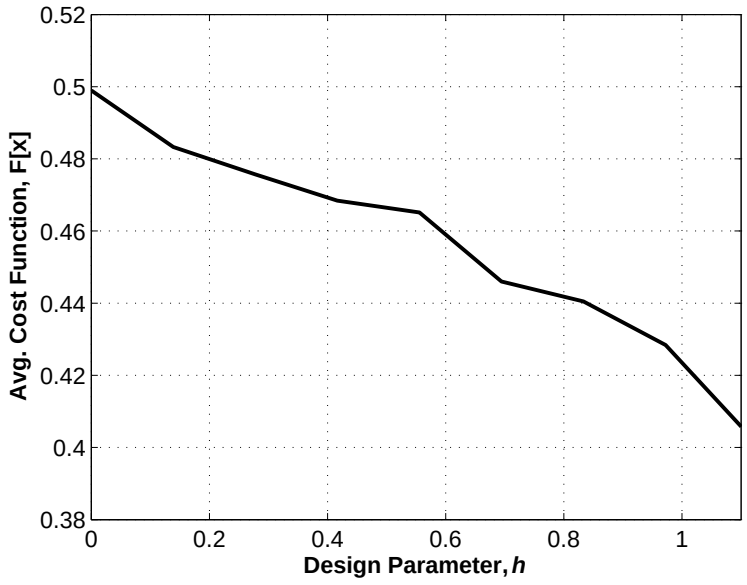

(b)

Figure 5.18: (a)Cost Function versus θ_σ for various values of h (b)Average Cost Function versus h, for $l = W_p$, $w = 0$ and $a = 1$.

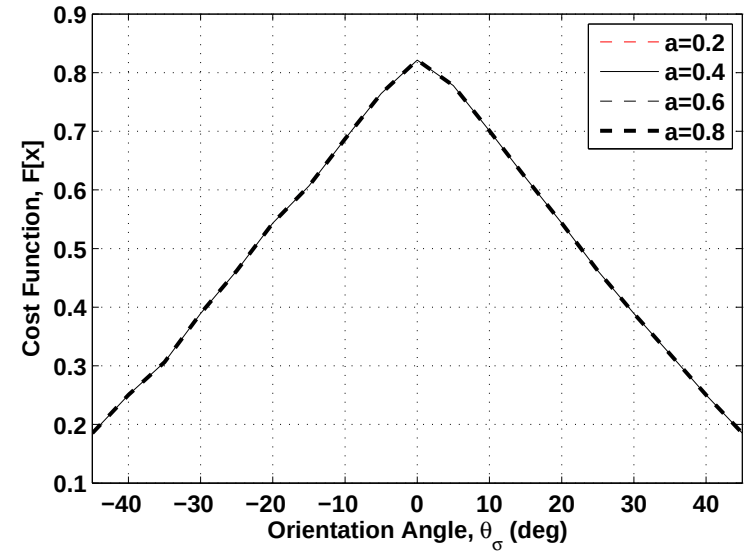

(a)

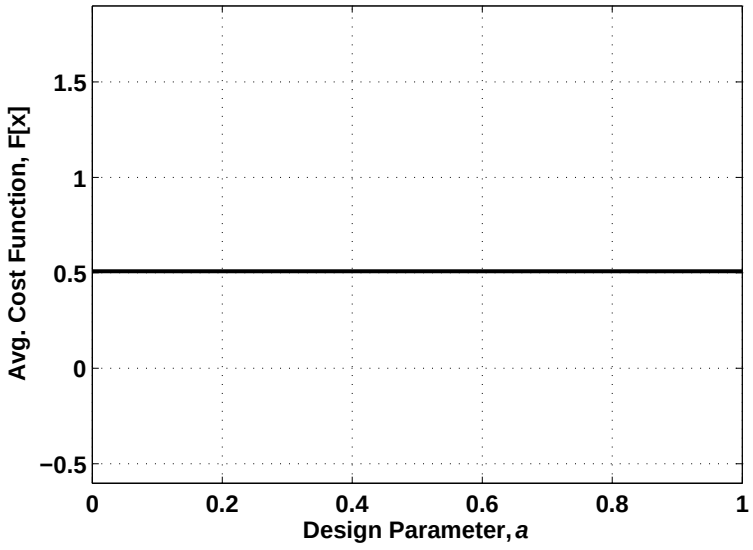

(b)

Figure 5.19: (a)Cost Function versus θ_σ for various values of a (b)Average Cost Function versus a, for $l = W_p$, $w = 0$ and $h = 0$.

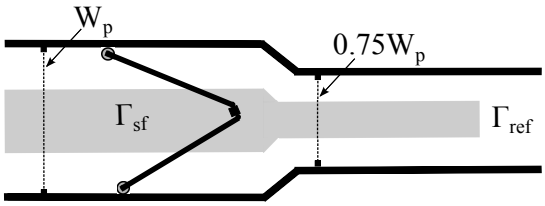

Figure 5.20: Configuration of the robot in a straight pipe using converged unconstrained parameters

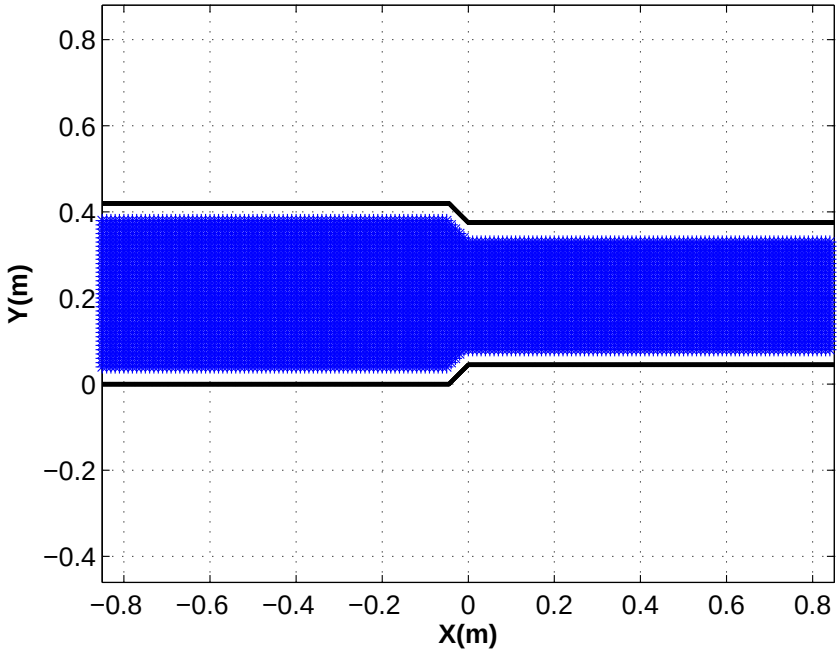

Figure 5.21: Γ_{sf} region using converged unconstrained parameters in a straight pipe, $\theta_\sigma = 0°$

5.6 Optimization in a 90° Elbow Pipe

To perform the design optimization in a 90° elbow pipe, the constrained optimization algorithm is first initialized. A representation of the robot with initial design parameters of $l = 0.5W_p$ and $a = 0.5$ is presented in figure 5.22. To be consistent with the optimization performed in a straight pipe, the design parameters representing the body of the robot are set to $w = 0.5W_p$ and $h = W_p$.

The 90° elbow pipe shown in figure 5.22 is divided into 9134 nodes to obtain a discrete

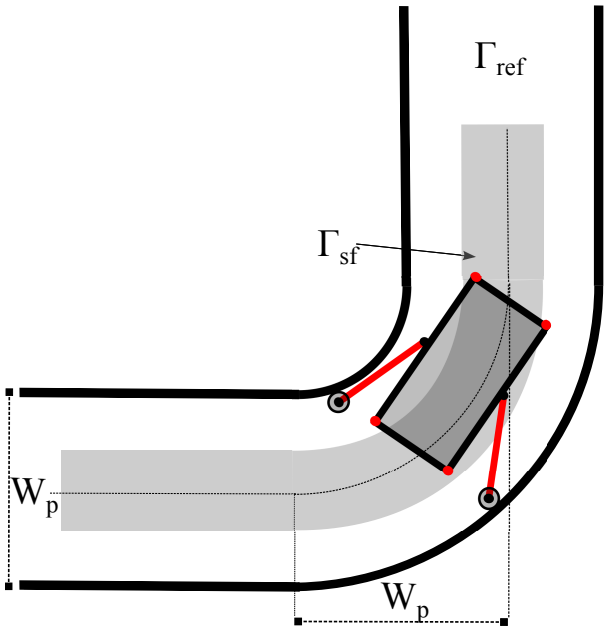

Figure 5.22: Configuration of the robot with initial design parameters in a 90° elbow pipe

Γ_{ref} region from which the nodes depicting Γ_{sf} are highlighted. The resultant Γ_{sf} region using the current initial parameters is shown in figure 5.23, when $\theta_\sigma = 0°$. The total number of discrete points composing Γ_{sf} region is 4068. Therefore, the resulting value of the objective function $\mathbf{F}(\chi)$ when $\theta_\sigma = 0°$ is

$$\mathbf{F}(\chi) = \mathbf{F}(\ 0.5,\ 0.5\ \ 1.0\ \ 0.5\ ) = \frac{\Gamma_{sf}}{\Gamma_{ref}} = \frac{4068}{9134} = 0.44$$

This means that, using the initial parameters the robot is able to reach 44% of Γ_{ref} region. Table 5.4 shows the values of parameter l and a at various iterations during the optimization process. Converged design parameters are obtained at the 4^{th} iteration, where $l = 0.78W_p$ and $a = 0.94$. A configuration of the robot representing these design parameters is shown in figure 5.24.

Figure 5.25 shows the average cost function value with respect to θ_σ for various values of parameter l. It can be observed that the average value of the cost function is maximum and constant near a value of 0.18, when $0.55W_p \leq\ l\ \leq 0.9W_p$. In order to select the most appropriate value of l, the cost function versus θ_σ for various design parameter l are plotted in figure 5.26. Among the values of parameter l in figure 5.25, a value which maximizes the cost function is $l = 0.78W_p$.

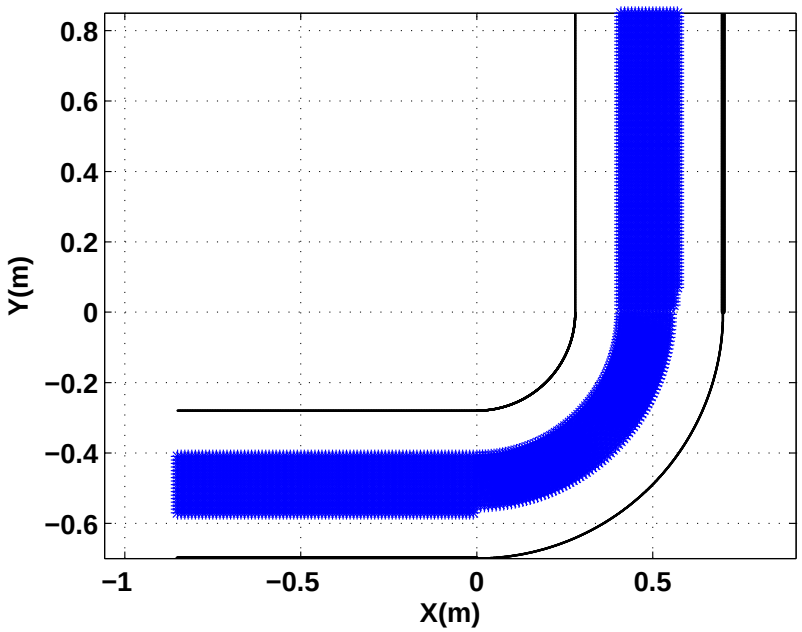

Figure 5.23: Γ_{sf} using initial parameters in a 90° elbow pipe, $\theta = 0°$

Table 5.4: Optimization of design parameters in 90^o elbow pipe

Design Parameters	l	a
Initial parameter	0.5	0.5
$1^{st} Iteration$	0.5	0.8
$2^{nd} Iteration$	0.78	0.8
$3^{rd} Iteration$	0.78	0.94
Optimal Parameters		
$4^{th} Iteration$	0.78	0.94

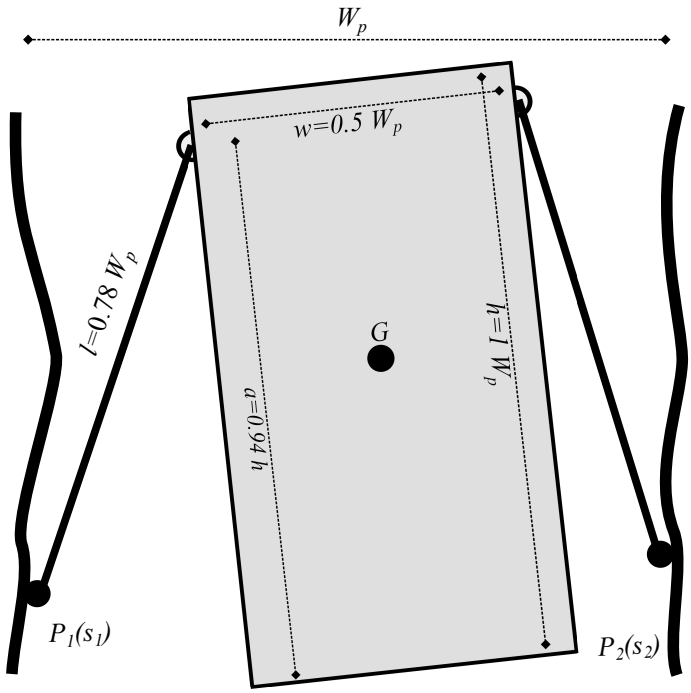

Figure 5.24: The geometry of the robot with optimal design parameters l and a in a 90° elbow pipe

Figure 5.27 shows the average cost function versus various values of parameter a. It can be observed that the maximum value of the average cost function is approximately 0.19 between $0.8 \leq\ a\ \leq\ 1$. Figure 5.28 shows the value of the cost function versus θ_σ for various values of parameter a. This graph is used to select the best overall value of $a = 0.94$ which maximizes the cost function when $-45° \leq \theta_\sigma \leq 45°$.

Figure 5.29 shows the configuration of the robot with converged design parameters in a 90° elbow pipe. Figure 5.8 shows the Γ_{sf} region using the converged design parameters. The total number of discrete points depicting a Γ_{sf} region is 4378 out of 9134 points of Γ_{ref}, when $\theta_\sigma = 0°$. This means that using the optimal parameters, the robot is able to cover approximately 48% of the prescribed Γ_{ref} region. This value is located at the peek of the curve represented by $l = 0.78W_p$ in figure 5.26.

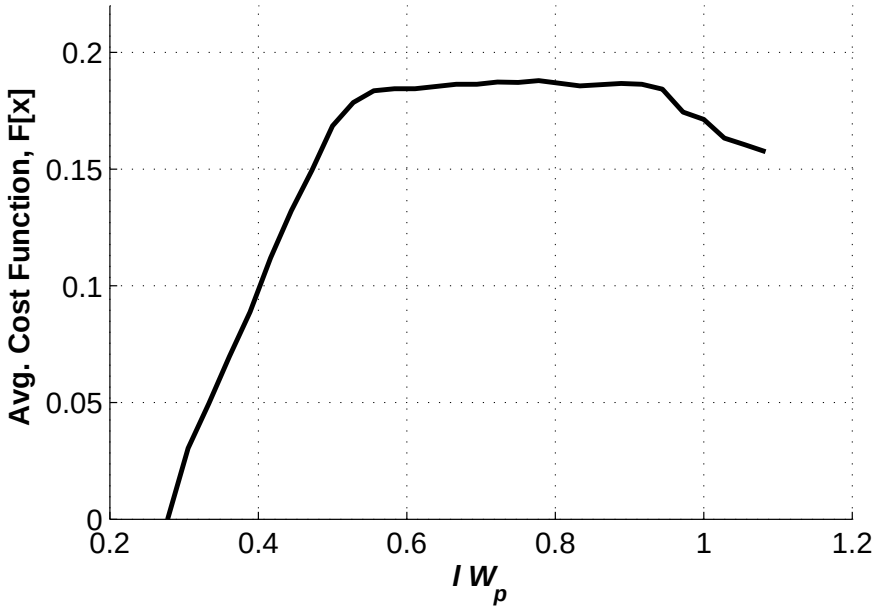

Figure 5.25: Average $\mathbf{F}(\chi)$ with respect to θ_σ for varied l

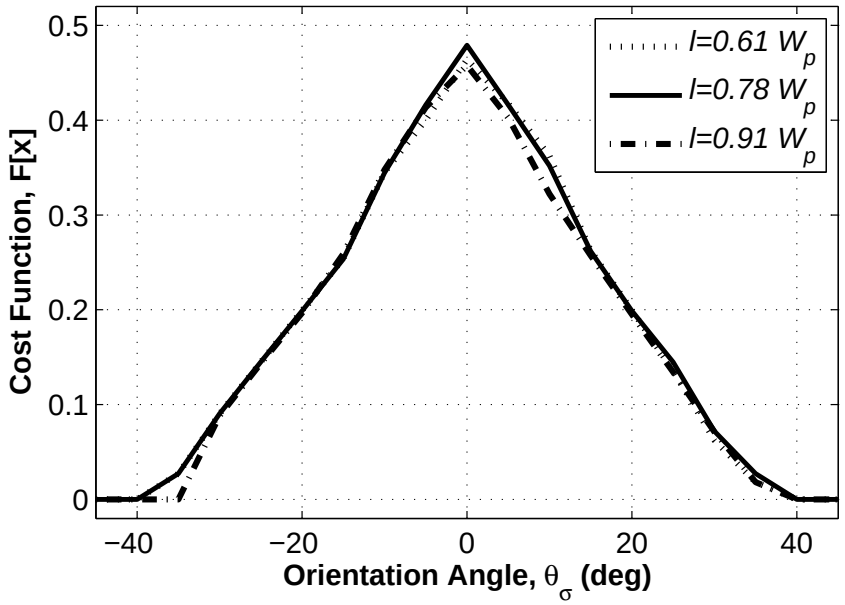

Figure 5.26: $\mathbf{F}(\chi)$ versus orientation angles θ_σ in 90° elbow pipe for various l

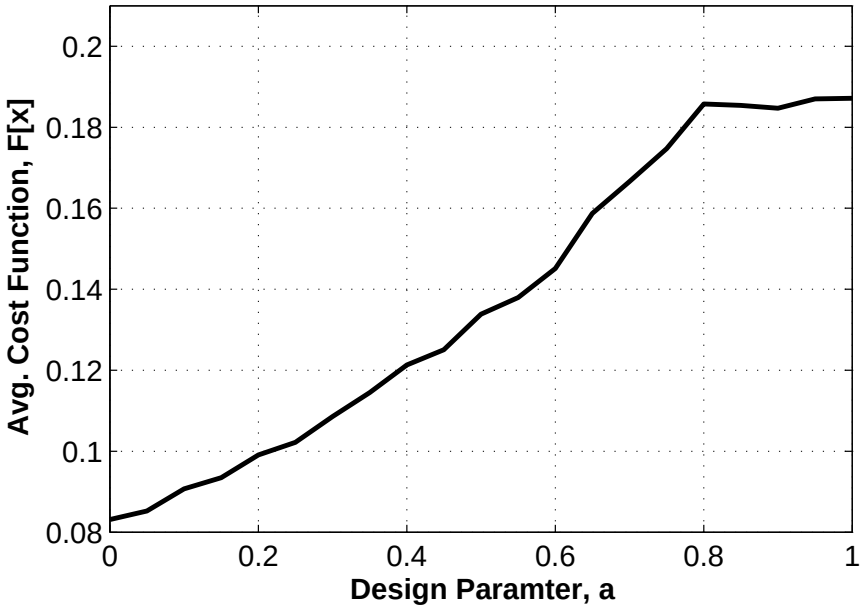

Figure 5.27: Average $\mathbf{F}(\chi)$ with respect to θ_σ for varied parameter a

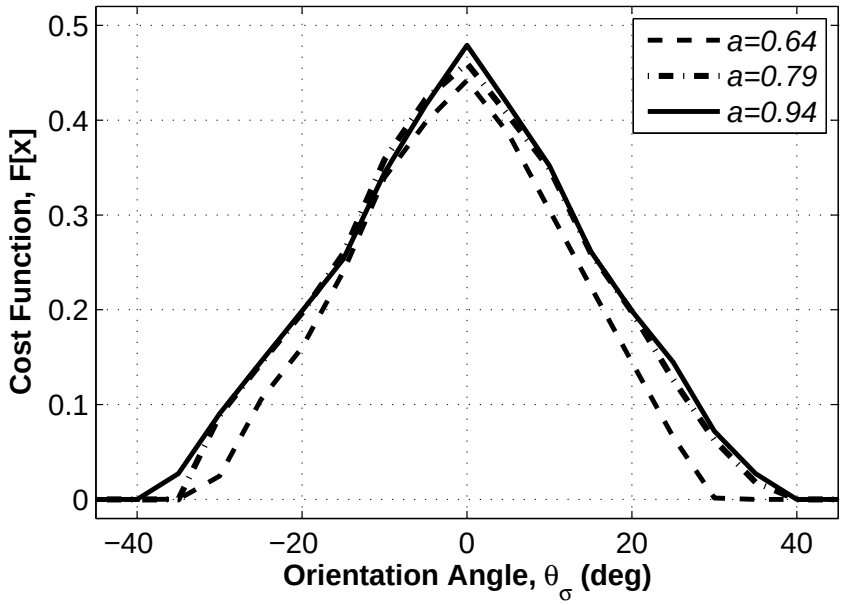

Figure 5.28: $\mathbf{F}(\chi)$ versus θ_σ in a 90° elbow pipe for various values of a

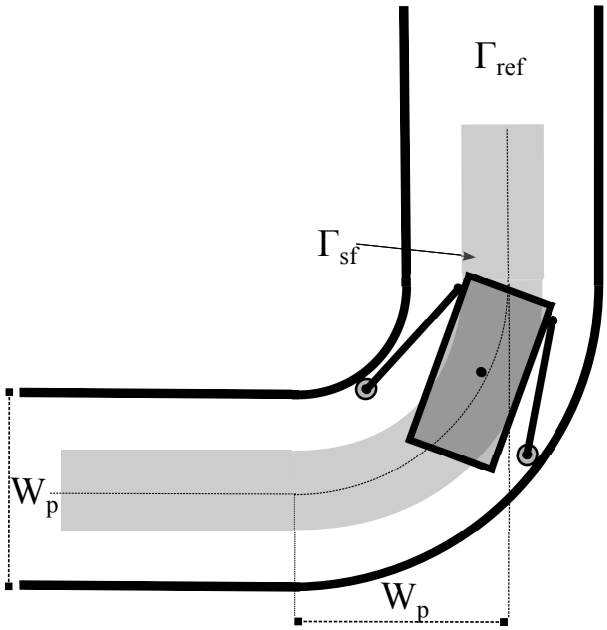

Figure 5.29: Configuration of the robot with optimal design in a 90° elbow

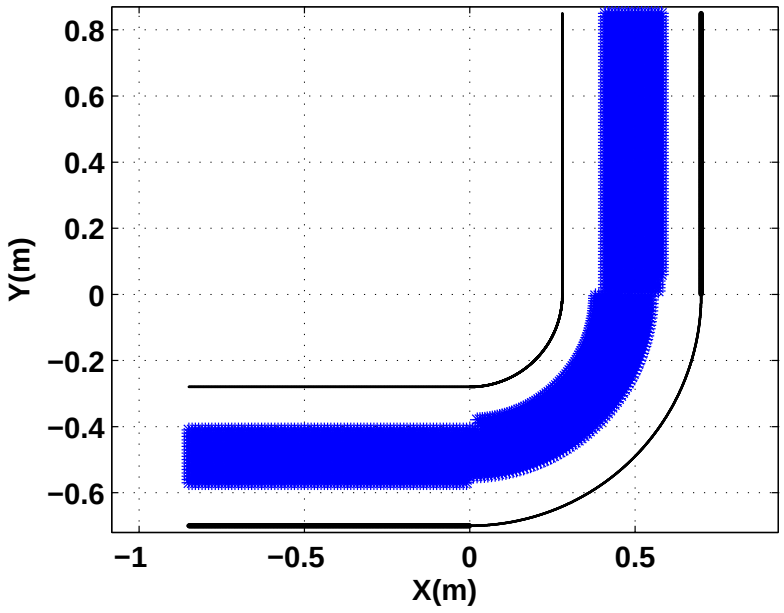

Figure 5.30: Γ_{sf} region in a 90° elbow, $\theta_\sigma = 0°$

5.7 Optimization in a 135° Elbow Pipe

In this section the design optimization is performed in a 135° elbow pipe. The initial design parameters are set as $l = 0.5W_p$, $w = 0.5W_p$. $h = W_p$ and $a = 0.5W_p$. A representation of the robot with these initial parameters is presented in figure 5.31. The

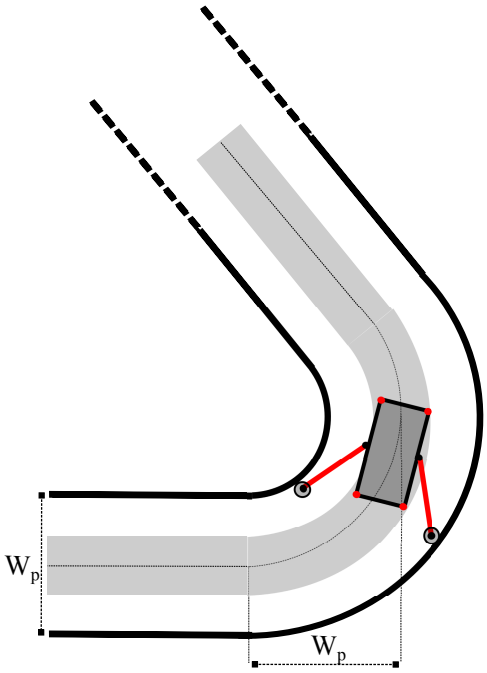

Figure 5.31: Configuration of the robot with initial design parameters in 135° elbow pipe

optimization algorithm divides the 135° elbow pipe in 10610 nodes to obtain a discrete Γ_{ref} region from which nodes depicting Γ_{sf} region are highlighted. Γ_{sf} region of the robot using the current initial parameters is shown in figure 5.32, when $\theta_\sigma = 0°$. The total number of discrete points composing Γ_{sf} region are 4856. Therefore, the resulting value of the cost function $\mathbf{F}(\chi)$ using initial parameters when $\theta_\sigma = 0°$ is

$$\mathbf{F}(\chi) = \mathbf{F}(\ 0.5,\ 0.5,\ 1.0,\ 0.5\ ) = \frac{\Gamma_{sf}}{\Gamma_{ref}} = \frac{4856}{10610} = 0.457$$

This means that the robot is able to cover 45.7% of Γ_{ref}.

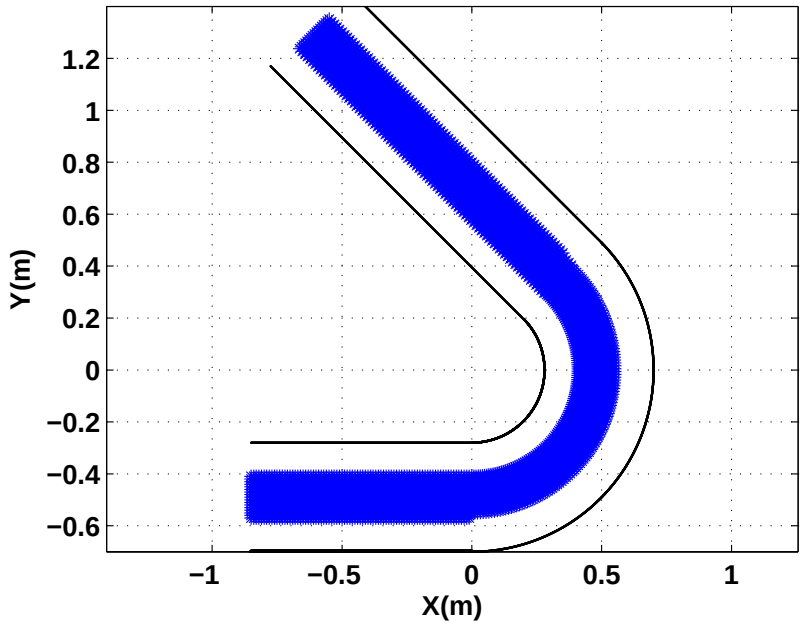

Figure 5.32: Γ_{sf} in a 135° elbow pipe using initial parameters, $\theta_\sigma = 0°$

The optimization is performed on design parameters l and a. The constant design parameters representing the body of the robot are set as $w = 0.5W_p$ and $h = W_p$. Table 5.5 shows the values of parameters l and a at various iteration during the optimization process. Converged design parameters are obtained at the 8^{th} iteration, $l = 0.75W_p$ and $a = 0.91$. The configuration of the robot with constant parameters $h = W_p$ and $w = 0.5W_p$ and optimal parameters l and a, is shown in figure 5.33.

Figure 5.34 shows the average cost function value over the span of θ_σ for various values of parameter l. It can be observed that the average value of the cost function is maximum when $0.5W_p \leq l \leq 0.9W_p$. Figure 5.35 shows values of the cost function against θ_σ for various values of parameter l. It can be seen that when $l = 0.75W_p$, the cost function is maximum around $\theta_\sigma = 0^o$.

Figure 5.36 shows the average cost function over the span of θ_σ for various values of parameter a. It can be observed that the maximum value of the average cost function is achieved when $0.9 \leq a \leq 1$. Figure 5.37 shows the value of the objective function against θ_σ for various values of parameter a. It can be seen that the cost function is maximum when $a = 0.9$ near $\theta_\sigma = 0°$. Hence, $a = 0.9$ is selected as an optimal value.

Figure 5.38 shows the configuration of the robot with optimal design parameters

Table 5.5: Optimization of design parameters in a 135° elbow pipe

Design Parameters	l	a
Initial parameter	0.5	0.5
$1^{st} Iteration$	0.5	0.6
$2^{nd} Iteration$	0.55	0.6
$3^{rd} Iteration$	0.55	0.8
$4^{th} Iteration$	0.61	0.8
$5^{th} Iteration$	0.61	0.88
$6^{nd} Iteration$	0.75	0.91
$7^{rd} Iteration$	0.75	0.91
Optimal Parameters		
$8^{th} Iteration$	0.75	0.91

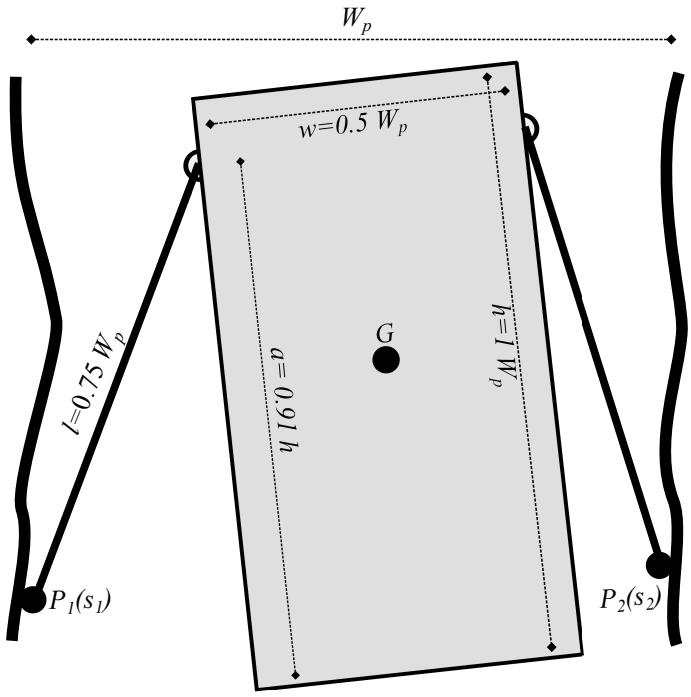

Figure 5.33: Configuration of the robot with constrained optimal design parameters l and a

in a 135° elbow pipe. Figure 5.7 shows Γ_{sf} region as a result of these optimal design parameters. The total number of discrete points depicting Γ_{sf} region are 5207 out of

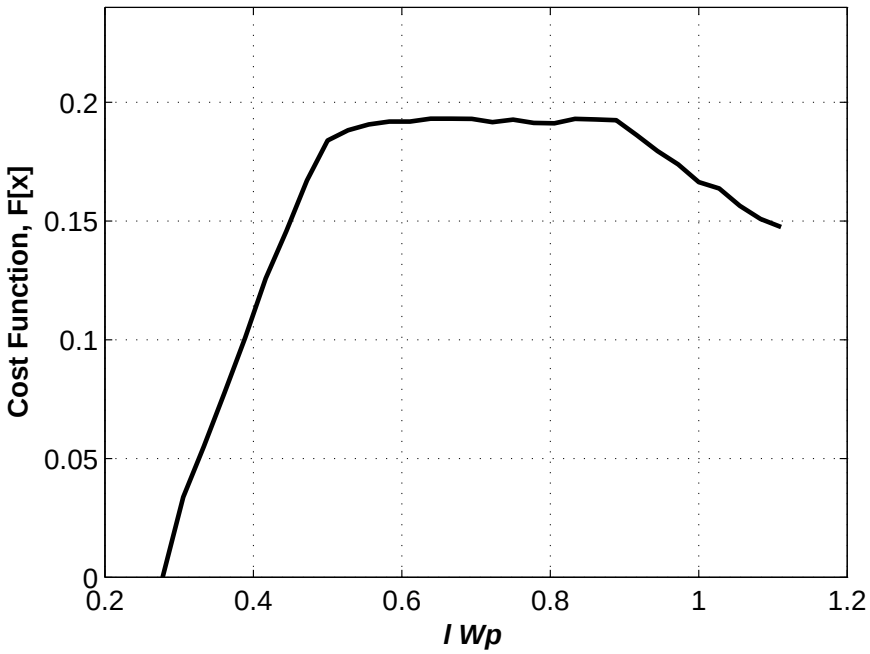

Figure 5.34: Average $\mathbf{F}(\chi)$ with respect to θ_σ for varied l

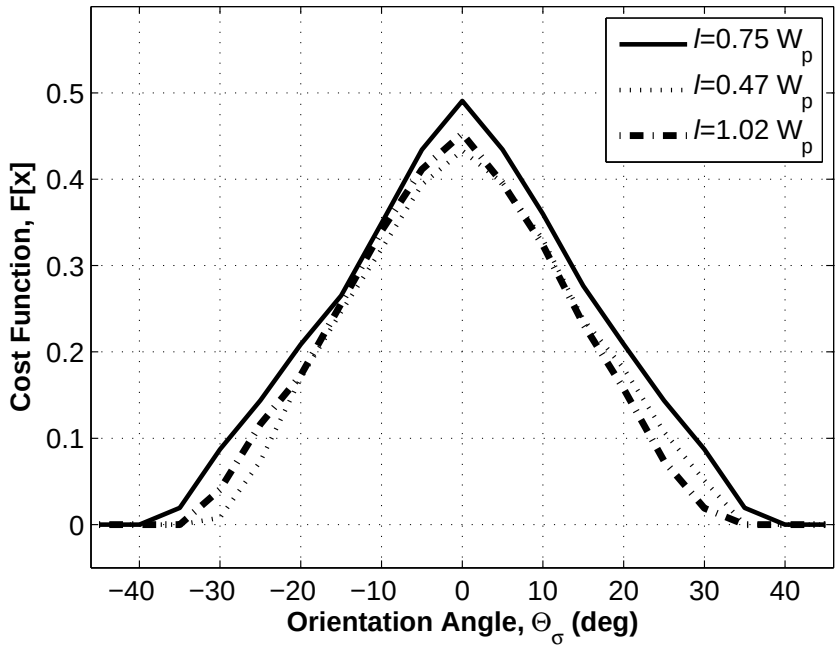

Figure 5.35: $\mathbf{F}(\chi)$ versus orientation angles (θ_σ) in 135^o Elbow Pipe for various l

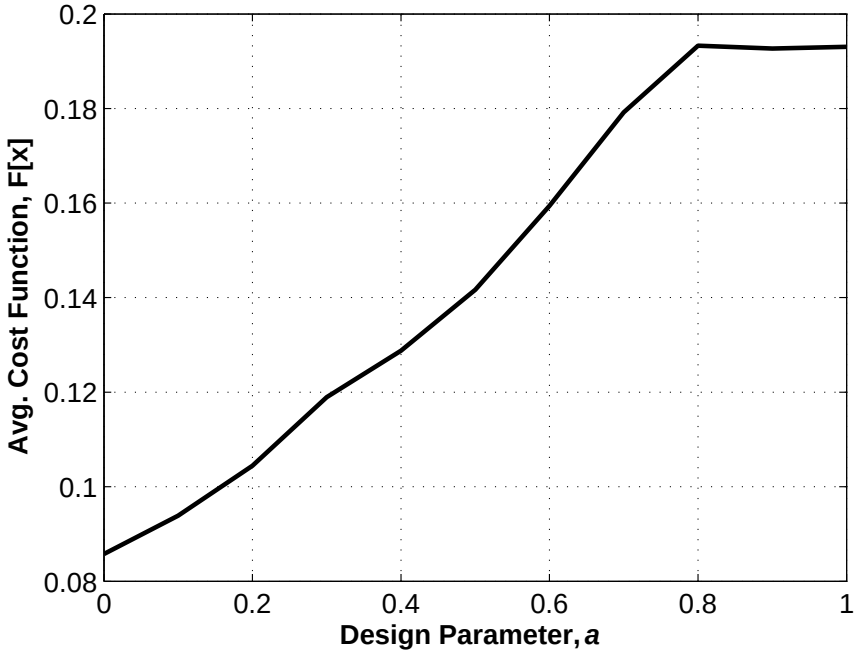

Figure 5.36: Average $\mathbf{F}(\chi)$ with respect to θ_σ for varied a

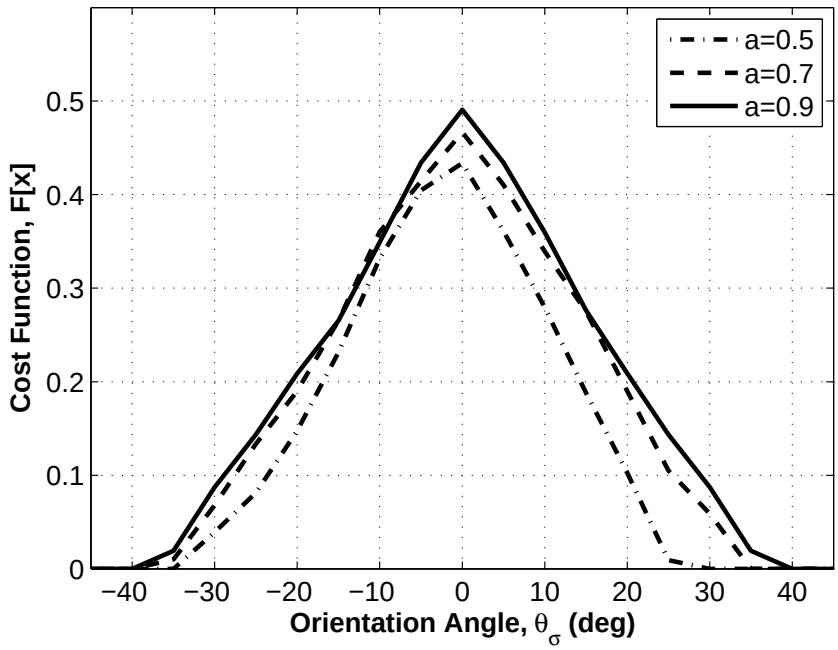

Figure 5.37: $\mathbf{F}(\chi)$ versus θ_σ in 135° elbow pipe for various a

10610 points of Γ_{ref}, when $\theta_\sigma = 0°$. This point is located at the peek of the curve represented by $l = 0.75W_p$ in figure 5.35.

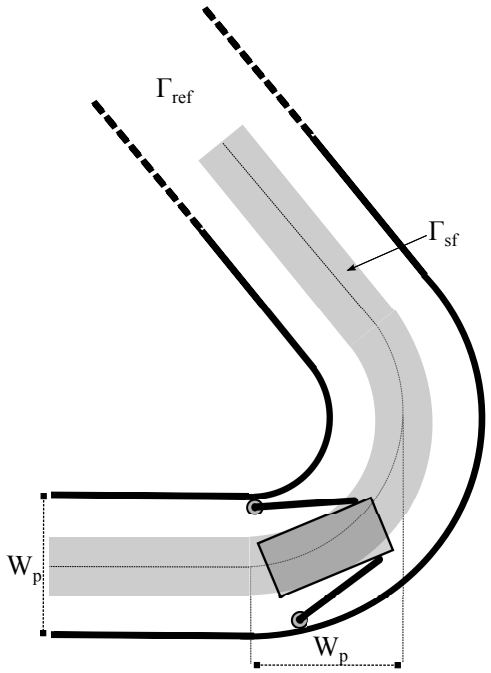

Figure 5.38: Configuration of the robot with optimal design in a 135^o elbow pipe

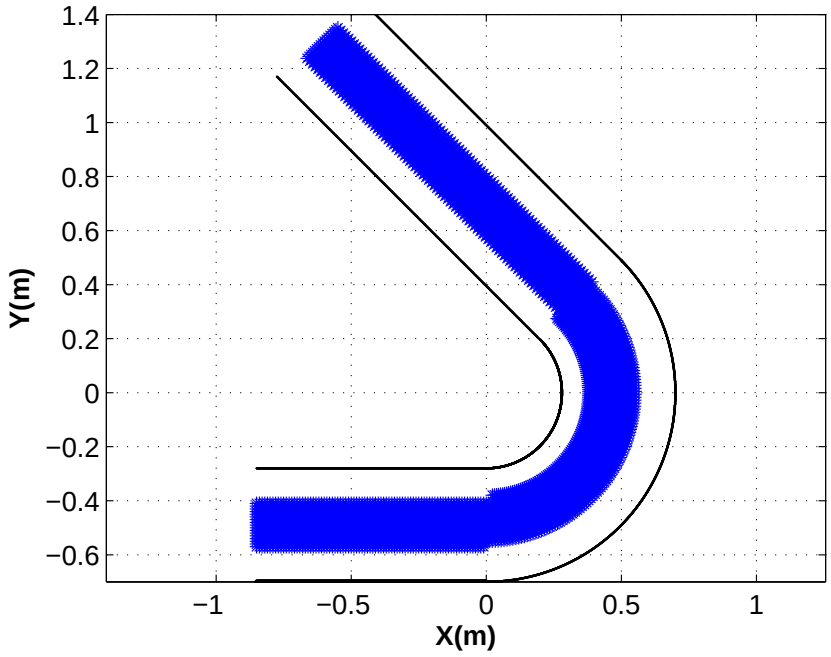

Figure 5.39: Γ_{sf} region in a 135° elbow, $\theta_\sigma = 0°$

5.8 Optimization in a 180° Elbow Pipe

In this section design optimization is performed in a 180° elbow pipe. A representation of a mobile parallel robot with initial parameters is presented in figure 5.40. As mention during the design optimization in a straight pipe, the design parameters w and h are kept constant with values of $w = 0.5W_p$ and $h = W_p$ The optimization algorithm grids the 180° elbow pipe in 11808 nodes to obtain a discrete Γ_{ref} region from which Γ_{sf} region is highlighted for a given θ_σ. The total number of discrete points making Γ_{sf} region are 5261. Therefore, the resulting value of the objective function using initial parameters and $\theta_\sigma = 0°$ is

$$\mathbf{F}(\chi) = \mathbf{F}(\ 0.5,\ 0.5,\ 1.0,\ 0.5\ ) = \frac{5261}{11808} = 0.445$$

This means that the robot is able to reach 44.5% of Γ_{ref}. Table 5.6, shows the values of parameter l and a at various iterations during the optimization process. Converged design parameters are obtained at the 4^{th} iteration, $l = 0.75W_p$ and $a = 0.9$. The design parameters $l = 0.75W_p$ and $a = 0.9$ maximizes the cost function, when parameter $h = W_p$ and $w = 0.5W_p$. A configuration of the robot representing these parameters is shown in figure 5.41. In this figure, the mobile planar parallel robot is shown in an arbitrary

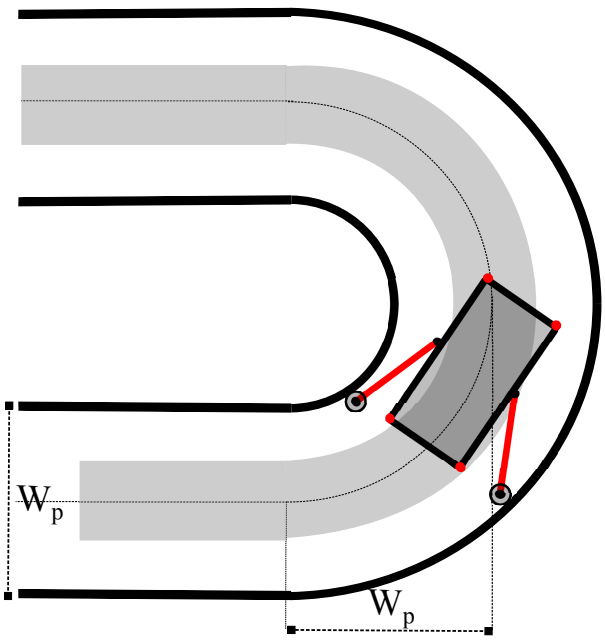

Figure 5.40: Configuration of the robot with initial design parameters in a 180° elbow pipe

confined environment with all of its design parameters normalized with respect to W_p.

Figure 5.42 shows the average cost function value over the span of θ_σ for various values of parameter l. It can be observed that the average value of the cost function is maximum when $0.5W_p \leq \ l \ \leq 0.8W_p$. In order to select the most appropriate value of l, the cost function versus θ_σ for various values of l are plotted in figure 5.43. Overall, $l = 0.75W_p$ maximizes the cost function around $\theta_\sigma = 0°$. Figure 5.44 shows the average cost function with respect to θ_σ for various values of parameter a. It can be observed that the maximum value of the average cost function is achieved when $0.8 \leq \ a \ \leq \ 1$. Figure 5.45 shows values of the cost function versus θ_σ for various values of parameters a. Overall, $a = 0.9$ maximizes the cost function when $-45° \leq \theta_\sigma \leq 45°$.

Figure 5.46 shows the robot with optimal design parameters in a 180° elbow pipe. Figure 5.8 shows Γ_{sf} region of the robot with optimal design parameters. The total number of discrete points depicting a Γ_{sf} region is 5261 out of 11808 points in Γ_{ref}, when $\theta_\sigma = 0°$.

$$\mathbf{F}(\chi) = \frac{\Gamma_{sf}(\ 0.7,\ 0.5,\ 1.0,\ 1.0\ )}{\Gamma_{ref}} = \frac{5725}{11808} = 0.48$$

This means that using the optimal parameters the robot is able to reach 48% of Γ_{ref} region.

Table 5.6: Optimization of design parameters in 180° elbow pipe

Design Parameters	l	a
Initial parameter	0.5	0.5
$1^{st} Iteration$	0.5	0.8
$2^{nd} Iteration$	0.75	0.80
$3^{rd} Iteration$	0.75	0.9
Optimal Parameters		
$4^{th} Iteration$	0.75	0.9

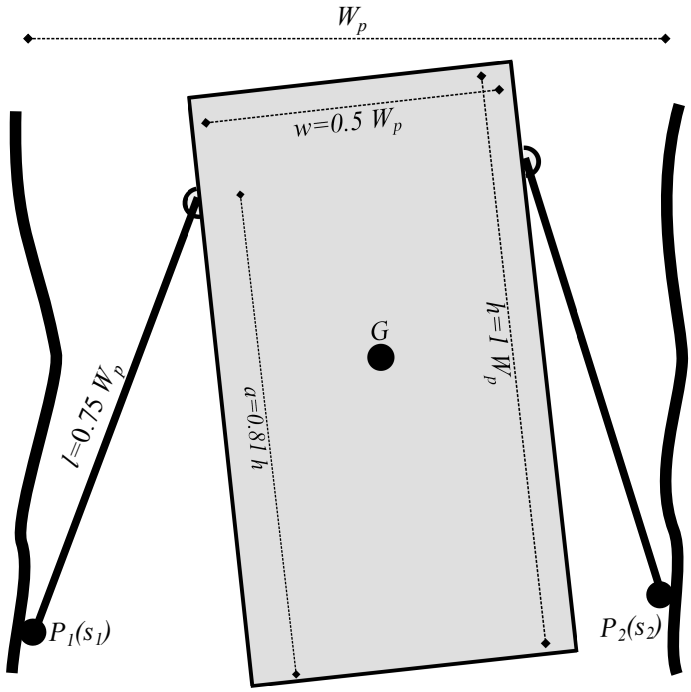

Figure 5.41: Configuration of the robot with optimal design parameters in 180° elbow

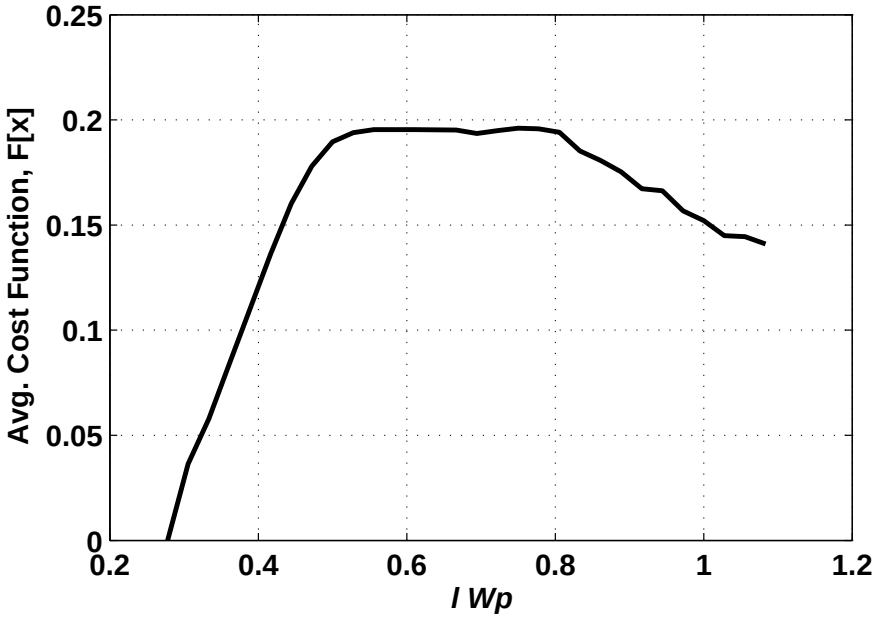

Figure 5.42: Average $\mathbf{F}(\chi)$ with respect to θ_σ for varied l

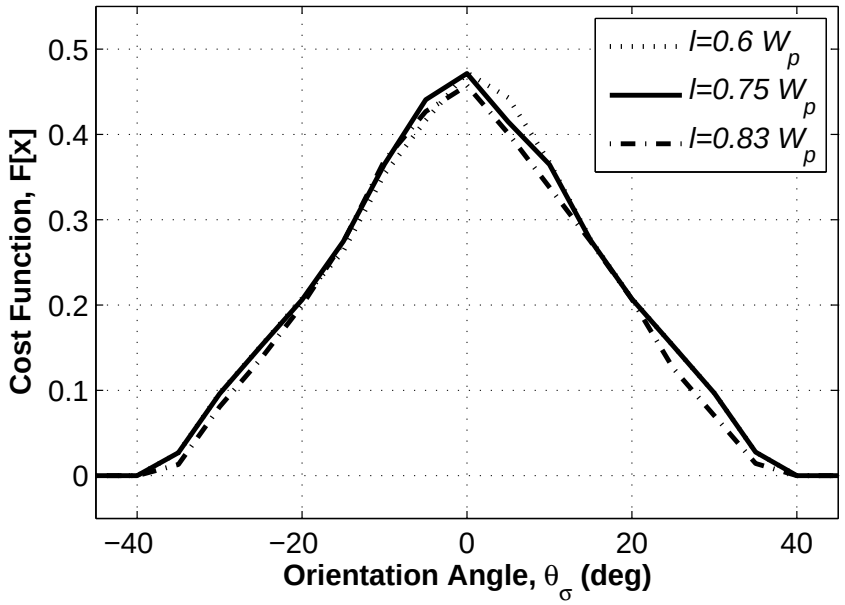

Figure 5.43: $\mathbf{F}(\chi)$ versus orientation angles (θ_σ) in 180^o elbow pipe for various l

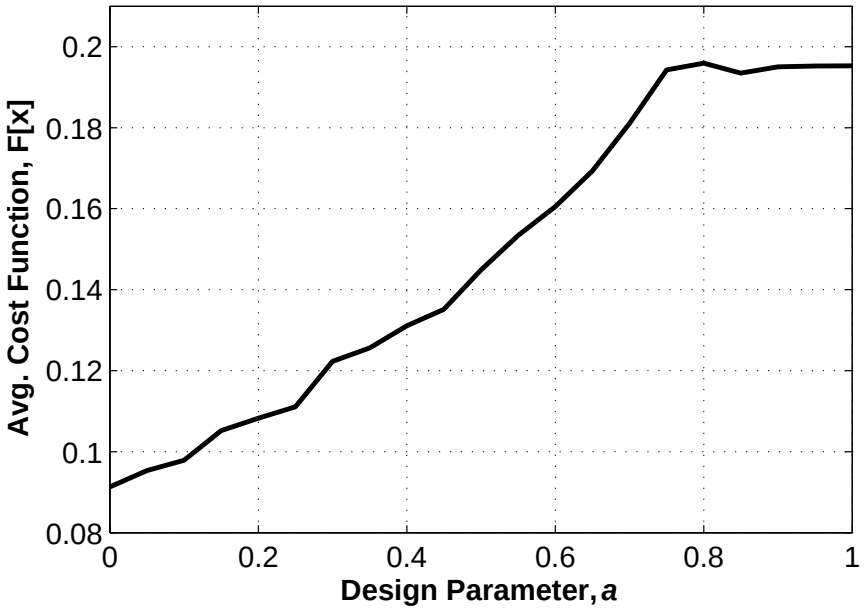

Figure 5.44: Average $\mathbf{F}(\chi)$ with respect to θ_σ for varied a

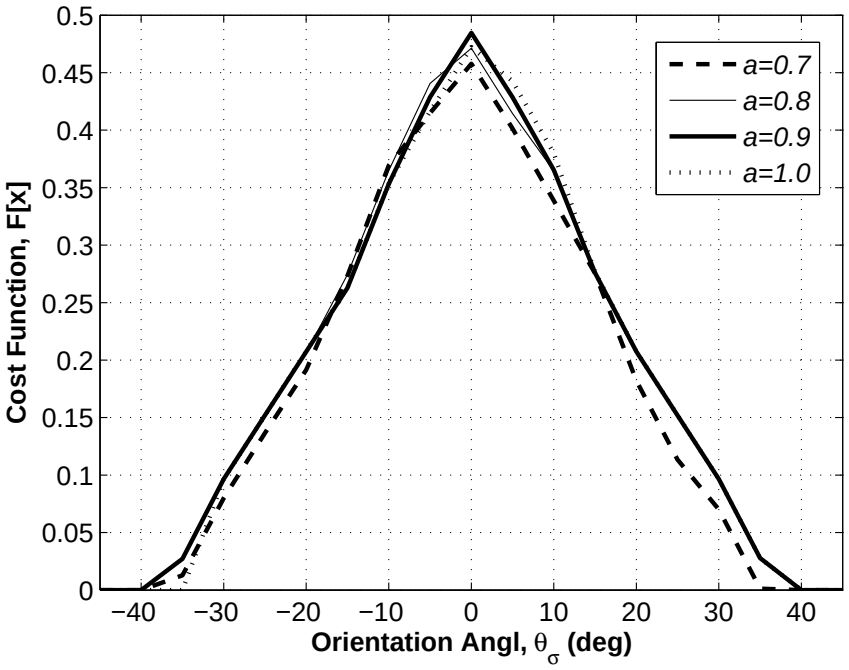

Figure 5.45: $\mathbf{F}(\chi)$ versus θ_σ in 180° elbow pipe for various a

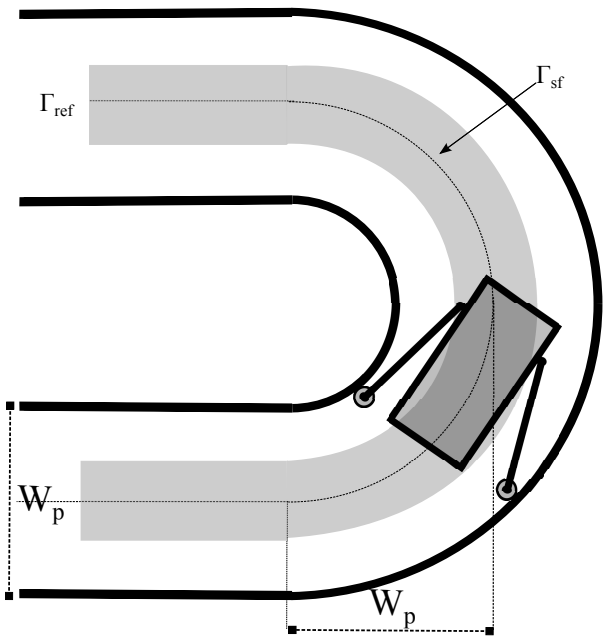

Figure 5.46: Configuration of the robot with optimal design in a 180° elbow pipe

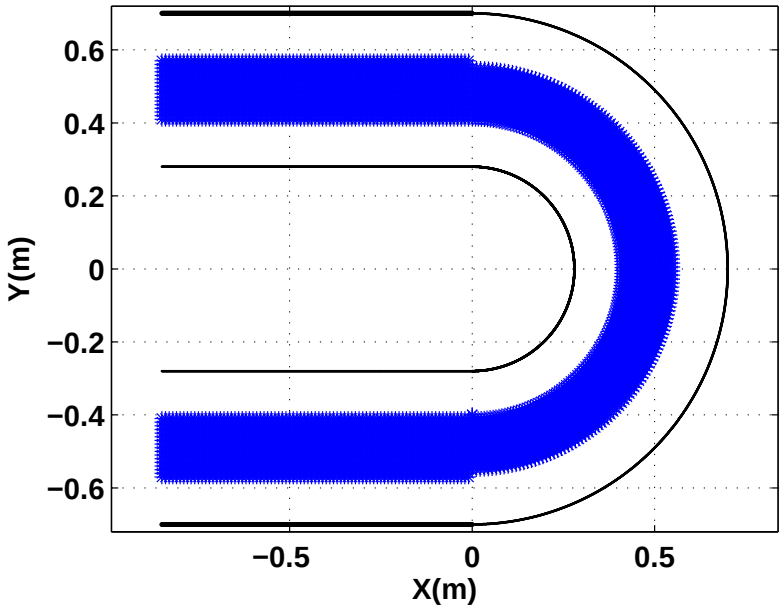

Figure 5.47: Γ_{sf} region in a 180° elbow, $\theta_\sigma = 0°$

5.9 Chapter Summary

In this chapter, the design parameters, l, w, h and a representing the geometry of the robot are optimized to enhance the performance of the robot, in terms of maximization of a reachable workspace and the minimization of singular configurations. Furthermore, four types of constraints, such as singularity avoidance, collision avoidance, workspace continuity, and contact constraint imposed between the boundaries and wheels of the robot lead to the formulation of an optimization problem. Parametric Variation method is used as a discrete optimization technique.

Furthermore, the design optimization is performed in four different types of pipe-like structures. These pipe-like structures include a straight pipe with varying diameters, 90° elbow, 135° elbow and 180° elbow pipe. The discrete optimization problem is formulated by providing a range of possible values which the design parameters may attain in order to satisfy the kinematic constraints of the robot. The algorithm is initialized by discretely defining Γ_{ref} for a given orientation angle, θ_σ. The initial design parameters are selected as $l = 0.5W_p$, $w = 0.5W_p$, $h = 0.5W_p$ and $a = 0.5$ in order to fit the robot into the pipe with width of W_p. The discrete optimization algorithm is described in details using a flowchart. The design optimization performed without setting any lower or upper bound on the design parameters provides a solution which is not feasible, since it requires the body of the robot of sides h and w to approach zero. Therefore, a constrained design optimization was performed by setting w and h as constants and optimizing only l and a. The resulting optimal parameters provides a feasible design solution which maximizes singularity-free workspace of the robot. The optimal value of parameters l and a highly depends on the constant values of w and h, since as w and h approach zero the cost function is maximized.

Chapter 6

Optimal Control in a Geometrically Singular Pipe

6.1 Introduction

In this chapter we consider the scenario of the robot in a geometrically singular environment, that is a pipe-like structure with a sharp elbow as illustrated in Figure 6.1. The sharp 90° elbow combines two straight pipes mutually orthogonal. The outer diameter of pipe is constant and denoted by W_p. It is important to verify the existence of a continuous Γ_{sf} region in this type of pipe structure. The region between the pipe boundaries in Figure 6.1 represents a prescribed reference workspace Γ_{ref} from which Γ_{sf} can be determined. To successfully cross the robot through this critical scenario a path-following control together with an optimal control is formulated as an optimization problem, with optimization function encoding singularity quantification and collision avoidance.

6.2 Mobility Analysis

In this section, workspace and singularity analysis on a mobile parallel robot is performed in sharp 90° elbow pipe. The pipe-like structure shown in figure 6.1 is used as a reference to perform this analysis. The design parameters considered here are l (length of arms), w (width), h (height), and a (position of the pin of the arm). These design parameters are non-dimensionalized with respect to the width of the pipe, W_p, which is constant throughout the pipe. A representation of a mobile parallel robot with design parameters equal to $l = 0.75W_p$, $h = W_p$, $w = 0.5W_p$ and $a = 0.9$ is presented in figure 6.1. These

values are global optimal design parameters as obtained in chapter 5. It can be seen that using these parameters the robot is able to fit inside the pipe, and at the same time satisfy other design requirements, as for example the minimum area to install the batteries, motors and electronics.

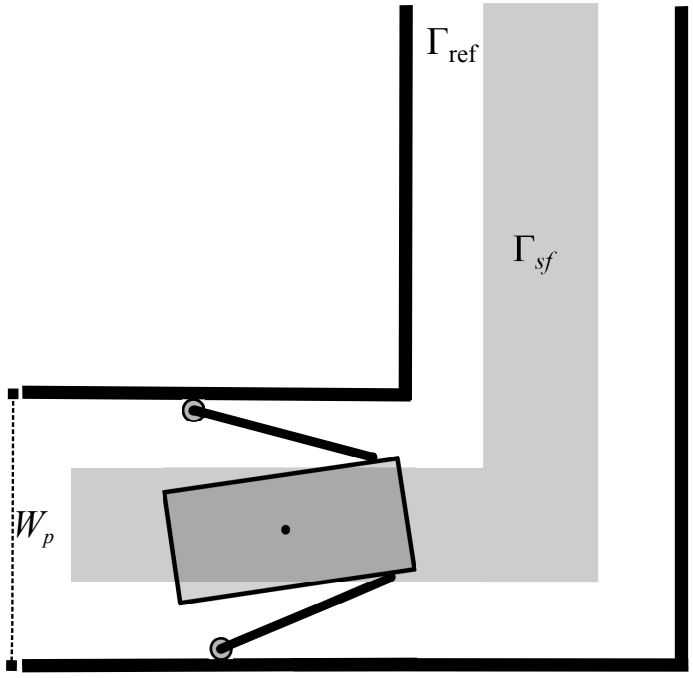

Figure 6.1: Representation of the robot in 90° Sharp Elbow Pipe

When operating autonomously in a pipe-like environment, a typically challenging manoeuvre is the one related to a sharp 90° angle elbow as illustrated in Figure 6.2, where the corner introduces a jump discontinuity in the orientation of the path. It is important to obtain a continuous path without singularities during the turn. The orientation of the robot is tangent to the center line of the pipe which is 0° with respect to the global reference frame as it moves in the horizontal straight pipe. As the robot reaches the corner, it changes its orientation to 90° angle with respect to the global reference frame and proceeds in to the vertical straight pipe. The line which defines the change of orientation with respect to the global reference frame is a diagonal line which joins the two pipe segments together. Figure 6.3 shows the workspace of the robot with orientation of the module tangent to the center line. The availability of the workspace is represented by the blue coloured regions. As the robot moves into the vertical pipe the Γ_{sf} exists as long as the wheels of the robot are in contact with the horizontal pipe.

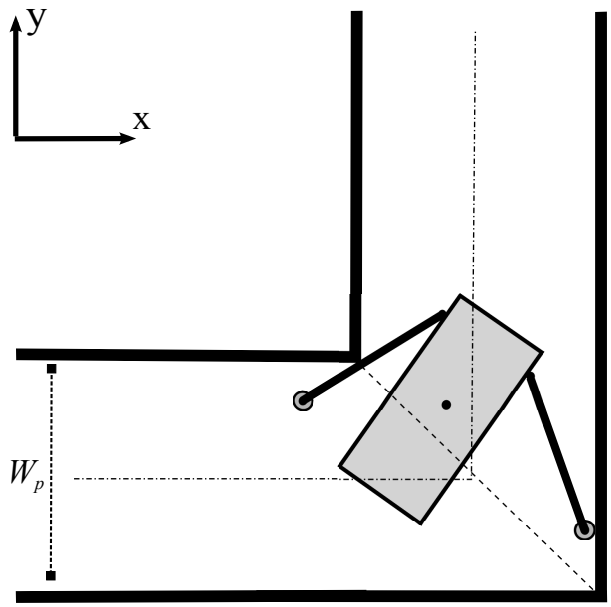

Figure 6.2: Collision of mobile parallel robot in a sharp 90° elbow pipe-like structure

The discontinuity in Γ_{sf} is due to change in the orientation which in turn implies the constraint violation $\alpha_r > 90°$ in order for the wheels to be in contact with the wall of the pipe. This type of serial configuration is illustrated in Figure 4.4, where the right arm is normal to the wall. Note that even when the robot enters the vertical pipe the discontinuity in Γ_{sf} persists for a certain span. This is due to the fact that the left arm collides with the left wall as illustrated in figure 6.2. When the left wheel can physically be in contact with the left wall on the vertical pipe and the system satisfies all kinematic constraints, the workspace exists.

6.3 Modified Mobile Planar Parallel Robot: Variable length arms

The discontinuity in the workspace depends on the parameters w and l. This is due to the fact that the arms or body of the robot collide with pipe walls and consequently the wheels loose contact with the walls while executing the turn. In order to avoid singularities, the module's width and height can be reduced. However, this requires increasing the length of the arms to satisfy the constraints of the wheels being in contact with the walls. Moreover, having relatively long arms makes it difficult to cross the sharp elbow. Here

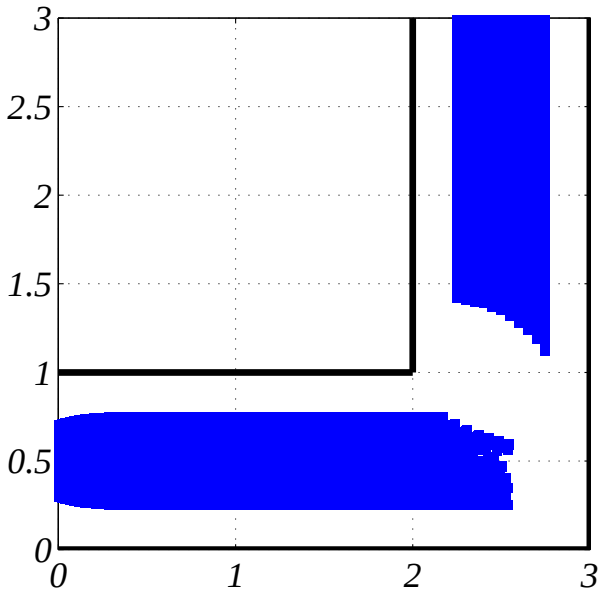

Figure 6.3: Γ_{sf}, singularity-free workspace analysis in a sharp 90° elbow pipe-like structure

we exploit the possibility of adding a prismatic joint on the arms so that the arms length can change during the operation. This allows to overcome the geometric singularities inherently leading to singularities in the Jacobian of the system. The modified mechanism is schematized in figure 6.4. The position kinematics is described by the following set of four equations, which extend the closure equation presented in equation 3.2, with the length of the arms as two additional parameter defining the configuration of the robot. The two parameters are d_1 and d_2, that are the degrees of freedom of prismatic joints on the left and right arm, respectively:

$$\begin{aligned}
x_G &= x_{P_1}(s_1) + \frac{w}{2}\cos\theta + h\left(a - \frac{1}{2}\right)\sin\theta + (d_1 + l)\sin(\alpha_1 - \theta) \\
y_G &= y_{P_1}(s_1) + \frac{w}{2}\sin\theta - h\left(a - \frac{1}{2}\right)\cos\theta + (d_1 + l)\cos(\alpha_1 - \theta) \\
(d_1 + l)\sin(\alpha_1 - \theta) &+ (d_2 + l)\sin(\alpha_2 - \theta) + w\cos\theta - (x_{P_2}(s_2) - x_{P_1}(s_1)) = 0 \\
(d_1 + l)\cos(\alpha_1 - \theta) &- (d_2 + l)\cos(\alpha_2 - \theta) + w\sin\theta - (y_{P_2}(s_2) - y_{P_1}(s_1)) = 0
\end{aligned} \tag{6.1}$$

Considering the parameters d_1, d_2, s_1, s_2, α_1, α_2, θ, x_G and y_G, the closure equation introduces four scalar relations between the nine parameters describing the kinematics; therefore the system has five degrees of freedom. The velocity kinematics is obtained by taking

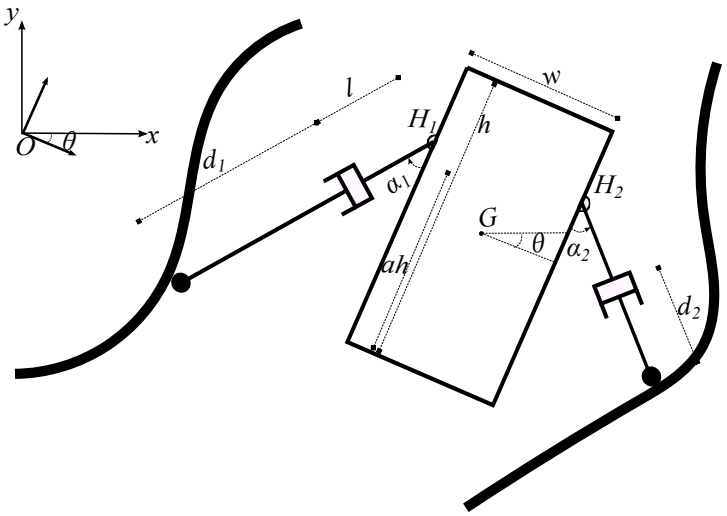

Figure 6.4: Configuration of a mobile parallel robot with prismatic arms

the time derivative of equation 6.1. Redefining the state vector as $x = (x_G, y_G, \theta, d_1, d_2)^T$, the velocity equations can be written in matrix form as $J_q\dot{q} = J_x\dot{x}$, where the Jacobians, J_q and J_x are now given by

$$J_q = \begin{pmatrix} (d_1+l)\cos(\alpha_1-\theta) & 0 & \frac{dx_{p_1}(s_1)}{ds_1} & 0 \\ -(d_1+l)\sin(\alpha_1-\theta) & 0 & \frac{dy_{p_1}(s_1)}{ds_1} & 0 \\ -(d_1+l)\cos(\alpha_1-\theta) & -(d_2+l)\cos(\alpha_2+\theta) & -\frac{dx_{p_1}(s_1)}{ds_1} & \frac{dx_{p_2}(s_2)}{ds_2} \\ (d_1+l)\sin(\alpha_1-\theta) & -(d_2+l)\sin(\alpha_2+\theta) & -\frac{dy_{p_1}(s_1)}{ds_1} & \frac{dy_{p_2}(s_2)}{ds_2} \end{pmatrix}$$

$$J_x = \begin{pmatrix} -1 & 0 & h(a-\frac{1}{2})\cos(\theta) - \frac{w}{2}\sin(\theta) - (d_1+l)\cos(\alpha_1-\theta) & \sin(\alpha_1-\theta) & 0 \\ 0 & -1 & h(a-\frac{1}{2})\sin(\theta) + \frac{w}{2}\cos(\theta) + (d_1+l)\sin(\alpha_1-\theta) & \cos(\alpha_1-\theta) & 0 \\ 0 & 0 & (d_1+l)\cos(\alpha_1-\theta) - (d_2+l)\cos(\alpha_2+\theta) + w\sin(\theta) & -\sin(\alpha_1-\theta) & -\sin(\alpha_2+\theta) \\ 0 & 0 & -(d_1+l)\sin(\alpha_1-\theta) - (d_2+l)\sin(\alpha_2+\theta) - w\cos(\theta) & -\cos(\alpha_1-\theta & \cos(\alpha_2+\theta)) \end{pmatrix}$$

6.4 Path-Following and Optimal Trajectories

As explained in the previous section the singularities associated to the discontinuity region in the workspace are due to the lack of contact between one arm extremity (wheel) and the wall, which translates into constraints violations. A measure of singularity is the proximity of $det(J_x {J_x}^T)$ to zero, where the expression of the determinant obtained with

Mathematica is

$$\begin{aligned}
det(J_x {J_x}^T) = \frac{1}{8}(4 + 20d{d_2}^2 + (1-2a)^2h^2 + 20({d_1}^2) + 2d_1l + 2l(d_2+l) + llw^2 \\
- 4(-1+2a)h(d_1+l)\cos(\alpha_1) - 4(-1+2a)h(d_2+l)\cos(\alpha_2) \\
- 48d_1d_2\cos(\alpha_1+\alpha_2) - 48d_1l\cos(\alpha_1+\alpha_2) - 48d_2l\cos(\alpha_1+\alpha_2) \\
- 48l^2\cos(\alpha_1+\alpha_2) - 4\cos(2(\alpha_1+\alpha_2)) + 4{d_1}^2\cos(2(\alpha_1+\alpha_2)) \\
+ 4{d_2}^2\cos(2(\alpha_1+\alpha_2)) - h^2\cos(2(\alpha_1+\alpha_2)) + 4ah^2\cos(2(\alpha_1+\alpha_2)) \\
- 4a^2h^2\cos(2(\alpha_1+\alpha_2)) + 8d_1l\cos(2(\alpha_1+\alpha_2)) + 8d_2l\cos(2(\alpha_1+\alpha_2)) \\
+ 8l^2\cos(2(\alpha_1+\alpha_2)) - 4d_2h\cos(2\alpha_1+\alpha_2) + 8ad_2hcos(2\alpha_1+\alpha_2) \\
- 4hl\cos(2\alpha_1+\alpha_2) + 8ahl\cos(2\alpha_1+\alpha_2) \\
+ 4(-1+2a)h(d_1+l)\cos(\alpha_1+\alpha_2) \\
+ w(w(-6(\cos(2\alpha_1)+\cos(2\alpha_2)) + \cos(2(\alpha_1+\alpha_2)))) \\
+ 4(\sin(\alpha_1)(9(d_{1+l}) + 2(1-2a)h\sin(\alpha_2)\sin(\alpha_1+\alpha_2))) \\
- 3(d_2+l)(-3\sin(\alpha_2)) - 3(d_1+l)\sin(\alpha_1+2\alpha_2))
\end{aligned}$$

The system is indeed singular if at least one singular value of J_x is zero, see Spong et al. [70]. Since the eigenvalues of $det(J_x {J_x}^T)$ are the squares of the singular values of J_x, it follows that the determinant in the equation above is zero when the system is singular. We decompose the state vector $\mathbf{x}$ as

$$\mathbf{x} = (\mathbf{z}\ \mathbf{d})^T$$

where

$$\mathbf{z} = (x_G, y_G, \theta)^T$$

and

$$\mathbf{d} = (d_1\ d_2)^T$$

. The motion control of the module inside the pipe is simulated by combining a path following control and an optimal control that maximizes the metric $det(J_x {J_x}^T)$. The path following portion of the algorithm updates the state $\mathbf{z}$ at discrete time instants according to

$$\mathbf{z}(k+1) = \gamma^d(k+1) + [\mathbf{I} - \delta_k\mathbf{K}]\,(\mathbf{z}(k) - \gamma^d(k))$$

where k is an integer corresponding to the discrete time index, $\mathbf{K}$ is a symmetric positive definite gain matrix, δ_k is the updating time interval, and γ^d is the desired state for $\mathbf{z}$,

which is a vector containing the parametric (with respect to the arc length) coordinates of the point of the path that is nearest to the centre of mass G and the desired orientation that is defined be the tangent to the path. The path following control is globally asymptotic stable as long as the largest eigenvalue of $\delta_k \mathbf{K}$ lies within the unit circle. We notice that the asymptotically equilibrium state has constant velocity as long as the path curvature is constant, see Spinello *et al.* [66]. The second contribution to the motion control comes from the gradient ascent update aimed at maximizing the singularity measure defined below

$$\mathbf{x}(k+1) = \mathbf{x}(k) + \delta_k \mathbf{H} \nabla_x det(J_x {J_x}^T)$$

where $\mathbf{H}$ is a positive definite gain matrix and ∇_x is the gradient with respect to $\mathbf{x}$, that in this case maps its scalar argument to a column vector. Since $\nabla_z det(J_x {J_x}^T) = 0$, the gradient ascent simplifies to

$$\mathbf{d}(k+1) = \mathbf{d}(k) + \delta_k \mathbf{H} \nabla_d det(J_x {J_x}^T)$$

and therefore the path following and the singularity avoidance are coupled with respect to the state $\mathbf{x}$.

6.4.1 Simulation Results

The discrete time simulation was performed in Matlab, where the robot was required to follow the dotted centre line of the pipeline as shown in Figures 6.5, 6.6 and 6.7. The forward motion is driven by a constant forward speed. The snapshots show how the robot successfully passes through the sharp 90° pipe while avoiding collisions and singularities. As mentioned earlier collision avoidance algorithm refrains all four corners of the module to come in contact with the inner wall of the pipe. Furthermore, a special case of collision avoidance of the arms with the walls of a pipe is added in the simulation which finds the point intersection between the arm and the wall. The intersection point on the wall is used to measure the new length of the arm and forces the desired change in the length of arm to avoid collision. Figures 6.2 and 6.6 show the configuration of a robot with and without the collision avoidance algorithm, respectively. The collision avoidance algorithm is an important step, since it assists the robot to successfully transit between the pipe segments.

Figure 6.8 shows how the lengths of arms d_1 and d_2 vary as the robot follows the centre line of the pipe. These parameters were set to have an upper bound of $0.6W_p$ to

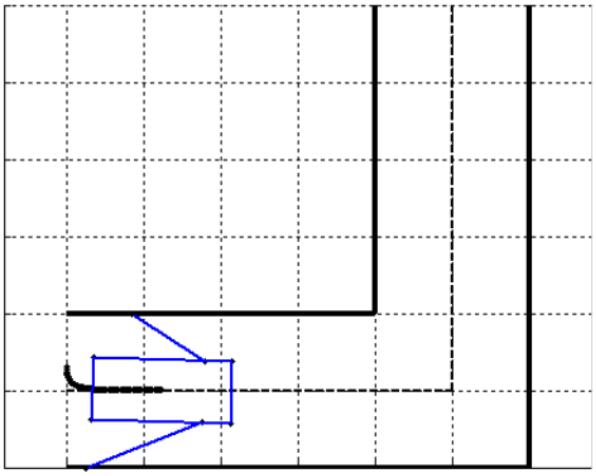

Figure 6.5: Robot navigation inside an elbow pipe (a) Horizontal segment (singularity-free)

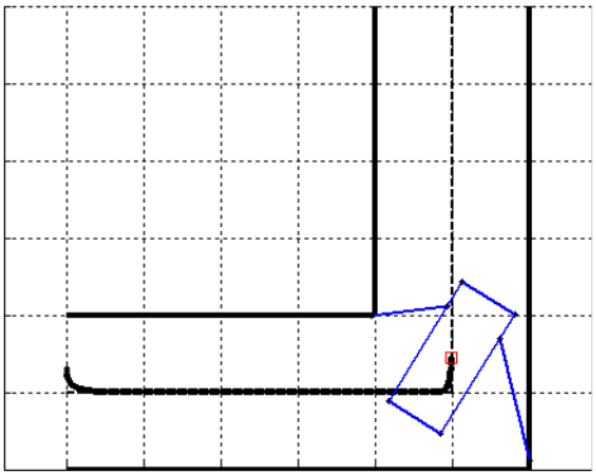

Figure 6.6: Robot navigation inside an elbow pipe (b) Crossing the elbow (avoid singularity and collision)

reflect the behaviour of a real prismatic joint. When the robot does not encounter any turn, the prismatic joint length tends to increase to the maximum value as it leads the robot as far as possible from singular configurations. This explains why d_2 was rapidly ramped up to its maximum value in the first few iterations of the simulation, as seen in Figure 6.8. Figure 6.9 shows the value of $det(J_x {J_x}^T)$ which is bounded between 0 and 1, while following the desired path. A sudden drop in the value of $det(J_x {J_x}^T)$ occurs when the robot tries to cross the elbow. The lowest value of this index corresponds to the

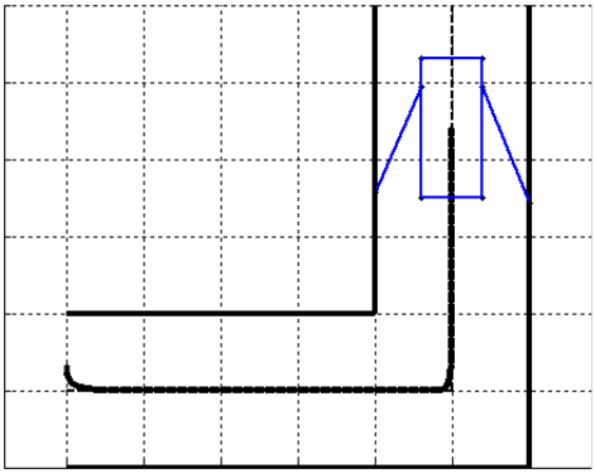

Figure 6.7: Robot navigation inside an elbow pipe (c) Vertical segment (singularity-free)

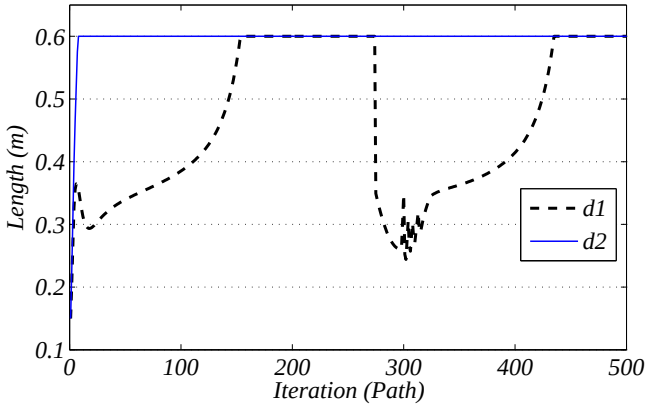

Figure 6.8: Prismatic arm length during the path-following of the robot

configuration shown in Figure 6.7. It is noted that at this configuration the two arms are close to being normal to the pipe wall causing the robot to be closer to a singular configuration. The fluctuation after the 300th iteration can be explained by Figures 6.8 and 6.9, and it is due to the length of the left arm d_1 being adjusted by the collision avoidance algorithm in order for the left wheel to remain in contact with the inner wall, and to not violate the kinematics constraints. Figure 6.10 shows the continuity of Γ_{sf} region, which confirms the success of the proposed solution to this critical sharp 90° elbow scenario.

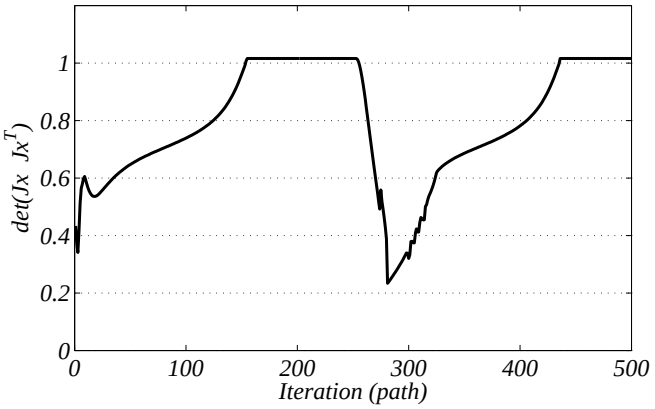

Figure 6.9: Proximity to singularity during the path-following of the robot

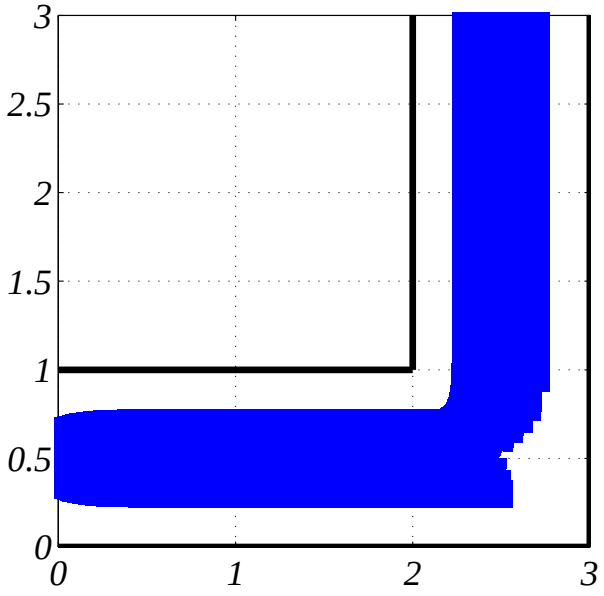

Figure 6.10: Γ_{sf}, singularity-free workspace in a sharp 90° elbow pipe-like structure

6.5 Chapter Summary

We considered a mobile robot for inspection of confined environments and investigated a critical manoeuvre that consists of passing through a sharp elbow with corners. The workspace analysis showed that the architecture with constant arms length leads to discontinuities due to the geometric impossibility of satisfying all constraints. Therefore, we proposed to added prismatic joints to augment the number of degrees of freedom and be able to satisfy the geometry and velocity constraints during the critical phases of the motion. We derived the position and velocity kinematics, through which we illustrated the autonomous operation of the robot by considering a path following control together with an optimal control that maximizes a measure of singularity based on the serial Jacobian. The algorithm was completed with a heuristic part for collision avoidance with the corners of the elbow. Simulation results show that the proposed solution leads to a continuous, singularity-free workspace allowing the robot to successfully pass through the elbow.

Chapter 7

Summary and Conclusions

The results presented in this thesis are steps toward the design of a robotic tool for autonomous non-destructive inspection of confined environments. This robotic tool is a flexible multi-body mechanism which can also be referred as a wheeled snake-like robot, since it mimics certain mobile properties of a snake. This type of robot exhibit excellent mobility in confined spaces and rough terrains. In this thesis, the kinematic analysis of a single module of a snake-like robot is presented. The single module has the architecture of a parallel mobile robot. The optimization of geometric parameters is performed to maximize the workspace and to avoid singularities while navigating across various pipe-like structures. Moreover, a modified version with with augmented degrees of freedom is presented together with an optimal control to avoid singularities when navigating across a singular geometric configuration.

A description of the mobile parallel robot as well as its positional and velocity kinematics is presented. For the purpose of navigation and inspection of pipelines, four different types of pipe-like structures are considered, one of which is a straight pipe with varied width; and the other three are 90°, 135° and 180° elbow joints. These pipe structures are used as a reference to analyze the workspace and singularities of the robot. The algorithm of determining a singularity-free workspace is explained in details and the Kinematic Conditioning Index is used as a metric for calculating the proximity to a singular configuration. Serial and parallel singularities of the mobile parallel robot are also investigated analytically, and all possible singular configurations are identified. It was observed that as the global orientation of the robot moves away from a symmetric configuration the width of the available workspace decreases. The results obtained from workspace and singularity analysis help understanding the influence of some key param-

eters in the behaviour of the system in various pipe-like structures. The singularity-free workspace obtained can assist the mobile parallel robot in its path-planning strategy.

The geometric parameters of the robot are optimized to enhance the performance, in terms of maximization of a reachable workspace and the avoidance of singular configurations. A discrete optimization problem is formulated with four constraints, such as singularity avoidance, collision avoidance, workspace continuity and contact constraints imposed between the wheels and the boundaries. Parametric variation is used to optimize the design parameters. The optimization problem is formulated by providing a range of possible values which the design parameters may attain in order to satisfy the kinematic constraints. The algorithm is initialized by discretely defining the reference workspace for a given global orientation angle. The design optimization performed without geometric constraints on parameters provides a solution which is not feasible, since it predicts the body of the robot to approach zero. Therefore, a constrained optimization is performed by setting the payload area as constant. The resulting optimal parameters provide a feasible design solution which maximizes singularity-free workspace of the robot. Due to the fact that several critical navigation scenarios for the mobile robot are the elbows, the selection of the design parameters can be biased toward the converged values obtained for 90°, 135° and 180° elbow. Figure 7.1 shows an example of various combinations of elbow pipe structures.

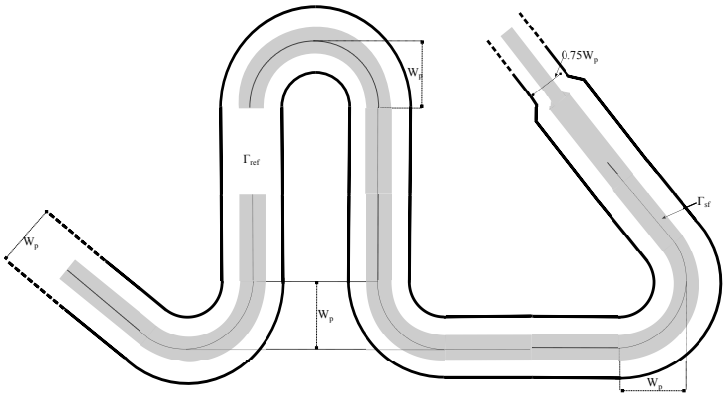

Figure 7.1: Combination of Pipe-like structures presented in these

A critical manoeuvrability scenario was investigated that consists of passing through a sharp 90° elbow. It was found through workspace analysis that the mobile parallel robot with constant arm length leads to discontinuity in its available workspace. Therefore, the number of degrees of freedom were augmented by adding prismatic arm joints. This allowed the robot to satisfy the geometric and kinematic constrains during the

critical phase of the motion. A path following control together with gradient ascent to maximize a measure of singularity based on serial Jacobian was used to illustrate the autonomous operation of the robot. The algorithm was completed with a heuristic part for collision avoidance with the corners of the elbow. Simulation results show that the proposed solution leads to a continuous, singularity-free workspace allowing the robot to successfully pass through the elbow.

The analysis and results presented in this thesis are published in Douadi *et al.* [13] and Spinello *et al.* [68]. It is hoped that the results and conclusion obtained in this thesis will help in the structural analysis and development of other types of mobile robots for confined environment applications.

Bibliography

[1] F. A. Adkins and E. J. Haug. Operational envelope of a spatial stewart platform. *Journal of Mechanical Design*, 119(2):330–332, 1997.

[2] D. Alciatore and C. Ng. Determining manipulator workspace boundaries using the monte carlo method and least squares segmentation. *ASME Robotics: Kinematics, Dynamics, and Controls*, 72:141–146, 1990.

[3] B. Bayle, J.Y. Fourquet, and M. Renaud. Manipulability analysis for mobile manipulators. *IEEE International Conference on Robotics and Automation*, 2:1251–1256 vol.2, 2001.

[4] B. Bayle, J.Y. Fourquet, and M. Renaud. Manipulability of wheeled mobile manipulators: application to motion generation. *International Journal of Robotics Research*, 22:565–581, 2003.

[5] D.P. Bertsekas. Incremental gradient, subgradient, and proximal methods for convex optimization: A survey.

[6] D.P. Bertsekas. *Convex Optimization Theory*. Athena Scientific optimization and computation series. Athena Scientific, 2009.

[7] I.A. Bonev and J. Ryu. A geometrical method for computing the constant-orientation workspace of 6-prrs parallel manipulators. *Mechanism and Machine Theory*, 36(1):1–13, 2001.

[8] R. Boudreau and C.M. Gosselin. The synthesis of planar parallel manipulators with a genetic algorithm. *Journal of Mechanical Design*, 121(3):533–537, Dec 1999.

[9] D. Chablat, P. Wenger, F. Majou, and J.P. Merlet. An interval analysis based study for the design and the comparison of 3dof parallel kinematic machines. *International Journal of Robotic Research*, 23:615–624, 2004.

[10] D. Chablat, P. Wenger, and J.P. Merlet. Workspace analysis of the orthoglide using interval analysis. *CoRR*, abs/0705.1284, 2007.

[11] F. Curtis and M. Overton. A sequential quadratic programming algorithm for nonconvex, nonsmooth constrained optimization. *SIAM Journal on Optimization*, 22(2):474–500, 2012.

[12] H. R. Daniali, P. J. Zsombor-Murray, and J. Angeles. Singularity analysis of planar parallel manipulators. *Mech. Mach. Theory*, 30(5):665–678, Jul 1995.

[13] L. Douadi, D. Spinello, W. Gueaieb, and H. Sarfraz. Planar kinematics analysis of a snake-like robot. *Robotica*, FirstView:1–17, 12 2013.

[14] R.B. Eckert. Internal corrosion health check advised for liquid and gas pipeline operators, March 2013.

[15] A. Evan. Cmu snakebots infest nuclear power plant. http://spectrum.ieee.org/automaton/robotics/industrial-robots/cmu-snakebots-infest-nuclear-power-plant/cmu-snakebots-infest-nuclear-power-plant, July 2013.

[16] A. Fattah and A. M. Hasan Ghasemi. Isotropic design of spatial parallel manipulators. *I. J. Robotic Res.*, 21(9):811–826, 2002.

[17] E.F. Fichter. A stewart platform based manipulator: General theory and practical construction. *The International Journal of Robotics Research*, 5(2):157–182, 1986.

[18] S.A. Fjerdingen, P. Liljeback, and A. Transeth. A snake-like robot for internal inspection of complex pipe structures (piko). *IEEE/RSJ International Conference on Intelligent Robots and Systems*, pages 5665–5671, 2009.

[19] A. Gallant, R. Boudreau, and M. Gallant. Geometric determination of the dexterous workspace of n-rrrr and n-rrpr manipulators. *Mechanism and Machine Theory*, 51(0):159 – 171, 2012.

[20] M. Gallant and R. Boudreau. The synthesis of planar parallel manipulators with prismatic joint for an optimal, singularity-free workspace. *Journal of Robotic Systems*, 19(1):13–24, Jan 2002.

[21] C. Gosselin and J. Angeles. Singularity analysis of closed-loop kinematic chains. *IEEE Transactions on Robotics and Automation*, 6(3):281–290, 1990.

[22] C. Gosselin and J. Wang. Singularity loci of a special class of spherical three-degree-of-freedom parallel mechanisms with revolute actuators. *The International Journal of Robotics Research*, 21(7):649–659, 2002.

[23] C.M. Gosselin and M. Guillot. The synthesis of manipulators with perscribed workspace. *Journal of Mechanical Design*, 113(4):451–455, Dec 1990.

[24] C.M. Gossellin and E. Lavoie. On the kinematic design of spherical three-degree-of-freedom parallel manipulators. *The International Journal of Robotics Research*, 12(4):185–197, Aug 1993.

[25] W. Guowu and D. Jian. Geometric and kinematic analysis of a seven-bar three-fixed-pivoted compound-joint mechanism. *Mech. Mach. Theory*, 45(2):170–184, Feb 2010.

[26] S.P. Han. A globally convergent method for nonlinear programming. *Journal of Optimization Theory and Applications*, 22(3):297–309, 1977.

[27] F. Hao and J.M. McCarthy. Conditions of line-based singularities in spatial platform manipulators. *Journal of Robotic Systems*, 15(1), 1998.

[28] F. Hao and J.P. Merlet. Multi-criteria optimal design of parallel manipulators based on interval analysis. *Mechanism and Machine Theory*, 40(2):157 – 171, 2005.

[29] L. He, Y. Chao, K. Suzuki, and K. Wu. Fast connected-component labeling. *Pattern Recognition*, 42:1977 – 1987, 2008.

[30] S. Hirose, H. Ohno, T. Mitsui, and K. Suyama. Design of in-pipe inspection vehicles for phi-25, phi-50, phi-150 pipes. *IEEE International Conference on Robotics and Automation*, 3:2309–2314 vol.3, 1999.

[31] S. Hirose and H. Yamada. Snake-like robots (tutorial). *Robotics Automation Magazine, IEEE*, 16(1):88–98, 2009.

[32] P. Hopkins. Oil and gas pipelines: Yesterday and today. *ASME*, 2006-7.

[33] J. R. Houser. *Numerical Methods for Nonlinear Engineering Models*. Springer, 2009.

[34] M. Huang. A study of workspace and singularity characteristics of 3-dof planar parallel robots. *ASME Conference Proceedings*, 2009(43833):209–215, 2009.

[35] M. Huang. Design of a planar parallel robot for optimal workspace and dexterity. *International Journal of Advanced Robotic Systems*, 2011.

[36] T. Huang, M. Li, X.M. Zhao, J.P. Mei, D.G. Chetwynd, and S.J. Hu. Conceptual design and dimensional synthesis for a 3-dof module of the trivariant robot. *IEEE Robotics*, 21(3):449–456, 2005.

[37] P. Huy and C. I-Ming. Optimal synthesis for workspace and manipulability of parallel flexure mechanism. *Proceeding of the 11th World Congress in Mechism and Machine Science*, 2003.

[38] A. Jamoussi. Robotics nde: A new solution for in-line pipe inspection. *Middle East Nondestructive Testing Confrence Exhibition*, 2005.

[39] B. John. Integrity management of pipelines subjected to stress corrosion cracking, March 2013.

[40] D. R. Jones, C.D. Perttunen, and B.E. Stuckman. Lipschitzian optimization without the lipschitz constant. *J. Optim. Theory Appl.*, 79(1):157–181, October 1993.

[41] M. Karol. Optimal design and modeling of spatial parallel manipulators. *The International Journal of Robotics Research*, 23(2):127–140, 2004.

[42] R. Kelaiaia, O. Company, and A. Zaatri. Multiobjective optimization of a linear delta parallel robot. *Mechanism and Machine Theory*, 50(0):159 – 178, 2012.

[43] M. Kircanski. Kinematic isotropy and optimal kinematic design of planar manipulators and a 3-dof spatial manipulator. *Int. J. Rob. Res.*, 15(1):61–77, February 1996.

[44] M. Kolesnik. Visual orientation and motion control of makro - adaptation to the sewer environment. *Int. Conf. on Simulation of Adaptive Behavior*, pages 62–69, 2002.

[45] O. Kun-Ku, L. Xin-Jun, K. Deuk Soo, and K. Jongwon. Optimal design of a micro parallel positioning platform. part one: Kinematic analysis. *Robotica*, 22:599–609, 10 2004.

[46] R. Kurtz and V. Hayward. Multiple-goal kinematic optimization of a parallel sherical mechanism with actuator redundancy. *IEEE Transactions of Robotics and Automation*, pages 644–651, 1992.

[47] Y.S. Kwon and B.J. Yi. Design and motion planning of a two-module collaborative indoor pipeline inspection robot. *IEEE Transactions on Robotics*, 28(3):681–696, 2012.

[48] D. Lee, T. Seo, and Kim J. Optimal design and workspace analysis of a mobile welding robot with a 3p3r serial manipulator. *Robotics and Autonomous Systems*, 59(10):813 – 826, 2011.

[49] S. Leguay-Durand and C. Reboulet. Optimal design of a redundant sherical parallel manipulator. *Robotica*, 15:399–405, 1997.

[50] M. Lopes and G. de Almeida. Manipulability optimization of a parallel structure robotic manipulator. *2nd Portogese Automatic Control Conferences*, 1996.

[51] A. Masayuki, T. Takayama, and S. Hirose. Development of "souryu-iii": connected crawler vehicle for inspection inside narrow and winding spaces. *Intelligent Robots and Systems, 2004. (IROS 2004). Proceedings. 2004 IEEE/RSJ International Conference on*, 1:52–57 vol.1, 2004.

[52] T. Mbarek, Lonij G., and Corves B. Singularity analysis of a fully parallel manipulator with 5dof based on grassmann line geometry. *12th IFRoMM World Congress*, pages 644–651, 2007.

[53] J.P. Merlet. *Parallel Robots*. Solid Mechanics and Its Applications. Kluwer Academic Publishers, 2000.

[54] B. Mircea and M. Constantinos. New performance indices and workspace analysis of reconfigurable hyper-redundant robotic arms. *International Journal of Robotic Research*, 23(6):643–659, 2004.

[55] M. Moghaddam and A. Hadi. Control and guidance of a pipe inspection crawler. *22nd International Symposium on Automation and Robotics in Construction*, pages 1–5, 2005.

[56] R. Murai, K. Ito, and K. Nakamichi. Proposal of a snake-like rescue robot designed for ease of use improvement of operability for non-professional operator. *34th Annual Conference of IEEE Industrial Electronics*, pages 1662–1667, 2008.

[57] M. Ono and S. Kato. A study of an earthworm type inspection robot movable in long pipes. *International Journal of Advances Robotic System*, 7:085–090, 2010.

[58] M.D. Powell. A fast algorithm for nonlinearly constrained optimization calculations. 630:144–157, 1978.

[59] J.J. Rastegar and D.D. Perel. Generation of manipulator workspace boundary geometry using the monte carlo method and interactive computer graphics. *J. Mech. Des.*, 112(3):452–454, 1990.

[60] J. Sefrioui and C. Gosselin. On the quadratic nature of the singularity curves of planar 3dof parallel manipulators. *Mech. Mach. Theory*, 30(4):533–551, May 1995.

[61] A. Shapiro, E. Rimon, and S. Shoval. A foothold selection algorithm for spider robot locomotion in planar tunnel environments. *The International Journal of Robotics Research*, 24(10):823–844, 2005.

[62] H. Shin, K.M. Jeong, and J.J. Kwon. Development of a snake robot moving in a small diameter pipe. *2010 International Conference on Control Automation and Systems*, pages 1826–1829, 2010.

[63] B. Siciliano. *Robotics: Modelling, Planning and Control*. Advanced Textbooks in Control and Signal Processing Series. Springer-Verlag London, 2009.

[64] N. Simaan and M. Shoham. Singularity analysis of a class of composite serial inparallel robots. *IEEE Transactions on Robotics and Automation*, 17(3):301–311, 2001.

[65] J. A. Snyman, L. J. Plessis, and J. Duffy. An optimization approach to the determination of the boundaries of manipulator workspaces. *Journal of Mechanical Design*, 122(4):447–456, 2000.

[66] D. Spinello, L. Douadi, and W. Gueaieb. Kinematic control of a mobile parallel robot in a confined environment. *Proceedings of the International Conference on Mechanical Engineering and Mechatronics (ICMEM)*, 2012.

[67] D. Spinello, W. Gueaieb, and R. Lee. Entropy filter for anomaly detection with eddy current remote field sensors. *2011 IEEE International Symposium on Robotic and Sensors Environments*, pages 95–100, 2011.

[68] D. Spinello, H. Sarfraz, W. Gueaieb, and L. Douadi. Critical maneuvers of an autonomous parallel robot in a confined environment. *Proceedings of the International Conference on Mechanical Engineering and Mechatronics (ICMEM)*, 2013.

[69] M.W. Spong and S. Hutchinson. *Robot Modeling and Control*. Wiley, 2005.

[70] M.W. Spong and M. Vidyasagar. *Robot dynamics and control*. Wiley, 2008.

[71] R. Stamper, L.W. Tsai, and G.C. Walsh. Optimization of a 3dof translational platform for well-conditioned workspace. *IEEE International Conference on Robotics and Automation*, pages 3250–3255, 1997.

[72] R.E. Stamper. *A three degree of freedom parallel manipulator with only translational degrees of freedom*. Phdthesis, University of Maryland, 1997.

[73] S. Stan, Balan R., and Maties V. Multi-objective design optimization of mini parallel robots using genetic algorithms. *IEEE International Symposium on Industrial Electronics, 2007*, pages 2173–2178, 2007.

[74] C. Stefanini, A. Menciassi, and P. Dario. Modeling and experiments on a legged microrobot locomoting in a tubular, compliant and slippery environment. *The International Journal of Robotics Research*, 25(5-6):551–560, 2006.

[75] B. H. Thacker, G.M. Light, J. F. Dante, E. Trillo, F. Song, C. F. Popelar, K. E. Coulter, and R. Page. Corrosion control in oil and gas pipelines, March 2010.

[76] A. Transeth. Anna konda the fire fighting snake robot. http://www.sintef.no/home/Information-and-Communication-Technology-ICT/Applied-Cybernetics/Projects/Our-snake-robots/Anna-Konda–The-fire-fighting-snake-robot/, Feb 2008.

[77] L.W. Tsai and S. Joshi. Kinematics and optimization of a spatial 3-upu parallel manipulator. *Journal of Mechanical Design*, 122:439–446, 2000.

[78] E.J. Van Henten, Vant Slot D.A., Hol C.W.J., and Van Willigenburg L.G. Optimal manipulator design for a cucumber harvesting robot. *Computers and Electronics in Agriculture*, 65(2):247 – 257, 2009.

[79] S. Wakimoto, J. Nakajima, M. Takata, T. Kanda, and K. Suzumori. A micro snake-like robot for small pipe inspection. *Proceedings of International Symposium on Micromechatronics and Human Science*, pages 303–308, 2003.

[80] A. Wolf, Ottaviano E., Shoham M., and Ceccarelli M. Application of line geometry and linear complex approximation to singularity analysis of the 3-dof capaman parallel manipulator. *Mechanism and Machine Theory*, 39(1):75 – 95, 2004.

[81] Y. Xinjie. Introduction to evolutionary algorithms. *40th International Conference on Computers and Industrial Engineering (CIE)*, pages 1–1, 2010.

[82] K.-H. Yoon and Y.-W. Park. Pipe inspection robot actuated by using compressed air. *IEEE/ASME International Conference on Advanced Intelligent Mechatronics*, pages 1345–1349, 2010.

[83] T. Yoshikawa. Manipulability of robotic mechanisms. *The International Journal of Robotics Research*, 4(2):3–9, 1985.

[84] T. Yoshikawa. Foundations of robotics: Analysis and controls. *Robotica*, 9:255–256, 3 1991.

[85] K. E. Zanganeh and J. Angeles. Kinematic isotropy and the optimum design of parallel manipulators. *Int. J. Rob. Res.*, 16(2):185–197, April 1997.

[86] S. Zarkandi, A. Vafadar, and M.R. Esmail. Prrrrrp redundant planar parallel manipulator: Kinematics, workspace and singularity analysis. *IEEE Conference on Robotics, Automation and Mechatronics (RAM)*, pages 61 –66, sept. 2011.

[87] Y. Zhao. Dimensional synthesis of a three translational degrees of freedom parallel robot while considering kinematic anisotropic property. *Robotics and Computer-Integrated Manufacturing*, 29(1):169 – 179, 2013.

[88] C. Zhu. In-pipe robot for inspection and sampling tasks. *Industrial Robot: An International Journal*, pages 39–45, 2007.

[89] E. Zitzler, Laumanns M., and Thiele L. Spea2: Improving the strength pareto evolutionary algorithm. Technical report, 2001.